

Quantized Theory for Emission and Coupling of Hybrid Systems

Vorgelegt von Diplom-Physiker
Thorsten Sverre Theuerholz
geb. in Leer

von der Fakultät II – Mathematik und Naturwissenschaften
der Technischen Universität Berlin

zur Erlangung des akademischen Grades

Doktor der Naturwissenschaften

— **Dr. rer. nat.** —

genehmigte Dissertation

Promotionsausschuss

- Vorsitzender : Prof. Dr. Thomas Möller, TU Berlin
1. Gutachter : Prof. Dr. Andreas Knorr, TU Berlin
2. Gutachter : Dr. Heiko Appel, FHI Berlin
3. Gutachter : Dr. Marten Richter, TU Berlin

Tag der wissenschaftlichen Aussprache: 10. Dezember 2015

Berlin, 2015

Abstract

Hybrid systems are generally capable of combining the advantages of both constituents to overcome the limitations of the single constituents. For an efficient development of new hybrid systems, a fundamental understanding of these systems is necessary. Therefore, we investigate in this thesis two types of hybrid systems: *First*, a hybrid system consisting of a metal sphere coupled to quantum dots is under investigation. By the combination of metal structures and quantum dots one can utilize the advantages of both constituents to their needs. For example, metal structures are capable of focusing light into the sub-wavelength regime, which is useful in the sense of miniaturization, and can provide strongly localized electric fields, called plasmons. These plasmons can interact with the excitons build up by external optical excitation in the quantum dots. *Second*, we introduce a theoretical description of the coupling between a semiconductor quantum well and a molecular layer. In such hybrid systems one can incoherently pump the quantum well and use the coupling to the molecular layer to transfer energy to the molecules. The combination of a medium which can be pumped electrically, the semiconductor quantum well, and a system which resonance energy can be modeled, the molecular layer, opens promising paths for high efficient light emitting systems.

We calculate the temporal evolution and spectra for the hybrid system consisting of a silver sphere and two quantum dots. Beside the coupling between the plasmons and excitons, we additionally include the coupling between the quantum dots, the so called Förster interaction. We investigate the influence of the Förster interaction on our observables of interest, the system polarization and the second order correlation function, in time and frequency domain. While the Rayleigh signal in time and spectra are barely influenced by the Förster interaction between the quantum dots, the second order correlation function is changed by up to three orders of magnitude. We found that the Förster interaction is capable of changing the emission statistics of the hybrid system from one regime to another. Although the Förster interaction is at least one order of magnitude smaller than the coupling between the plasmons and excitons, it is capable of tuning the emission statistic over a wide range. We are able to trace this back to redistributions of dipole-moments and resonances of the coupled hybrid system by the Förster interaction between the quantum dots. These energy shifts and asymmetric redistributions of dipole-moments give rise of asymmetric second order correlation functions with different kinds of emission statistics. We show that increasing the Förster interaction allows us to tune the emission statistic of the hybrid system from antibunched to coherent and further into the bunched regime while all other system parameters are kept constant. Furthermore, we model a whole ensemble of hybrid systems, one quantum dot coupled to a gold sphere, and compare our ensemble results with experiments primarily done in the group of H. Lange at Hamburg University. We found the same trends as observed in the experiments for the single constituents as well as for the coupled hybrid systems without adapting free parameters. Within a certain parameter range, the quantitative agreement is pretty striking, too.

For the molecular layer on top of a semiconductor quantum well, we develop a theory for the coupling beyond the dipole approximation. This is done by introducing transition charges to model the molecules as well as the semiconductor quantum well. These transition charges are provided by the Fritz Haber Institute Berlin using Density Functional Theory (DFT). With certain approximations, we derive an energy transfer from the semiconductor quantum well to the molecular layer and vice versa.

Zusammenfassung

Im Allgemeinen sind Hybrid-Systeme in der Lage die Vorteile ihrer Bestandteile zu kombinieren und so deren Anwendungsmöglichkeiten zu erweitern. Zur effizienten Entwicklung neuer Hybrid-Systeme ist deren fundamentales Verständnis nötig. In dieser Arbeit untersuchen wir zwei unterschiedliche Typen von Hybrid-Systemen: Das erste System bestehend aus einer Metallkugel gekoppelt an ein bzw. zwei Quantenpunkte. Durch die Kombination von Metallstrukturen und Quantenpunkten kann man die Vorteile beider Einzelsysteme zu seinen Gunsten nutzen. Metallstrukturen können zum Beispiel Licht in Bereiche fokussieren die kleiner als die Wellenlänge des verwendeten Lichtes sind, dies kann genutzt werden um optische Geräte kompakter zu bauen. Außerdem kann es in Metallen stark lokalisierte elektrische Felder geben, so genannte Plasmonen. Diese Plasmonen können mit den Exzitonen, optischen Anregungen im Quantenpunkt, wechselwirken. Als zweites Hybrid-System betrachten wir eine Molekülschicht auf einem Quanten-Well und leiten die Rate für den Energietransfer zwischen beiden her. Die Vorteile der einzelnen Systeme sind zum einen die Möglichkeit einen Quanten-Well elektrisch zu pumpen und zum anderen die Modelierbarkeit der optischen Übergangsfrequenz der Moleküle, was solche Hybrid-Systeme zu hoch effizienten Lichtquellen machen könnte.

Für eine Silberkugel gekoppelt an zwei Quantenpunkte berechnen wir die zeitliche Entwicklung sowie Spektren für die interessanten Systemobservablen von Interesse. Neben der Kopplung zwischen den Exzitonen und Plasmonen berücksichtigen wir zusätzlich die Kopplung zwischen den Quantenpunkten, die sogenannte Förster-Wechselwirkung. Den Einfluss dieser auf die Polarisation und auf die Emissionsstatistik des Hybrid-Systems untersuchen wir im Zeit- und Frequenzraum. Das Rayleigh-Spektrum wird kaum durch die Förster-Wechselwirkung beeinflusst. Die Emissionsstatistik hingegen verändert sich um drei Größenordnungen. Die Förster-Wechselwirkung ändert die Statistik auch qualitativ, z. B. von einer anti-gebunchten zu einer kohärenten bis hin zu einer gebunchten. Dies geschieht obwohl die Förster-Wechselwirkung zwischen den Quantenpunkten mindestens eine Größenordnung kleiner als die zwischen Plasmonen und Exzitonen ist. Grund für den dennoch starken Einfluss ist die Umverteilung von Dipolmomenten und die Verschiebung von Übergangsenergien in dem gekoppelten Hybrid-System. Diese führen zu asymmetrischen Spektren der Emissionsstatistik mit unterschiedlichen Statistiken. Wir zeigen, dass man durch Erhöhen der Förster-Wechselwirkung zwischen den Quantenpunkten die Emissionsstatistik von einer anti-gebunchten über eine kohärente bis zu einer gebunchten Statistik verändern kann, wobei alle anderen Systemparameter konstant gelassen werden. Zusätzlich modellieren wir ein ganzes Ensemble von Hybrid-Systemen, bestehend aus jeweils einer Goldkugel und einem Quantenpunkt, und vergleichen unsere Theorie mit Messungen, welche hauptsächlich in der Gruppe von H. Lange an der Universität Hamburg durchgeführt wurden. Theorie und Experiment zeigen die selben Trends für die einzelnen Systeme und die gekoppelten Hybrid-Systeme. Innerhalb eines bestimmten Parameterbereiches gibt es zudem eine überzeugende quantitative Übereinstimmung.

Für die Kopplung zwischen einer Molekülschicht und einem Quantum-Well entwickeln wir eine Theorie jenseits der Dipolnäherung. Dies wird möglich durch die Einführung von sogenannten *transition charges* die das elektrische Feld des Moleküls und das des Quantum-Wells im Außenraum beschreiben. Diese *transition charges* werden im Fritz Haber Institut Berlin mittels Dichte Funktional Theorie (DFT) berechnet. Mit einigen Näherungen berechnen wir die Energietransferrate vom Quanten-Well zur Molekülschicht und umgekehrt.

Contents

I Prologue	11
1 Introduction	13
1.1 Structure of the thesis	14
II Theory	15
2 Properties of metal spheres	17
2.1 Resonance energy and damping of MNPs calculated from diffraction index . . .	17
2.1.1 Resonance energies and damping rates of metal spheres within the quasi static approach	19
2.1.2 Calculation of resonance energies and damping rates of metal spheres by using the Helmholtz equation	20
3 Quantum mechanical theory	27
3.1 Source field expression	27
3.2 Fano effect	29
3.2.1 Classical Fano effect	30
3.2.2 Quantum mechanical Fano effect	31
III Quantum dots coupled to a metal sphere	35
4 Two quantum dots coupled to a metal nanoparticle	37
4.1 Introduction	38
4.2 Hamilton operators	39
4.3 Observables of interest and equation of motion of the hybrid system	42
4.4 Temporal evolution of the coupled hybrid system for different excitations	46
4.4.1 Temporal evolution of the system polarization after excitation with an Gaussian pulse	47
4.4.2 Second order correlation function of the hybrid system for optical con- tinuous wave excitation	48
4.5 Optical emission spectra of the hybrid system	51
4.5.1 Rayleigh spectra of the uncoupled constituents of the hybrid system	52
4.5.2 Rayleigh spectra of the resonantly coupled hybrid system	53
4.5.3 Rayleigh spectra of the off-resonantly coupled hybrid system	56

4.6	Rayleigh spectra for different pump intensities of the external optical field	58
4.7	Second order correlation function of the hybrid system in frequency domain	59
5	Ensemble of coupled quantum dot and gold sphere hybrid systems	71
5.1	Introduction to the hybrid system and experimental setup	71
5.2	Characterization of the uncoupled hybrid system constituents and introducing observables of interest	76
5.3	Coupling between the constituents of the hybrid: Comparison between the dipole-dipole interaction and a full classical calculation	78
5.4	Temporal evolution of single hybrid systems	80
5.5	Temporal evolution of an ensemble of coupled hybrid systems	83
IV	Hybrid inorganic organic systems	91
6	Molecules coupled to a semiconductor quantum well	93
6.1	Coupling elements of hybrid inorganic/organic systems	93
6.2	Band structure of the semiconductor	95
6.3	Hamilton Operator of the HIOS	96
6.4	Equation of motion for the HIOS	98
6.5	Transfer rates	99
V	Epilogue	103
7	Conclusion and Outlook	105
	Danksagung	107
	Appendices	109
A	Parameter for fit of the dielectric function	111
B	Equations of motion for the hybrid system	113
B.1	One quantum dot coupled to a metal sphere	113
B.2	Two quantum dot coupled to a metal sphere	113
C	Parameters used to model the optical experiments	117
D	Different contributions to the far field signal for the red quantum dots coupled to a gold sphere	119

List of Figures

2.1	Comparison of the Drude fit and a more advanced fit to the measurements of Johnson and Christy for gold (Au) [JC72]. On the left, the real part of the dielectric function is plotted and on the right side for the imaginary part.	18
2.2	Comparison of the resonance energy ω_{sp} of the dipole mode versus the radius R of the sphere (left) and the damping rate γ_{sp} versus the radius (right) for different dielectric functions to model the bulk material (Au). The sphere is embedded in a dielectric medium with $\epsilon_{out} = 1.77$, valid, e.g., for water.	23
2.3	Comparison of the resonance energy ω_{sp} of the dipole mode versus the radius R of the sphere (left) and the damping rate γ_{sp} versus the radius (right) for different dielectric functions to model the bulk material (Au). The sphere is embedded in a dielectric medium with $\epsilon_{out} = 3$	24
2.4	Comparison of the resonance energy ω_{sp} of the dipole mode versus the radius R of the sphere (left) and the damping rate γ_{sp} versus the radius (right) for different dielectric functions to model the bulk material (Au). The sphere is embedded in a dielectric medium with $\epsilon_{out} = 5$	24
3.1	Left: Sketch of the mechanical system. Right: Spectrum of the pendulum amplitudes $ x_1 $ and $ x_2 $ versus the frequency of the driving force acting on the first pendulum.	30
3.2	Left: Energy scheme of the hybrid system consisting of a metal sphere and a quantum dot. Both are coupled via g . Right: Spectra of the steady state for different excitations energies. Plotted are the absolute values of the plasmonic $ a^\dagger $ and the excitonic $ \rho_{vc} $ polarization. The metal sphere diameter is 10nm as well as the distance between the constituents. The metal sphere resonance is at $\Delta\omega = 0\text{meV}$ and the quantum dot one at $\Delta\omega = 20\text{meV}$. Note, the excitonic polarization is multiplied by 20.	32
4.1	Sketch of the system including the coupling between the quantum dots V_{12} , between the quantum dots and silver sphere $g_{1/2}$ and the external electrical field $E(t)$. θ denotes the angle between the system axis and the external electrical field.	38
4.2	Sketch of the equations of motion for two quantum dots coupled to a metal sphere and to each other by the Förster interaction. The quantum dots has one electron each. Red arrows accounts for definitions and the black ones for coupling of the dynamical quantities. Note, the hierarchy in the excitonic quantities is closed for the case of two quantum dots at this stage.	46

4.3	Temporal evolution of the Rayleigh scattering of the hybrid system. The excitonic resonance of both quantum dots and the plasmon resonance are equal. The system is excited on resonance by a Gaussian pump pulse. Note, the y-axis is on a logarithmic scale.	47
4.4	Sketch of the energy levels of a V -type three level system (left) and for a Λ -type one (right).	48
4.5	Possible emission statistics.	49
4.6	Second order correlation function for resonantly coupled hybrid systems on logarithmic scale. The hybrid system is driven by weak continuous wave excitation. The diameter of the silver sphere is 10nm and we plot two different distances between the constituents ($R = 10\text{nm}$ and $R = 16\text{nm}$) with and without Förster interaction between the quantum dots.	50
4.7	Second order correlation function for resonantly coupled hybrid systems on logarithmic scale excited slightly off-resonant. The hybrid system is driven by weak continuous wave excitation. The diameter of the silver sphere is 10nm and we plot two different distances between the constituents ($R = 10\text{nm}$ and $R = 16\text{nm}$) with and without Förster interaction between the quantum dots.	50
4.8	τ -dynamics of the second order correlation function. The hybrid system is excited resonantly by the external optical field.	51
4.9	Rayleigh picture of the uncoupled constituents of the hybrid system versus the detuning to the external optical field. Left: Two quantum dots with identical parameter but different excitonic transition energies. The detuning is 2 meV. Shown are the spectra with ($V_{12} = 0.45\text{meV}$) and without ($V_{12} = 0\text{meV}$) the Förster interaction between the two quantum dots. Right: Bare metal sphere with its broad resonance and two identical quantum dots with and without the Förster interaction between them.	52
4.10	Rayleigh spectra for two quantum dots resonantly coupled to the silver sphere versus the detuning to the external optical pump field. Left: Spectra for a silver sphere of $r_m = 5\text{nm}$ radius and several distances between the quantum dots and the silver sphere. Right: Rayleigh spectra for a 5nm silver sphere and a distance of 10nm between the quantum dots and the silver sphere with and without the Förster interaction between the quantum dots.	54
4.11	Rayleigh spectra for two quantum dots coupled to the silver sphere versus the detuning of the surface plasmon frequency to the external optical pump field ($\Delta\omega_{ext} = \omega_{ext} - \omega_{pl}$). Left: Spectra for a silver sphere of $r_m = 5\text{ nm}$ radius and several distances between the quantum dots and the silver sphere. Right: Rayleigh spectra for a 5 nm silver sphere and a distance of 10 nm between the quantum dots and the silver sphere with and without the Förster interaction between the quantum dots.	57
4.12	Rayleigh spectra of a resonantly (left) and off-resonantly coupled hybrid system for different pump intensities of the external optical field. Shown is the Rayleigh spectra for a distance of 15nm ($g = 11.5\text{meV}$) between the two quantum dots and the silver sphere ($r_m = 5\text{nm}$). There is no Förster interaction between the quantum dots.	59

4.13	Second order correlation function ($g^{(2)}(\omega_{ext})$) versus detuning of the plasmon frequency to the external pump field ($\Delta\omega_{ext} = \omega_{ext} - \omega_{sp}$). The results are for different distances R and strengths of the Förster interaction between the quantum dots V_{12} . The distance 10 nm between the quantum dots and the silver sphere corresponds to a coupling strength $g = 38.8$ meV, 16 nm corresponds to $g = 9.5$ meV.	60
4.14	Plasmon density correlation ($\langle a^\dagger a^\dagger a a \rangle$) and the square of the plasmon density ($\langle a^\dagger a \rangle^2$) versus the detuning to the external optical field. The parameters for the single plots correspond to the one chosen for the second order correlation function in Figure 4.13	62
4.15	First lowest order of the coupled hybrid system with and without Förster interaction between the quantum dots. Besides the Förster interaction the distance R between the quantum dots and the silver sphere is varied. The orders 1 up to 4 are plotted on a logarithmic scale.	63
4.16	Total transition dipole moment (Equation 4.42) for different Förster interaction strength between the two quantum dots versus the coupling strength between excitonic and plasmonic system.	65
4.17	Sketch of the system states. Top: System states for the case without interaction between the excitons and plasmons. Bottom: System states (polaritons) for the case with coupling between the constituents of the hybrid. In both cases excitonic and plasmonic transition are in resonance ($E_{q_i} = E_{sp}$). The picture is taken from [TCRK13].	66
4.18	Hybrid system restricted to transitions from one manifold to the next higher one. The distance between the quantum dots and the silver sphere is $R = 15$ nm, corresponding to an interaction strength of $g = 11.5$ meV. We show the spectra for the plasmon density $\langle a^\dagger a \rangle$ and the excitonic polarization ρ_{vc} without the Förster interaction ($V_{12} = 0$ meV) between the quantum dots (upper two rows) and with the Förster interaction ($V_{12} = 0.45$ meV) between the quantum dots (two lower rows). Furthermore, we varied the damping of the plasmons to make the newly formed resonances visible in the coupled hybrid system. The spectra are normed.	68
4.19	Second order correlation function versus the Förster interaction between the quantum dots. The hybrid system is excited resonantly by the external optical field.	69
4.20	Second order correlation function versus the Förster interaction between the quantum dots. The hybrid system is excited off-resonantly ($\Delta = 0.9$ meV) by the external optical field.	69
5.1	Sketch of the gold sphere and the quantum dot surrounded by polymer shell securing the right distance between the gold sphere and the quantum dot. The lipoic acid group, linking gold sphere and the polymer shell, is magnified. (Picture taken from (in submission))	72

5.2	Sketch of the theoretical framework employed to model the experiments. The system is excited with a chirped pump pulse. The excitons in the quantum dots interacts via Coulomb coupling with the plasmons on the metal sphere. Both sub-systems, the excitonic one as well as the plasmonic one are damped. The damping for the plasmons is mostly due to ohmic losses and the excitonic one to pure dephasing, nevertheless we also include radiative dephasing for incoherent quantities to describe the fluorescence lifetime properly. Including all these parameters, we calculate the far field signal/fluorescence signal.	73
5.3	TEM pictures of single systems. The diameter of the gold sphere is 20 nm and the spacer thickness 5 nm (left and middle). The image on the right shows cross-linking of the gold spheres for a high ratio of gold spheres to quantum dots. (Pictures taken from (in submission)).	74
5.4	Mono-exponential fit to determine the radiative dephasing of the quantum dots. Left: Measurement of the green quantum dots and fit to the data. Right: Comparison between experiment and fit to the data for the red quantum dots.	75
5.5	Linear spectra of the uncoupled single constituents of the hybrid system (quantum dots and metal spheres with different diameter D_{Au}). Note, the resonance energy of the quantum dots was determined by spectral measurements, all other parameters are obtained theoretically or by independent measurements.	76
5.6	Measured spectra of the uncoupled constituents of the hybrid system. The spectra of the green and red quantum dots are fluorescence spectra. The gold spheres are measured in absorption.	77
5.7	Spectra of the red quantum dots only (red curve) and the red quantum dots coupled to gold spheres with different diameters. For the coupled systems the spectra are recorded with the used spectral filter to block the laser pulse and the light scattered by the gold.	78
5.8	Coupling strength between the excitons and plasmons (solid lines, left scale) versus the diameter of the metal sphere according to Equation 4.5 and the results for the losses of an excited electric dipole nearby a metal sphere (dots, right scale) versus the diameter of the metal sphere. The classical calculation of the losses was done by Ziliang Ye from the group of Tony Heinz.	79
5.9	Temporal evolution of single hybrid systems consisting of a red quantum dot and a gold sphere with a diameter of 12 nm. The distance between both constituents is ensured by a 15 nm spacer. a) uncoupled hybrid system with a very fast plasmonic decay, within pulse duration, and a very slow excitonic decay due to small radiative dephasing. b-d) coupled single hybrid systems for weak and strong coupling between the constituents. Due to the coupling the plasmonic and excitonic parts show the same decay.	80
5.10	Excitonic and plasmonic part of the far field signal versus time for the hybrid system with green quantum dots and gold sphere with 12nm diameter. a) uncoupled constituents, the plasmonic part follows the pulse. b-c) coupled hybrid system for different coupling strengths used to calculate the ensemble average.	82

5.11	Far field signal for 50 hybrid systems to compute the ensemble average (solid lines). The coupling strength between the constituents of the single hybrid systems is given by the color code on the right. For comparison we additionally plot the curve for uncoupled red quantum dots (red dashed). The averaged curve of the hybrid system ensemble (black dashed) and the averaged curve convolved with the instrumental response function (purple dashed) are shown, too. The systems are excited by a 300fs chirped Gaussian pulse.	84
5.12	Theoretical curves averaged over an ensemble of 50 single hybrid systems and convolved with the instrumental response function. Shown in a-d are the different parts of the far field signal (5.6) for a spacer thickness of 15nm and for several diameters of the gold spheres. In c) the complete signal of the hybrid system is shown.	85
5.13	Comparison between the theoretical calculations (left column) and the experimental results (right column). Each plot shows the temporal evolution of the far field signal for a certain gold sphere diameter and different spacer thicknesses. The plots are on a logarithmic scale and normed.	87
5.14	Comparison between the theoretical calculations (left column) and the experimental results (right column). Each plot shows the temporal evolution of the far field signal for a certain spacer thickness and different gold sphere diameters. The plots are on a logarithmic scale and normed.	88
5.15	Temporal evolution of the far field signal for hybrid systems consisting of green quantum dots coupled to gold spheres. Left: The ensemble average is shown for different gold sphere diameters. Right: Far field signal convolved with the instrumental response function.	89
6.1	Sketch of the band structure of the substrate using the effective mass approximation.	96
D.1	Theoretical curves averaged over an ensemble of 50 single hybrid systems and convolved with the instrumental response function. Shown in a-c are the different parts of the far field signal (5.6) for a spacer thickness of 5nm and for several diameters of the gold spheres. In c) the complete signal of the hybrid system is shown.	120
D.2	Theoretical curves averaged over an ensemble of 50 single hybrid systems and convolved with the instrumental response function. Shown in a-c are the different parts of the far field signal (5.6) for a spacer thickness of 10nm and for several diameters of the gold spheres. In c) the complete signal of the hybrid system is shown.	121

List of Tables

2.1 Results for the resonances of the dipole mode and damping rates of gold and silver metal spheres for different dielectric backgrounds.	20
A.1 Fit parameter for gold.	111
A.2 Fit parameter for silver.	111
C.1 Parameters used to model the optical measurements in Chapter 5 and how they are determined.	117

Part I
Prologue

Chapter 1

Introduction

The phrase *hybrid system* describes generally the combination of two or more systems with different properties. In this thesis we focus on two different types of hybrid systems: The first type is composed of a metal sphere coupled to one or two semiconductor quantum dots. The second type consists of a molecular layer on top of a semiconductor quantum well. Both of these hybrid systems are intensively studied experimentally as well as theoretically to gain new insights in the occurring physical processes. This could allow for an efficient development of new devices. The use of metal structures was found to be very powerful for different kinds of sensing due to their ability to strongly enhance electric fields into the sub-wavelength regime [LD13, GG09, NHL⁺08]. These strong fields can be localized propagate and are called plasmons [BP51, PB52, BP53, Pin53]. The combination of metal structures with, e.g., quantum dots or other two level systems give rise of a variety of physical effects. Devices suitable for processing quantum information [FLKA14, TMO⁺13, CSHL06] or the equivalent to the laser, the so called Spaser (surface plasmon amplification by stimulated emission of radiation) [BS03, NZB⁺09, RGTK15] are intensively studied and only two examples. We focus on metal spheres coupled to two level system, in our case semiconductor quantum dots. It was previously found that the interaction between the excitons and the plasmons alter the emission statics of the hybrid [RDSF⁺10]. We demonstrate a hybrid system with one metal sphere coupled to two quantum dots in which the emission can be tuned over a wide range by only changing the interaction strength between the semiconductor quantum dots [TCRK13]. Furthermore, we compare our theoretical results with experimental ones and find convincing qualitative agreement (in submission).

The second type of hybrid system investigated in this thesis consists of a molecular layer on top of a semiconductor quantum well. These systems are promising candidates for highly efficient light sources. The aim is to, e.g., pump the quantum well electrically and to transfer this energy to the molecules which then emit light [VKR⁺14, FKS⁺15, BSX⁺06, SBB⁺15]. Since the distance between the molecular layer and the semiconductor quantum well might be small, we introduce a theory beyond the dipole approximation by using transition charges [MAR06, CMW09, CSSJ10]. The transition charges are provided by the Fritz Haber Institute derived using density functional theory (DFT).

1.1 Structure of the thesis

This thesis is divided in five parts:

The first part is the Prologue with an introduction and informations about the structure of the thesis.

The second one is a theory part where some of the used theories are introduced. This part is divided in a classical and a quantum mechanical theory part.

In the third part a model is introduced to describe a hybrid system consisting of a metal sphere and one/two semiconductor quantum dots. For the hybrid system consisting of one metal sphere coupled to two quantum dots, we investigate the temporal evolution and the spectra of the observables of interest. Furthermore, we describe the temporal evolution after pulse excitation of an ensemble of coupled hybrid systems in the third part. Our theoretical results for the ensemble of coupled hybrid systems are compared to measurements. In the end we discuss and compare the theoretical and experimental results.

In the forth part the coupling between a molecular layer on top of a quantum well is investigated. We derive an energy transfer rate between the molecular layer and the quantum well beyond the dipole approximation. We achieve this by using transition charges to model the electric field of the molecules and the quantum well in their outer region.

The fifth and last part consists of the *Danksagung* and the Appendices.

Part II
Theory

Chapter 2

Properties of metal spheres

In this chapter, we give an overview over the theoretical concepts used to determine the properties of the metal spheres, which are constituent of the hybrid systems under investigation. First, two fits for the dielectric function of metals are introduced and discussed. Namely, the Drude model and a more complex multi Lorentzian fit. Using this analytical expression for the dielectric function of the metal, a comparison of two different approaches to calculate the resonance energy of the dipole transition and the corresponding damping rate of a metal sphere is given. It turns out, that the Drude fit is pretty good for surroundings of the metal sphere with a high permittivity (above 4), which leads to lower dipole transition energies. Comparing the Drude model, the multi Lorentzian fit and the values measured by Johnson & Christy [JC72], we found that the Drude model is good for energies below 2eV. We use this properties of the metal spheres to include them into our quantized theory for hybrid systems. In Chapter 4, we couple two quantum dots to a silver sphere and investigate the emission statistics of this hybrid system. Later, in Chapter 5, we model an ensemble of hybrid systems and compare our results to experiments carried out in the group of Holger Lange (Universität Hamburg). In this case, gold spheres and two different kinds of quantum dots build a hybrid system and are investigated by, e.g., time resolved photoluminescence measurements.

2.1 Resonance energy and damping of MNPs calculated from diffraction index

There are two approaches widely used to calculate the resonance energy of spherical MNPs and the corresponding damping rates using only measured data of the refractive index of the metal involved.

The first one starts with the Laplace equation in the quasi-static approach and derives by using continuity relations the resonance energy and damping of the surface plasmon modes [RDSF⁺10, BS03]. Within the used approximations, this approach is able to calculate the resonance energy and damping rate of the surface plasmon dipole mode. Nevertheless, this quite simple method is not able to include the size dependency of the metal sphere.

The second one starts with the Helmholtz equation, obtained from Maxwell equations in the time harmonic approximation, and formulates continuity conditions at the surface of the sphere. This approach is more complex than the first one, but in contrast, it is able to include the size of the metal sphere. This will be especially important when we compare our theory

with experiments, which clearly show the dependency of the resonance energies on the size of the metal sphere.

Before taking a closer look at two possible calculations for the properties of the metal sphere, we give a few remarks concerning the dielectric function of metals. Usually the dielectric function $\varepsilon(\omega)$ of a metal is approximated by a Drude (Drude-Sommerfeld) approximation

$$\varepsilon(\omega) = \varepsilon_0 - \frac{\omega_{p,bulk}^2}{\omega^2 + i\gamma_{p,bulk}\omega}, \quad (2.1)$$

which is in great agreement with the measurements [JC72] for small energies, cp. Figure 2.1. $\omega_{p,bulk}$ is the bulk plasma frequency and $\gamma_{p,bulk}$ the corresponding damping term. A more precise approximation of the dielectric function can be achieved by fitting the function introduced by Etchegoin et. al. [ELRM06] to the measured data of Johnson and Christy. The main idea is to fit the dielectric function with more than one pole, as it is the case in the Drude limit. The fit function reads [ELRM06]:

$$\varepsilon_{Au} = \varepsilon_\infty - \frac{1}{\lambda_p^2 \left(\frac{1}{\lambda^2} + \frac{i}{\gamma_{p,bulk}\lambda} \right)} + \sum_{i=1,2} \frac{A_i}{\lambda_i} \left[\frac{e^{i\phi_i}}{\frac{1}{\lambda_i} - \frac{1}{\lambda} - \frac{i}{\gamma_i}} + \frac{e^{-i\phi_i}}{\frac{1}{\lambda_i} + \frac{1}{\lambda} + \frac{i}{\gamma_i}} \right]. \quad (2.2)$$

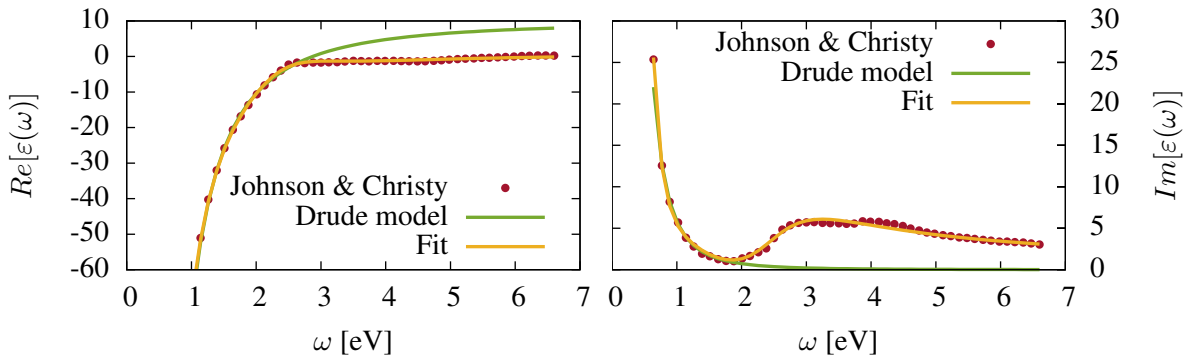


Figure 2.1 | Comparison of the Drude fit and a more advanced fit to the measurements of Johnson and Christy for gold (Au) [JC72]. On the left, the real part of the dielectric function is plotted and on the right side for the imaginary part.

The determined fit parameters are given in the Appendix A. In Figure 2.1 it becomes obviously, that the fit with multiple poles has a way more striking agreement with the dielectric function of gold than the Drude model, especially for higher energies.

In the following, the different results for the resonance energies and the damping rates of the plasmon modes (usual the dipole mode $l = 1$) will be discussed. It is possible to include an additional damping term to the fit of the dielectric function of the bulk metal. This additional term account for surface scattering and becomes important for decreasing size of the sphere ($R < 10\text{nm}$). Usually, the surface scattering is introduced by replacing the ordinary damping rate of the bulk material $\gamma_{p,bulk}$ by

$$\gamma(R) = \gamma_{p,bulk} + A \frac{v_F}{R} \quad (2.3)$$

with the Fermi velocity v_F and a phenomenological factor A . This factor needs to be fit to the experiment and is between 1 and 10. This surface scattering is due to the limitation of the mean free path of the electrons in small spheres [KF69] and results in scattering of the electrons with the surface. Sometimes this type of surface scattering is named Kreibig damping after Uwe Kreibig, who introduced and measured the phenomenological parameter A [KG85].

It is straight forward to include the surface scattering into the Drude approximation. However, it is not clear how to include the surface scattering into the more elaborated multi Lorentzian approach (2.2), since several damping rates are involved. One would need to find an accurate A for every damping rate included. Furthermore, A is usually fit to experimental data under the assumptions that a Drude model is used [NGPJ⁺06]. This can lead to unphysical behavior for the damping rates if surface scattering is include for the multi Lorentzian fit. For instance, it leads to a smaller damping in the case of very small spheres instead of a larger on. Therefore, surface scattering is only discussed for the Drude model, but always neglected for the multi Lorentzian approach. A more detailed discussion is given in Section 2.1.2.

With the analytical expression of the dielectric function, it is possible to calculate the required resonance energies and damping rates for the plasmon modes in dependency of the surrounding material and later also in dependency of the radius of the metal sphere.

2.1.1 Resonance energies and damping rates of metal spheres within the quasi static approach

A metal sphere in an constant electric field (E_z), which has only an non-vanishing z component, can be described by the Laplace equation $\Delta\Phi = 0$. The excitation field can be approximated as constant over the sphere, as long as the exciting wavelength is at least one order of magnitude larger than the diameter of the sphere. If this holds, one can assume a constant electric field over the whole volume of the sphere. The solution for the electric field $E(\mathbf{r})$ is [Jac99]:

$$\mathbf{E}(\mathbf{r}, \omega) = E_{z,ext} \frac{\varepsilon_{out} - \varepsilon(\omega)}{2\varepsilon_{out} + \varepsilon(\omega)} \mathbf{G}(\mathbf{r}), \quad (2.4)$$

with the Green's function

$$\mathbf{G}(\mathbf{r}) = \begin{cases} \hat{\mathbf{e}}_z & r < R \\ \frac{R^3}{r^3} [3(\hat{\mathbf{e}}_z \cdot \hat{\mathbf{e}}_r) \hat{\mathbf{e}}_r - \hat{\mathbf{e}}_z] & r > R \end{cases} \quad (2.5)$$

for the inside of the sphere ($r < R$) and the outside ($r > R$). $\hat{\mathbf{e}}_r$ and $\hat{\mathbf{e}}_z$ are basis vectors in cylindrical coordinates. The polarizability β of the metal sphere

$$\beta = \frac{\varepsilon_{out} - \varepsilon(\omega)}{2\varepsilon_{out} + \varepsilon(\omega)} \quad (2.6)$$

shows the strongest enhancement for vanishing denominator $2\varepsilon_{out} + \varepsilon(\omega) = 0$, this is the so called Fröhlich condition [FZS14]. That yields the well known condition $-2\varepsilon_{out} = \varepsilon(\omega_{sp})$ for the surface plasmon resonance ω_{sp} (valid as long as the damping γ_{sp} of the surface plasmons is way smaller than their resonance energies ω_{sp}).

To obtain the damping rate, a first order Taylor expansion of $\varepsilon(\omega) = \text{Re}[\varepsilon(\omega)] + \text{Im}[\varepsilon(\omega)]$ is performed and the result is insert in the polarizability β . This yields

$$\beta = \frac{\varepsilon_{out} - \varepsilon(\omega)}{2\varepsilon_{out} + \varepsilon(\omega)} \approx \frac{3\text{Im}\varepsilon_{out}\eta}{\text{Im}(\omega_{sp} - \omega) + \frac{\gamma_{sp}}{2}}, \quad (2.7)$$

which results in a damping $\gamma_{sp} = 2\eta\Im[\varepsilon(\omega)]$ with $\eta^{-1} = \left. \frac{d\text{Re}[\varepsilon(\omega)]}{d\omega} \right|_{\omega=\omega_{sp}}$ [RDSF+10]. Some results using the quasi static approximation are given in Tabular 2.1.1. The resonance energies and the damping rates strongly depend on the permittivity of the medium surrounding the metal sphere. For gold as well as for the silver spheres the resonance energy of the dipole mode and their damping decreases for increasing permittivity of the surrounding medium. Since silver has a higher conductivity than gold, the damping of the dipole mode is much smaller in silver spheres than in gold spheres.

ε_{out}	gold sphere		silver sphere	
	resonance energy $\hbar\omega_{sp}$	damping rate γ_{sp}	resonance energy $\hbar\omega_{sp}$	damping rate γ_{sp}
1	2.5 eV	548 meV	3.5 eV	98 meV
1.77	2.4 eV	371 meV	3.1 eV	62 meV
3	2.2 eV	240 meV	2.8 eV	53 meV
5	2 eV	130 meV	2.5 eV	50 meV

Table 2.1 | Results for the resonances of the dipole mode and damping rates of gold and silver metal spheres for different dielectric backgrounds.

We used this approach, e.g., in [TCRK13], but needed a more elaborated approach do compare with experiments (see Chapter 5). Therefore, an approach considering also the size of the metal sphere is presented in the following.

2.1.2 Calculation of resonance energies and damping rates of metal spheres by using the Helmholtz equation

Now we follow an approach from Kolwas et al. and use a Helmholtz equation to obtain the damping rates and resonances of the plasmonic modes [KDD06, KD13]. Similar to the approach in the previous section, we start with the source free Maxwell equations. They read in the absence of free charges ρ_{free} and currents j_{free} :

$$\begin{aligned} \nabla \times \mathbf{H} &= \frac{\partial \mathbf{D}}{\partial t} & \nabla \cdot \mathbf{B} &= 0 \\ \nabla \times \mathbf{D} &= -\frac{\partial \mathbf{B}}{\partial t} & \nabla \cdot \mathbf{E} &= 0 \end{aligned} \quad (2.8)$$

\mathbf{B} and \mathbf{E} are the magnetic and electric field, respectively. \mathbf{j} and ρ are the induced currents and charge densities. Assuming a linear material response of the sphere on the electric-magnetic fields yields to the standard relations between the electric field and the electric displacement

$$\mathbf{D}(\mathbf{r}, \omega) = \mathbf{E}(\mathbf{r}, \omega) + \frac{\mathbf{j}(\mathbf{r}, \omega)}{\omega} \quad (2.9)$$

in frequency space. Since the metal sphere is a conductor, the relation between the induced current and the electric field is given by Ohm's law $\mathbf{j}(\mathbf{r}, \omega) = \sigma(\omega)\mathbf{E}(\mathbf{r}, \omega)$. Using Ohm's law, we can rewrite the electric displacement field

$$\mathbf{D}(\mathbf{r}, \omega) = \varepsilon_0 \left(1 + \frac{\mathbf{j}(\mathbf{r}, \omega)}{\varepsilon_0 \omega} \right) \mathbf{E}(\mathbf{r}, \omega) = \varepsilon_0 \varepsilon(\omega) \mathbf{E}(\mathbf{r}, \omega) \quad (2.10)$$

with material and frequency depending dielectric function $\varepsilon(\omega)$ of the metal sphere. It is assumed, that the surrounding media is nonconducting and nonmagnetic ($\sigma_{out} = 0$) and its dielectric function is independent of the frequency ($\varepsilon(\omega) = \varepsilon_{out}$). For the metal sphere the same dielectric function as for the bulk material is used. Assuming only time harmonic fields $\mathbf{E}(\mathbf{r}, \omega) = \mathbf{E}(\mathbf{r})e^{\dot{\mathbf{i}}\omega t}$, it is possible to obtain the Helmholtz equation for a metal sphere surrounded by a dielectric host material. Using Maxwell's equations (2.8) and the relation between the electric field and the electric displacement (2.10), it is possible to reduce the system of equations to the Helmholtz equation

$$\Delta \mathbf{E}(\mathbf{r}) + k^2 \mathbf{E}(\mathbf{r}) = 0, \quad (2.11)$$

here only transversal modes ($\nabla \cdot \mathbf{E} = 0$) are considered. $k_0 = \frac{\omega}{c}$ is the wave vector in vacuum, the actual wave vector depends on whether the Helmholtz equation is formulated for the inside of the sphere $k_{in} = k_0 \sqrt{\varepsilon_{in}}$, or outside the sphere (for the surrounding medium) $k_{out} = k_0 \sqrt{\varepsilon_{out}}$. The solution of the **scalar** Helmholtz equation

$$\Delta \psi(r, \theta, \Phi) + k^2 \psi(r, \theta, \Phi) = 0 \quad (2.12)$$

in spherical coordinates is given by spherical harmonics $Y_{lm}(\theta, \Phi)$ and spherical Bessel functions $j_l(k_{in} \cdot \mathbf{r})$ for the inside of the sphere and spherical Hankel functions $h_l(k_{out} \cdot \mathbf{r})$ for the surrounding material of the sphere [Jac99]. Now the solution for the vectorial Helmholtz equation (2.11) can be constructed by the use of the scalar solutions, considering only the solution with no radial component of the magnetic field [KDD06]:

$$\begin{aligned} \mathbf{E}(\mathbf{r}) &= B_{lm} \frac{1}{k} \nabla \times \nabla \times (\mathbf{r} \psi_{lm}(\mathbf{r}, \theta, \Psi)) \\ \mathbf{B}(\mathbf{r}) &= B_{lm} \frac{k}{\dot{\mathbf{i}}k_0} \nabla \times (\mathbf{r} \psi_{lm}(\mathbf{r}, \theta, \Psi)) \end{aligned} \quad (2.13)$$

with $\psi_{lm}(\mathbf{r}, \theta, \Psi) = j_l(k_{in} r) Y_{lm}(\theta, \Phi)$ for the inside of the sphere
and $\psi_{lm}(\mathbf{r}, \theta, \Psi) = h_l(k_{out} r) Y_{lm}(\theta, \Phi)$ for the outside of the sphere.

Kolwas et al. rewrite the solution with the same terminology as in [BW80], since there is no standard definition of the spherical Hankel and Bessel functions. The solutions inside the sphere are:

$$\begin{aligned} E_r(r, \theta, \Phi) &= B_{lm}^{in} \frac{l(l+1)}{k_{in} r} J_l(k_{in} r) \\ E_\theta(r, \theta, \Phi) &= B_{lm}^{in} \frac{[k_{in} r J_l(k_{in} r)]'}{k_{in} r} \frac{\partial Y_{lm}(\theta, \Phi)}{\partial \theta} \\ E_\Phi(r, \theta, \Phi) &= B_{lm}^{in} \frac{\dot{\mathbf{i}}m}{k_{in} r \sin \theta} [k_{in} r J_l(k_{in} r)] \\ H_r(r, \theta, \Phi) &= 0 \\ H_\theta(r, \theta, \Phi) &= B_{lm}^{in} \sqrt{\varepsilon_{in}} \frac{m}{\sin \theta} J_l(k_{in} r) Y_{lm}(\theta, \Phi) \\ H_\Phi(r, \theta, \Phi) &= \dot{\mathbf{i}} B_{lm}^{in} \sqrt{\varepsilon_{in}} J_l(k_{in} r) \frac{\partial Y_{lm}}{\partial \theta}. \end{aligned}$$

For the solution outside the sphere follows:

$$\begin{aligned}
 E_r(r, \theta, \Phi) &= B_{lm}^{out} \frac{l(l+1)}{k_{out}r} h_l(k_{out}r) \\
 E_\theta(r, \theta, \Phi) &= B_{lm}^{out} \frac{[k_{out}r h_l(k_{out}r)]'}{k_{out}r} \frac{\partial Y_{lm}(\theta, \Phi)}{\partial \theta} \\
 E_\Phi(r, \theta, \Phi) &= B_{lm}^{out} \frac{\dot{\mathbf{m}}}{k_{out}r \sin \theta} [k_{out}r h_l(k_{out}r)] \\
 H_r(r, \theta, \Phi) &= 0 \\
 H_\theta(r, \theta, \Phi) &= B_{lm}^{out} \sqrt{\varepsilon_{out}} \frac{m}{\sin \theta} h_l(k_{out}r) Y_{lm}(\theta, \Phi) \\
 H_\Phi(r, \theta, \Phi) &= \dot{\mathbf{m}} B_{lm}^{out} \sqrt{\varepsilon_{out}} h_l(k_{out}r) \frac{\partial Y_{lm}}{\partial \theta}.
 \end{aligned}$$

The ' denotes the derivation with respect to the argument of the function ($q_{in/out}r$). The continuity condition for the tangential component of the electric field at the surface of the metal sphere (E_θ, E_Φ) leads to

$$B_{lm}^{in} \frac{[k_{in}R J_l(k_{in}R)]'}{k_{in}R} = B_{lm}^{out} \frac{[k_{out}R h_l(k_{out}R)]'}{k_{out}R} \quad (2.14)$$

and the continuity condition for the tangential component of the magnetic field H_θ, H_Φ to

$$B_{lm}^{in} \sqrt{\varepsilon_{in}} J_l(k_{in}R) = B_{lm}^{out} \sqrt{\varepsilon_{out}} h_l(k_{out}R) \quad (2.15)$$

Due to the rotational symmetry, the continuity equations are independent of m . The combination of the continuity equations (2.14) and (2.15) only gives nontrivial solutions for the field amplitudes B_{lm} if

$$\frac{[k_{in}R J_l(k_{in}R)]'}{k_{in}R \sqrt{\varepsilon_{in}} J_l(k_{in}R)} - \frac{[k_{out}R h_l(k_{out}R)]'}{k_{out}R \sqrt{\varepsilon_{out}} h_l(k_{out}R)} = 0 \quad (2.16)$$

holds. The roots Ω_l of the continuity equation (2.16) need to be calculated numerically and are in principle complex $\Omega_l = \omega_{sp} + \dot{\mathbf{i}}\gamma_{sp}$, with the surface plasmon frequency ω_{sp} and the damping of the surface plasmon γ_{sp} for a given mode l . These attributes depend on the size of the metal sphere (radius R) and on the dielectric function of the surrounding medium. Furthermore, they depend on the used dielectric function of the metal sphere, whether one uses a single Lorentzian approximation, e.g., Drude model, or a more accurate fit to the experimental data like a multi Lorentzian approximation [ELRM06].

In Figure 2.2 (left) the resonance energies of the dipole mode versus the radius of the metal sphere is shown. It is obviously, that different fit functions for the dielectric function $\varepsilon(\omega)$, namely Drude model (2.1), Drude model with surface scattering (2.3) and multi Lorentzian fit (2.2), result in different resonance energies. While the Drude models, with and without surface scattering, only show small derivations for very small spheres, their discrepancy to the multi pole fit is quite large for the resonance energy of the dipole transition (Figure 2.2, left). All three fits lead to decreasing resonance energies for increasing radius of the metal sphere [SKD12].

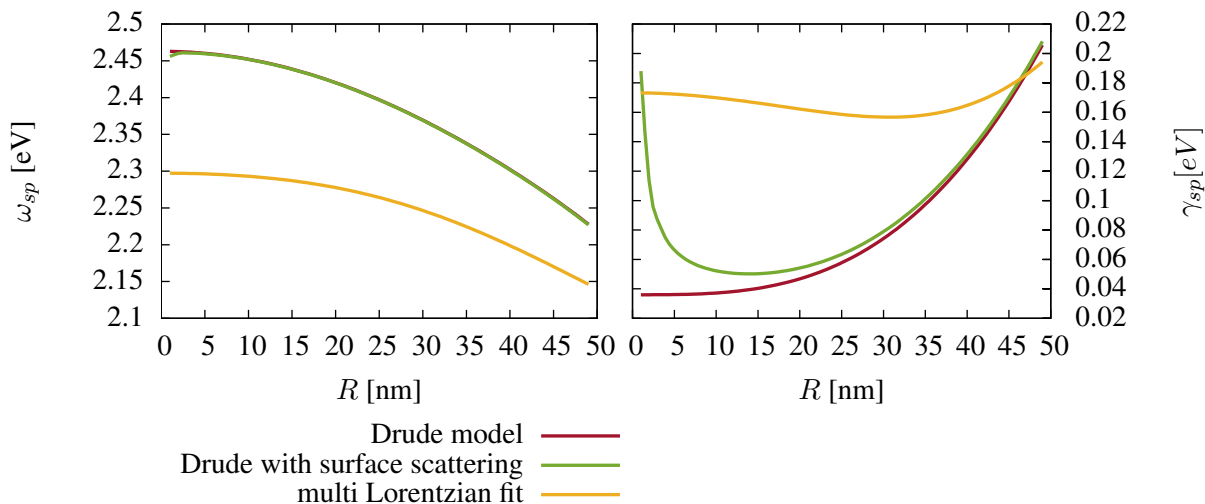


Figure 2.2 | Comparison of the resonance energy ω_{sp} of the dipole mode versus the radius R of the sphere (left) and the damping rate γ_{sp} versus the radius (right) for different dielectric functions to model the bulk material (Au). The sphere is embedded in a dielectric medium with $\epsilon_{out} = 1.77$, valid, e.g., for water.

The results for the damping rates vary way more than for the energies. The Drude fits, with and without surface scattering, become equal for larger radii of the sphere. For small spheres the included surface scattering plays an important role and increases the scattering significantly in the case of the Drude fit with surface scattering. Although there is no surface scattering included phenomenologically in the multi Lorentzian fit, the damping rate slightly increase for decreasing radius of the metal sphere. This behavior is more pronounced for a lower permittivity ϵ_{out} . Comparing the theoretical results with the experiments done in the group of Holger Lange (in submission), the spectra calculated using the multi Lorentzian fit show a way more striking agreement with the experimental ones, than the ones with the Drude or Drude model with surface scattering. This is caused by the disagreement of the Drude fit to the real/measured dielectric function of gold in the range from 2eV up to 2.5eV. For dipole transition energies above 2eV, one should use a multi Lorentzian fit to obtain descent results.

For a higher permittivity of the surrounding medium $\epsilon_{out} = 5$, the results for the dipole transition energy and the corresponding damping rate of the three used fits approach the same values (c.p. Figure 2.4). Higher permittivity of the surrounding medium leads to lower energies of the dipole transition. The Drude fit is pretty good for dipole transitions below 2eV (c.p. Figure 2.1), as well as the multi Lorentzian. Therefore, the Drude and the multi Lorentzian fit yield the same result. Only the Drude fit with a phenomenological surface scattering rate included, results in different values of the damping rate especially for small spheres, smaller than 10nm (c.p. Figure 2.4 right).

Considering Equation 2.16, it is easy to calculate resonance energies and damping rates for higher l modes ($l > 1$), corresponding to the quadrupole mode, octopole mode and so on and so forth. A discussion for higher modes can be found in [KDD06], where they used a Drude model with surface scattering to describe the dielectric function of the metal. In this work, we do not include higher order modes. This is possible since two approximations holds:

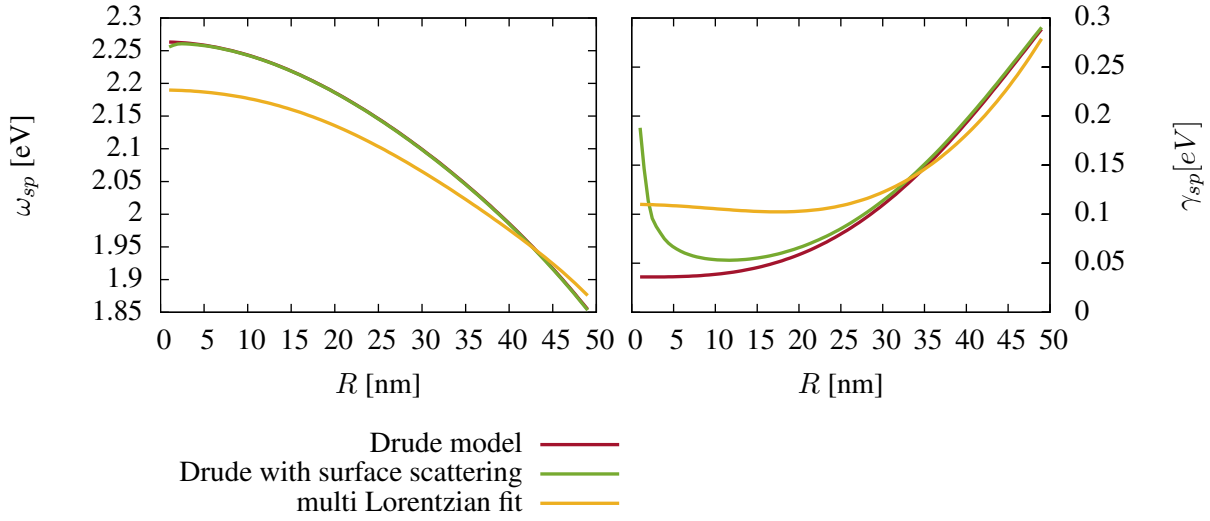


Figure 2.3 | Comparison of the resonance energy ω_{sp} of the dipole mode versus the radius R of the sphere (left) and the damping rate γ_{sp} versus the radius (right) for different dielectric functions to model the bulk material (Au). The sphere is embedded in a dielectric medium with $\varepsilon_{out} = 3$.

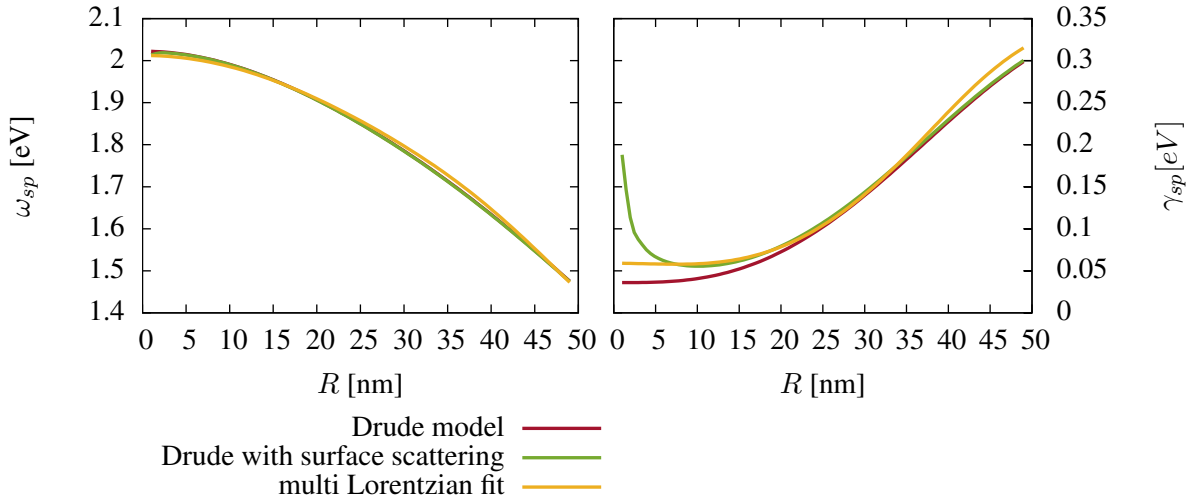


Figure 2.4 | Comparison of the resonance energy ω_{sp} of the dipole mode versus the radius R of the sphere (left) and the damping rate γ_{sp} versus the radius (right) for different dielectric functions to model the bulk material (Au). The sphere is embedded in a dielectric medium with $\varepsilon_{out} = 5$.

First, the quasi static approach. As long as the metal spheres are way smaller, only the dipole mode is excited by the external optical field. Thus, only the dipole mode couples to the far field and is detected, all higher modes are dark. Second, due to the quasi static approach the only way to excite higher order modes is via the near field of the quantum dots used to build the hybrid systems investigated later in this work (Chapter 4 and 5). It was shown, that this

near field excitation of higher order plasmon modes is only important, if the distance between the quantum dots and the metal sphere is smaller than the diameter of the metal spheres. We ensure, that this distance is always at least the diameter and therefore, the dipole approximation holds.

Beside the approaches discussed above, more elaborated approaches exist using, e.g., density functional theory [LK70] or a hydrodynamic model for the free electrons in the metal [Boa82]. It was shown experimentally and using a nonlocal hydrodynamic model for the free electrons that silver spheres with a diameter smaller than ≈ 10 nm exhibit a blue shift of about 0.5 eV compared to larger spheres (25 nm) [RYS⁺13, RSK⁺13]. Furthermore, the hydrodynamical model can be used to quantize plasmons [RW69], e.g., in spheres [CR68]. However, we describe systems where the blue shift does not play an important role since the sphere diameter is too large.

Chapter 3

Quantum mechanical theory

In this chapter, we briefly introduce some of the quantum mechanical concepts used within this thesis. We introduce the source field expression used to connect the microscopic system operator with the far field detected by a detector far away from the system. Under certain approximations, the detected signal is directly proportional to the system operators with a certain time delay. Furthermore, we give a general introduction to the Fano effect for a classical and quantum mechanical system.

3.1 Source field expression

In the following part, we describe different systems within the formalism of second quantization. To do so, we use operators to describe, e.g., the excitons and plasmons, which are excited in the quantum dots and the metal spheres. These operators describe the dynamics within the particles involved, but this dynamics cannot be measured directly. Therefore, some theory is needed to connect the quasi-particle operators of the considered hybrid systems to the free modes, which can for instance travel to a detector and be measured. This connection is granted by the so called source field expression.

We apply the source field expression to the plasmons, which represent the dipole excitation of the metal sphere. We mainly follow [Lou83], a similar approach of a source field expression for cavities can be found in [Car93].

We assume the metal sphere is at the origin of our coordinate system and in vacuum or at least in a medium, which has a dielectric function independent of the frequency in the range of interest. Furthermore, we expect the external electric field to be in the vacuum state. Without loss of generality, we assume the detector is somewhere on the z -axis. Therefore we are only interested in the electric field on the z -axis. The field outside the metal sphere is expressed via Heisenberg operators for the electric field operator $\mathbf{E}(z, t)$, which are usually split into a positive $\mathbf{E}^+(z, t)$ and a negative $\mathbf{E}^-(z, t)$ frequency part [Mil94]

$$\mathbf{E}(z, t) = \mathbf{E}^+(z, t) + \mathbf{E}^-(z, t) \quad (3.1)$$

with

$$\mathbf{E}^+(z, t) = \sum_{\mathbf{k}} \sum_{\lambda} \hat{\mathbf{e}}_{\lambda, \mathbf{k}} \sqrt{\frac{\hbar \omega_{\mathbf{k}}}{2 \epsilon_0 V}} c_{\mathbf{k}, \lambda}(t) e^{i \mathbf{k} \cdot \mathbf{r}}. \quad (3.2)$$

The negative frequency part is given by hermitian adjoining the positive frequency part $\mathbf{E}^-(z, t) = (\mathbf{E}^+(z, t))^\dagger$. The field outside the metal sphere is modeled as a reservoir of several modes with wave vector \mathbf{k} and polarization direction $\mathbf{e}_{\lambda, \mathbf{k}}$. The operator $c_{\mathbf{k}, \lambda}$ destroys a photon with wave vector \mathbf{k} and polarization λ . $\hbar\omega_{\mathbf{k}}$ is the energy of the photon annihilated and V the quantization volume.

To bridge between the dynamics of the plasmons and the photons of the reservoir, we need to calculate the equation of motion for the reservoir operator $c_{\mathbf{k}, \lambda}(t)$. Therefore, we introduce the free Hamiltonian of the reservoir and of the dipole plasmon mode

$$H_0 = \sum_{\mathbf{k}, \lambda} \hbar\omega_{\mathbf{k}, \lambda} c_{\mathbf{k}, \lambda}^\dagger c_{\mathbf{k}, \lambda} + \hbar\omega_{sp} a^\dagger a \quad (3.3)$$

with the photon energy $\hbar\omega_{\mathbf{k}, \lambda}$ for the photonic reservoir modes. a^\dagger and a are the creation and annihilation operator for the plasmonic dipole mode of a metal sphere, respectively. The interaction Hamiltonian between the plasmonic dipole mode and the reservoir results from a canonical mode quantization of the free electric field [Lou83] as

$$H_{int} = \sum_{\mathbf{k}, \lambda} \hbar \left(g_{\mathbf{k}, \lambda}^* a c_{\mathbf{k}, \lambda}^\dagger + g_{\mathbf{k}, \lambda} a^\dagger c_{\mathbf{k}, \lambda} \right) \quad (3.4)$$

with the coupling parameter between the electrical field and the dipole $g_{\mathbf{k}, \lambda} = e\sqrt{\frac{\omega_{\mathbf{k}}}{2\varepsilon_0\hbar V}} \mathbf{e}_{\mathbf{k}, \lambda} \cdot \mathbf{D}$. Here, \mathbf{D} denotes the vectorial dipole moment of the plasmons.

The equation of motion for the reservoir photons follows by using the Heisenberg equation of motion and the Hamiltonians ((3.3) - (3.4)) as

$$\dot{c}_{\mathbf{k}, \lambda} = -\dot{\imath}\omega_{\mathbf{k}, \lambda} c_{\mathbf{k}, \lambda} - \dot{\imath}g_{\mathbf{k}, \lambda}^* a. \quad (3.5)$$

This equation of motion can be integrated formally using the formalism of constant coefficient to

$$c_{\mathbf{k}, \lambda}(t) = c_{\mathbf{k}, \lambda}(0) e^{-\dot{\imath}\omega_{\mathbf{k}} t} - e\sqrt{\frac{\omega_{\mathbf{k}}}{2\varepsilon_0\hbar V}} \mathbf{e}_{\mathbf{k}, \lambda} \cdot \mathbf{D} \int_0^t dt' a(t') e^{\dot{\imath}\mathbf{k} \cdot \mathbf{R} + \dot{\imath}\omega_{\mathbf{k}} t'} \quad (3.6)$$

with the initial condition for the electric field operator $c_{\mathbf{k}, \lambda}(0)$.

Now we insert the formal solution $c_{\mathbf{k}, \lambda}(t)$ into Equation 3.2 and express the sum over \mathbf{k} as an integral $\sum_{\mathbf{k}} \rightarrow \frac{V}{(2\pi)^3} \int d\mathbf{k}$ [HK09]. The \mathbf{k} integral is written in spherical coordinates. We omit the $\mathbf{k}(0)$ term, since it only describes the free propagation of the electric field. The equation for the source field reads:

$$\mathbf{E}^+(z, t) = -\frac{\dot{\imath}e}{2(2\pi)^3\varepsilon_0} \sum_{\lambda} \int d\mathbf{k} \omega_{\mathbf{k}} \mathbf{e}_{\mathbf{k}, \lambda} (\mathbf{e}_{\mathbf{k}, \lambda} \cdot \mathbf{D}) \int_0^t dt' a(t') e^{-\dot{\imath}\mathbf{k} \cdot (\mathbf{r} - \mathbf{R}) + \dot{\imath}\omega_{\mathbf{k}}(t' - t)}. \quad (3.7)$$

To solve the angular integrals, the dipole should be orientated in the x-z-plane with the angle Θ to the z-axis

$$\mathbf{D} = D(\sin \Theta, 0, \cos \Theta) \quad (3.8)$$

and the distance between the detector at r and the dipole at R on the z -axis is assumed to be very large. Thus, it is ensured that $k|r - R| \gg 1$ holds. Using this assumptions and the fact that at this large distance the polarization of the transfers dipole field is parallel to the x -axis, the angular integration results in several e -functions with arguments of $|r - R|$ inverse in first, second and third order. Since $k|r - R| \gg 1$ holds, only the first order is kept. These two remaining e -functions result in two delta-functions by integrating over k . In the end, after the delta-functions has been evaluated, the final result for the positive electric field operator is [Lou83]:

$$E^+(\mathbf{r}, t) = -\frac{e\omega_{sp}^2 D \sin \Theta}{4\pi\epsilon_0 c^2 |r - R|} \dot{a} \left(t - \frac{|r - R|}{c} \right). \quad (3.9)$$

Obviously, this result for the electric field at, e.g., the position of the detector is direct proportional to the creation (a^\dagger) and annihilation (a) operators of the plasmonic dipole mode. Therefore, it is convenient to describe the system by the operators of the single constituents, namely the exciton and plasmon operators. In the same manner a source field expression for the excitonic operators can be introduced. This is possible, since the coupling between the external electric field and the excitons is of the form of a dipole-dipole coupling. Again, one need to ensure that the same assumptions hold. The resulting electric field operator (3.9) shows retardation due to the distance between the dipole and the detector. This retardation effects does not play a role, e.g., in the steady state spectra we are interested in (cp. Chapter 4). Furthermore, the retardation only shifts the time dynamics of the pumped hybrid system investigated in, e.g., Section 5.4. This offset does not change the physical interpretation of our results.

3.2 Fano effect

In this section we introduce the Fano effect. This effect is named after Ugo Fano, who was the first giving a theoretical description [Fan35, Fan61]. He explained the occurrence of asymmetric peaks in the spectra of noble gases [Beu35]. Typical for this effect is the occurring of asymmetrical line shapes in the spectra. This asymmetry can be traced back to the interference of two different excitations. The Fano effect has been found in several systems, e.g., quantum dots [CWB01, GGGH⁺00, GZL⁺08], in photonic crystal cavities [CY03, GPB⁺09] and quantum wells [AAGG07]. It has additionally been investigated in doped semiconductors [BCC⁺97], semiconductors in magnetic fields [BAKM⁺97] and has been used to prove the forming of quasi particles in semiconductors [LIH06]. It also occurs in carbon nanotubes [HYD06, BS04]. The most interesting case for this thesis is the occurrence of the Fano effect in metal nanoparticles dimers [BRAB⁺08], aggregates [MBN09] and hybrid systems [ZG11, ZGB06, RDSF⁺10]. Furthermore, the Fano effect occurs in coupled nanoplasmonic structures [VSS⁺09] and is tunable by symmetry breaking in plasmonic nanostructures [HSD⁺08].

In the following, we explain the generation of this asymmetry generally for a system of two classical oscillators and a coupled quantum mechanical system. For the classical system we use two pendulums, where the first one is driven by an external force [JSK06]. We explain the Fano effect for the quantum mechanical system using a hybrid system consisting of a metal sphere and a quantum dot. In Chapter 4, we discuss Fano effect for a realistic system. There, we determine the coupling strength, the parameters of the constituents of the hybrid and investigate the influence of several quantities on the Fano effect.

3.2.1 Classical Fano effect

We start with a mechanical analogy to the Fano effect [JSK06]. We consider two pendulums coupled by a weak spring to each other, the left pendulum is driven by an external force (c.p. Figure 3.1 left). Assuming only small amplitudes of the pendulum elongation, the equations of motions for the amplitudes x_1 and x_2 reads [JSK06]:

$$\begin{aligned} \frac{d^2}{dt^2}x_1 + \frac{d}{dt}\gamma_1x_1 + \omega_1^2x_1 + gx_2 &= de^{i\omega t} \\ \frac{d^2}{dt^2}x_2 + \frac{d}{dt}\gamma_2x_2 + \omega_2^2x_2 + gx_1 &= 0 \end{aligned} \quad (3.10)$$

with the damping γ , the resonance frequency ω and the coupling between the pendulums g . We solve this equations of motions numerically into the steady state for several excitation frequencies of the driving force and obtain the spectrum shown in Figure 3.1 on the right. We choose resonance energies $\omega_1 = 1$ for the driven pendulum and $\omega_2 = 1.2$ for the right one. For the damping of the pendulum we chose $\gamma_1 = 0.025$ and $\gamma_2 = 0.01$, the coupling between both is set to $g = 0.5$ and for the coupling of the first pendulum to the external force we use $d = 0.5$.

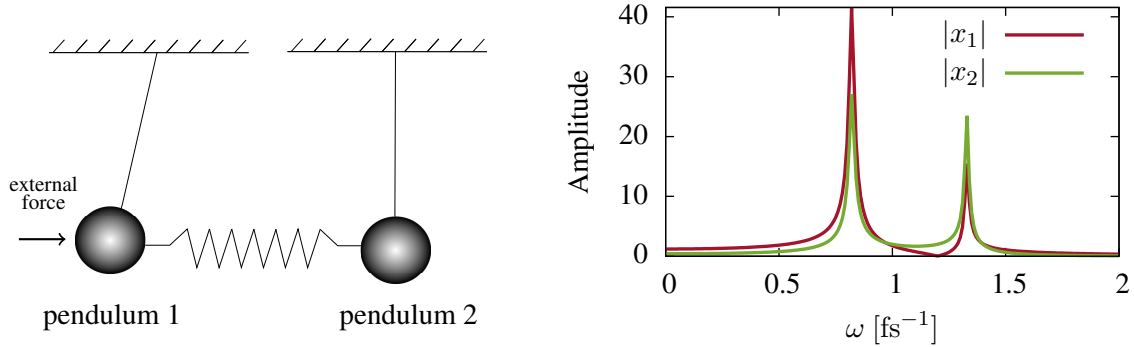


Figure 3.1 | Left: Sketch of the mechanical system. **Right:** Spectrum of the pendulum amplitudes $|x_1|$ and $|x_2|$ versus the frequency of the driving force acting on the first pendulum.

Due to the coupling between both pendulums, the eigenfrequencies of the uncoupled pendulum are shifted away from each other. This shift scales with the coupling strength between the pendulum. We discuss these coupling induced shifts in more detail in, e.g., Section 4.5.2 and 4.5.3 for quantum mechanical systems. While the amplitude of the right pendulum, the non driven one, has a symmetric spectrum (Fig. 3.1 green curve), the spectrum of the driven pendulum shows a asymmetry at $\omega = 1.2\text{fs}^{-1}$, the resonance frequency of the right pendulum, which is not driven by an external force. This asymmetry can be understood as Fano resonance. It is possible to give an intuitive explanation for this resonance in the case of a mechanical system. While increasing the frequency of the driving force towards the resonance energy of the left pendulum ($\omega = 1\text{fs}^{-1}$), the amplitudes increases. For frequencies higher than the resonance frequency of pendulum 1, the amplitude decrease. It is worth to mention, that the phase of the amplitude is turned by π above the eigenfrequency of pendulum 1 [JSK06]. Increasing the driving frequency further excites swinging of the second pendulum. Due to the phase

shift of the oscillation from the first pendulum, the oscillations between the eigenfrequencies ($1\text{fs}^{-1} < \omega < 1.2\text{fs}^{-1}$) are phase shifted by π . Therefore, both oscillations, from pendulum 1 and pendulum 2, interfere destructively causing the Fano resonance at $\omega = 1.2\text{fs}^{-1}$. This resonance is clearly visible in Figure 3.1 on the right for the amplitude of the first pendulum $|x_1|$ (red curve). Increasing the driving frequency further starts to drive the second pendulum and the amplitude rise at the shifted frequency of pendulum 2, second peak in the spectrum for $|x_1|$. After the shifted resonance, the amplitude decreases again.

3.2.2 Quantum mechanical Fano effect

We investigate a quantum mechanical system consisting of a continuous system (metal sphere) and a two level system (quantum dot) sketched in Figure 3.2 on the left. We describe both within the dipole approximation, which results in a dipole-dipole coupling between both constituents of the hybrid system. In contrast to the two level system, the excited state of the metal sphere is broadened by a huge damping. Therefore, the broadened excited state behaves like a continuous system with several states. In Chapter 4 we discuss the Fano effect in a system consisting of two quantum dots coupled to a metal sphere. There, we will also investigate the influence of the system parameters on the Fano effect in more detail. Here, we will give a general overview of the Fano effect in quantum mechanical systems and an explanation why it occurs.

To calculate a spectra similar to the classical one in Figure 3.1, we start with the derivation of the equations of motions for a metal sphere coupled to a quantum dot. We use the Hamilton operator and Lindblad terms introduced in Section 4.2 with the operator equation 4.19 to obtain the equations of motion. For the plasmon probability $\langle |n\rangle\langle p| \rangle$ we find:

$$\begin{aligned}
 \partial_t \langle |n\rangle\langle p| \rangle = & \left(\dot{\mathbf{i}}(n-p)\omega_{sp} - \frac{\gamma_{sp}}{2}(p+n) \right) \langle |n\rangle\langle p| \rangle + \gamma_{sp}\sqrt{p+1}\sqrt{n+1} \langle |n+1\rangle\langle p+1| \rangle \\
 & - \dot{\mathbf{i}}g\sqrt{n+1} \langle \rho_{vc}|n+1\rangle\langle p| \rangle + \dot{\mathbf{i}}g^* \sqrt{p+1} \langle \rho_{vc}|p+1\rangle\langle n| \rangle^* \\
 & + \dot{\mathbf{i}}g\sqrt{p} \langle \rho_{vc}|n\rangle\langle p-1| \rangle - \dot{\mathbf{i}}g^* \sqrt{n} \langle \rho_{vc}|p\rangle\langle n-1| \rangle^* \\
 & - \frac{\dot{\mathbf{i}}}{\hbar} \chi E(t) \sqrt{n+1} \langle |n+1\rangle\langle p| \rangle + \frac{\dot{\mathbf{i}}}{\hbar} \chi^* E(t)^* \sqrt{p+1} \langle |n\rangle\langle p+1| \rangle \\
 & + \frac{\dot{\mathbf{i}}}{\hbar} \chi E(t) \sqrt{p} \langle |n\rangle\langle p-1| \rangle - \frac{\dot{\mathbf{i}}}{\hbar} \chi^* E(t)^* \sqrt{n} \langle |n-1\rangle\langle p| \rangle.
 \end{aligned} \tag{3.11}$$

The first lines originates from the free Hamiltonian and the Lindblad terms. This line accounts for the free evolution of the system with the plasma frequency ω_{sp} and damping by γ_{sp} . Energy relaxation is included by the last term in the first line, which is a pump term driven by the higher (+1) excited plasmonic state. The second and third line couples the plasmon probability to the quantum dot, or more precisely to the polarization ρ_{vc} of the quantum dot. The coupling strength between the metal sphere and the quantum dot is denoted by g . In the last two lines the interaction with the external optical field $E(t)$ is included. The external optical field couples via the plasmonic dipole moment χ to the plasmonic system.

Beside the plasmon probability we need additional equations of motions for the excitonic quantities, namely the polarization ρ_{vc} and the conduction band density n_c . We write both quantities as plasmon assisted polarization and plasmon assisted density. Therefore, higher

order excitonic and plasmonic correlations are included. This yields for the plasmon assisted polarization:

$$\begin{aligned}
 \partial_t \langle \rho_{vc} | n \rangle \langle p | \rangle = & \left(\dot{\mathbf{i}}(n-p)\omega_{sp} - \dot{\mathbf{i}}\omega_{g1} - \frac{\gamma_{sp}}{2}(p+n) - \frac{\gamma_g}{2} \right) \langle \rho_{vc} | n \rangle \langle p | \rangle \\
 & - \frac{\dot{\mathbf{i}}}{\hbar} \mu E(t) (\langle n_c | n \rangle \langle p | \rangle - \langle n_v | n \rangle \langle p | \rangle) + \gamma_{sp} \sqrt{p+1} \sqrt{n+1} \langle \rho_{vc} | n+1 \rangle \langle p+1 | \rangle \\
 & - \dot{\mathbf{i}}g^* \sqrt{n} \langle n_c | n-1 \rangle \langle p | \rangle + \dot{\mathbf{i}}g^* \sqrt{p+1} \langle n_v | n \rangle \langle p+1 | \rangle \\
 & - \frac{\dot{\mathbf{i}}}{\hbar} \chi^* E(t)^* \sqrt{n} \langle \rho_{vc} | n-1 \rangle \langle p | \rangle + \frac{\dot{\mathbf{i}}}{\hbar} \chi E(t) \sqrt{p} \langle \rho_{vc} | n \rangle \langle p-1 | \rangle \\
 & + \frac{\dot{\mathbf{i}}}{\hbar} \chi^* E(t)^* \sqrt{p+1} \langle \rho_{vc} | n \rangle \langle p+1 | \rangle - \frac{\dot{\mathbf{i}}}{\hbar} \chi E(t) \sqrt{n+1} \langle \rho_{vc} | n+1 \rangle \langle p | \rangle.
 \end{aligned} \tag{3.12}$$

Since the excitonic polarization is plasmon assisted, damping and driving terms occur due to the Lindblad terms for the plasmonic system. Nevertheless, for the special case of $n = p = 0$ all these terms cancel out and the equation of motion for the excitonic polarization remains. The assisted excitonic polarization is coupled via the excitonic dipole moment μ and the electric field to the conduction and valence band. The coupling g between the quantum dot and the metal sphere couples the assisted excitonic polarization to plasmonic transition (third line). The last two lines describe the interaction of the plasmons ($|n\rangle\langle p|$) with the external optical field. Since the equation of motion for the conduction band density is pretty the same as for the polarization, we regard it to the Appendix [B.1](#).

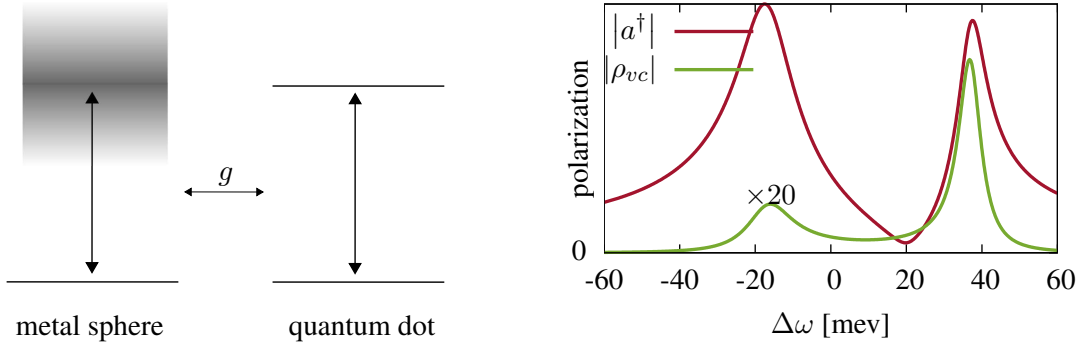


Figure 3.2 | Left: Energy scheme of the hybrid system consisting of a metal sphere and a quantum dot. Both are coupled via g . **Right:** Spectra of the steady state for different excitations energies. Plotted are the absolute values of the plasmonic $|a^\dagger|$ and the excitonic $|\rho_{vc}|$ polarization. The metal sphere diameter is 10nm as well as the distance between the constituents. The metal sphere resonance is at $\Delta\omega = 0$ meV and the quantum dot one at $\Delta\omega = 20$ meV. Note, the excitonic polarization is multiplied by 20.

We solve the equations of motions into the steady state for several detunings $\Delta\omega$ to obtain the spectra in Figure [3.2](#) on the right. $\Delta\omega$ is the detuning between the excitation frequency of the external optical field ($E(t)$) and the plasmonic resonance. Therefore, the plasmonic resonance is consequently at $\Delta\omega = 0$ meV. The excitonic transition energy is detuned with respect to the plasmonic one and appears at $\Delta\omega = 20$ meV. The peaks apparent in the spectra

are pushed apart from each other by the interaction between the quantum dot and the metal sphere, due to the newly formed eigenstates in the hybrid system. These states are discussed in Section 4.5.1 - 4.5.3 in more detail for a hybrid system consisting of a metal sphere and one or two quantum dots.

The spectrum plotted in Figure 3.2 on the right shows the absolute value of the plasmonic $|a^\dagger|$ and excitonic $|\rho_{vc}|$ polarization versus the detuning of the plasmonic resonance and the external optical field. While the excitonic polarization shows symmetric peaks, the plasmonic polarization exhibits an asymmetric dip at the resonance frequency of the uncoupled excitonic system ($\Delta = 20\text{meV}$). This dip is caused by the Fano effect, which occurs due to destructive interference between two possible excitation channels. In this case, the excitation from the ground state to the excited plasmonic state and from the ground state into the excited exciton state. Between the resonances of both constituents of the system, these two possible excitations interfere destructively at $\Delta = 20\text{meV}$ giving rise to the asymmetric dip. Similar to the classic case one could argue, that the mainly driven system is the plasmonic one, since the dipole is orders of magnitude larger (at least one) than the excitonic one. Therefore, the plasmonic transition is driven strongly and excites the excitonic transition for excitations frequencies of the external optical field above the plasmonic resonance. Above this resonance, the plasmonic and excitonic excitation interfere destructively and thus give rise of the asymmetric dip at $\Delta = 20\text{meV}$.

Part III

Quantum dots coupled to a metal sphere

Chapter 4

Two quantum dots coupled to a metal nanoparticle

In this chapter, we develop a model for a hybrid system consisting of quantum dots and a metal sphere. These hybrid systems are intensively studied experimentally and theoretically, since they are capable of combining the advantages of both constituents. The metal particles, for instance, are capable of focusing light into the sub-wavelength scale. This can be used for miniaturization of light based technologies [KAP15], e.g., of on chip sensing [LD13] and in fiber optics [Sla98]. The quasi-particles of these strongly focused electric fields are named plasmons [Sto11, SKD12]. Plasmons can be spatially localized [CRBSP15, CSG14] or propagate along a surface [GJH⁺15]. In the following we focus on localized plasmons which are excited on a metal sphere. The combination of metal particles and quantum dots for example, opens new possibilities for applications. Promising applications are, e.g., ultra-sensitive [GG09] and biosensing [NHL⁺08]. Furthermore, it is possible to enhance the efficiency of light harvesting complexes [ZLPW⁺15, LKL⁺15, DQK⁺13, ALA⁺10]. Also devices for quantum information processing with plasmons are possible [FLKA14, TMO⁺13, CSHL06]. Another interesting field is the use of plasmons as a cavity for the amplification of stimulated emission of radiation, or short Spaser (surface plasmon amplification of stimulated emission of radiation). This Spaser was proposed theoretically by Bergman and Stockman [BS03]. In 2009 Noginov et. al. claimed the demonstration of such a laser device [NZB⁺09]. However, it is discussed very controversially whether such a device is possible or not. Using semi-classical theories the existences of a Spaser is found to be very unlikely or even unattainable [KS14, KS12, ZL13]. Similar results are found using full quantized theories with different assumptions and simplifications [RGTK15, Pro12, VAP⁺12, PV14].

This chapter is organized as follows: We start with a brief introduction of the system (Section 4.1) and set up a Hamiltonian in second quantization (Section 4.2). We derive the required parameters of the Hamiltonians, i.e. the coupling parameters and the plasmon properties according to Chapter 2. Using an operator equation and the Hamilton operators, we evaluate the equation of motion and define our observables of interest (Section 4.3). The equations of motions are solved numerically for certain cases: We considered pulsed and continuous wave excitations of the hybrid system and investigate the Rayleigh scattering (Section 4.4.1) and the emission statistics (Section 4.4.2). Furthermore, we investigate the τ -dynamics of the second order correlation function in Section 4.4.2.

Beside the temporal behavior, we analyze the spectra of the statistics and the Rayleigh scattering. One focus is on the influence of the Förster interaction on both spectra. While the Rayleigh scattering spectra are barely influenced (Section 4.5.1 ff.), the emission statistics are very sensitive to changes of the Förster interaction between the quantum dots (Section 4.7). The statistics can be changed, e.g., from antibunched, to coherent and finally to a bunched statistic by only increasing the Förster interaction and keeping all other parameters constant. We trace this back to the newly formed states in the hybrid system due to the interactions between the constituents. The Förster interaction between the quantum dots shifts the new eigenenergies and redistributes the dipole moments for certain transitions between excitation manifolds. This leads to the huge changes in the emission statistics of the hybrid system although the Förster interaction is quite weak between the quantum dots (<1 meV) compared to the, e.g., damping rates (21 meV) and coupling strength between the excitons and plasmons (up to 38 meV).

4.1 Introduction

We investigate a hybrid system consisting of a silver sphere and two quantum dots. We include coupling between the quantum dots and coupling between the excitons, formed in the quantum dots, and the plasmons, excited on the silver sphere. This dipole-dipole coupling is mediated by the Coulomb force and called Förster interaction. To avoid confusion, we will only name the interaction between the quantum dots Förster interaction but not the interaction between the plasmons and excitons.

The observables of interest are the Rayleigh scattering and the second order correlation function, also named $g^{(2)}$ -function. We investigate these observables in time domain, where we consider different excitation of the system, and in frequency domain.

A sketch of the system is shown in Figure 4.1. The distance between the two quantum dots and the silver sphere is D and the angle between the system axis and the incident field is θ .

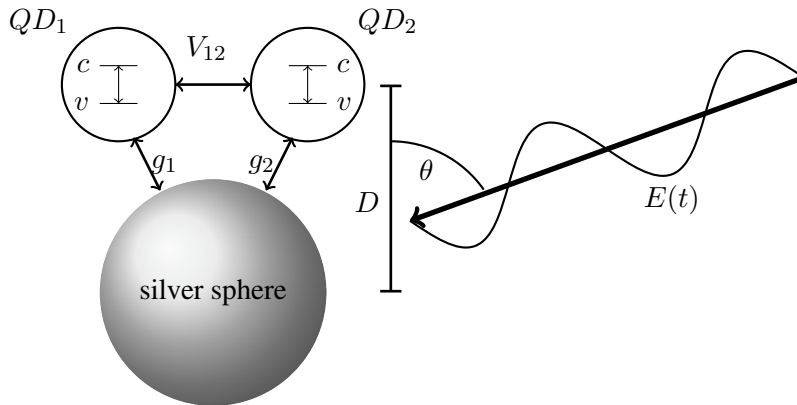


Figure 4.1 | Sketch of the system including the coupling between the quantum dots V_{12} , between the quantum dots and silver sphere $g_{1/2}$ and the external electrical field $E(t)$. θ denotes the angle between the system axis and the external electrical field.

We describe the coupled system within the formalism of second quantization. The quantum dots are modeled by their dominant exciton and the silver sphere is described by the lowest plasmon mode, the dipole mode. Thus, we can model the whole system and the occurring

interactions between constituents within the dipole approximation. It has been shown that this approximation yields the same result as an theory incorporating higher order plasmon modes, as long as the diameter of the silver sphere is equal or smaller than the distance between the silver sphere and the quantum dots [VVKH12]. This ensure that no higher order plasmon modes are excited due to the interaction between quantum dot and silver sphere. Another possible way to excite higher order plasmon modes is by excitation of the external optical field. This is, e.g., included in the Mie theory [Mie08, KCZ+03]. To avoid this, the size of the silver sphere needs to be much smaller than the wavelength of the incident light field to ensure the validity of the quasi static approach [YZD+08]. Considering the dominant exciton only, the possible states for an electron are in the valence band v or the conduction band c , as depicted in Figure 4.1.

We assume the same distance of both quantum dots to the silver sphere and similar angels. Therefore, both quantum dots couple with the same strength to the plasmonic modes. Since the Förster interaction is mediated by the Coulomb force, we can alter their strength by varying the distance between the two QDs. We ensure that the wavelength of the exciting external optical field is way larger than the diameter of the silver sphere, thus the quasi static approach holds [ZGB06]. Furthermore, the distance between the quantum dots and between the quantum dots and the silver sphere should not undergo 1 nm. If this is the case, processes requiring spatial overlap of the electron wave functions like tunneling and Dexter transfer [SKR15] becomes very unlikely and can be neglected. Therefore, we concentrate on the Coulomb induced energy transfer between the two quantum dots (V_{12}) and the Coulomb induced Dipole-Dipole energy transfer between the quantum dots and the silver sphere ($g_{1/2}$).

4.2 Hamilton operators

In this section we introduce the Hamilton operators and Lindblad terms used to calculate the equation of motion. The equation of motions to determine the observables of interest are introduced in the next section.

Within the formalism of second quantization we use the compound system Hamiltonian [TCRK13]

$$H = H_0 + H_{int} + H_{ext} + H_F, \quad (4.1)$$

with the free Hamiltonian of the quantum dot and the silver sphere H_0 the Hamiltonian for the interaction between the quantum dot and the silver sphere H_{int} [RDSF+10, WSI0], the Hamiltonian for the interaction between the hybrid system and the external optical field H_{ext} [RDSF+10, WSI0] and the Förster interaction between the quantum dots (i-th and j-th) H_F [DAFK06]. We formulate the Hamiltonians generally for a hybrid system consisting of one metal sphere and N QDs. Later we will restricted the equations to only two QDs.

The Hamiltonian for the noninteracting system

$$H_0 = H_{pl} + H_{exc} = \hbar\omega_{sp}a^\dagger a + \hbar \sum_i \omega_{ex_i} a_{c_i}^\dagger a_{c_i} \quad (4.2)$$

consists of the plasmonic and excitonic contributions, with the plasmon resonance frequency ω_{sp} , the creation a^\dagger and annihilation operator a for the plasmonic dipole mode. We ensure, by choosing an appropriate distance between the quantum dots and the silver sphere, that we need only to include the plasmonic dipole mode of the sphere. It was shown that as long as the distance between the quantum dot and the silver sphere is at least the diameter of the silver

sphere, higher plasmonic modes can be neglected [VVKH12] for the near field interaction. Furthermore, we assume the quantum dots and the plasmonic dipole mode to be almost in resonance, thus, higher plasmonic modes would couple less efficient to the quantum dots, since their resonance energy is higher than the one of the dipole mode [SKY09, SK11]. This detuning reduces the spectral overlap between the dipole modes and higher order modes, which than results in a less efficient coupling. As long as the quasi static approach holds (size of the silver sphere is way smaller than the wavelength of the external optical field) higher plasmon modes ($l > 1$) do not coupled to the optical far field and are not populated by the external field [SKY09]. Therefore, higher order plasmon modes only couple via the near field, but they do not influence the far field signal, in which we are interested in, directly [GVVY⁺13]. Due to all this reasons, we neglect higher order plasmon modes in our calculations.

The quantum dot is described by the dominant excitonic transition ω_{g_i} of the i -th quantum dot and the creation $a_{c_i}^\dagger$ and annihilation a_{c_i} operators for an electron in the conduction band of the i -th QD. Without loss of generality, we set the energy of the valence band to zero and can neglect its contribution.

We introduce the interaction Hamiltonian

$$H_{int} = - \sum_i g_i a_{v_i}^\dagger a_{c_i} a^\dagger + \text{h.a.} \quad (4.3)$$

in the rotating wave approximation. This approximation neglects non-energy conserving terms, e.g., $a_{c_i}^\dagger a_{v_i} a^\dagger$, which describes the creation of an plasmon and exciton. These processes are in principle possible due to the time-energy uncertain relation, but they are only important, if the resonance energies of the constituents are strongly detuned. Considering only a small detuning between quantum dots and the silver sphere, non-energy conserving terms cancel out by evaluating the expectation value of the observables. The non-energy conserving terms oscillate with the frequency $\omega_{sp} + \omega_{ex_i}$, while the energy conserving terms oscillate with the difference of the transition frequencies $\Delta = \omega_{sp} - \omega_{ex_i}$. Due to the fast oscillation of the non energy conserving terms, their influence on the expectation value is very small compared to the energy conserving terms. Therefore, averaging over time cancels out the influence of the fast oscillating/non energy conserving terms.

The interaction Hamiltonian with the external optical field

$$H_{ext} = -E_t \chi a^\dagger - \sum_i \mu_i E_t a_{c_i}^\dagger a_{v_i} + \text{h.a.} \quad (4.4)$$

describes creation and annihilation of plasmons and excitons by the external optical field, respectively. Again, we applied a rotating wave approximation to reduce the complexity of the Hamiltonian. The rotating wave approximation holds, since we ensure excitation of the hybrid system near resonance by the external optical field. χ denotes the dipole moment of the plasmonic mode and μ_i the dipole moment of the i -th quantum dot. The external optical field $E_t = E_0 e^{i\omega_{ext}t}$ is given by the amplitude E_0 and the excitation frequency ω_{ext} of the optical field. The amplitude of the external optical field $E_0 = \frac{\Omega}{2\mu_i}$ is defined through the Rabi energy Ω and the i -th excitonic dipole moment μ_i . For the considered CdSe quantum dots the dipole moment is 1.84 enm [EB97].

The coupling parameters of the metal sphere, dipole moment χ and the coupling to the dipole of the quantum dot g , are calculated following [RDSE⁺10, WS10]. Their approach to estimate the dipole-dipole coupling strength between a metal sphere and a quantum dot starts

with the calculation of the classical dipole fields of both constituents. Using the Clausius-Mossotti relation to connect the polarizability of a medium with its permittivity, they calculate the classical polarization field of the metal sphere at the position of the quantum dot. After deriving the formal solution of the equations of motion for the plasmon polarization $\langle a \rangle$ and the quantum dot polarization ρ_{vc} via a Fourier transformation, the classical and quantum mechanical expression are compared with each other. The comparison of both equations yields for the coupling

$$g_i = \frac{s_\alpha \mu_i}{R_m^3} \sqrt{\frac{3\hbar\eta R_m^3}{4\pi\epsilon_0}} \quad (4.5)$$

and

$$\chi = -\epsilon_{out} \sqrt{12\pi\hbar\eta\epsilon_0 R_m^3} \quad (4.6)$$

for the dipole moment of lowest plasmon mode of the metal sphere, the dipole mode. Here, R_m is the radius of the metal sphere, ϵ_{out} die permittivity of the medium surrounding the sphere and $s_\alpha = 3\cos^2\theta - 1$ accounts for the angle dependency of the coupling strength, where θ is the angle between the system axis and the external optical field. Since the dipole moment of the metal sphere is induced by the external optical field, the field determines directly the angle of the plasmonic dipole moment. Therefore, the angle between the quantum dot dipole moment and the external optical field s_α directly influences the coupling strength between the two dipoles. μ_i is the dipole moment of the i -th molecule and

$$\eta = \left(\frac{d(\operatorname{Re}[\epsilon(\omega)])}{d\omega} \Big|_{\omega=\omega_{sp}} \right)^{-1} \quad (4.7)$$

the inverse of the gradient of the dielectric function of the metal at the surface plasmon frequency ω_{sp} .

The last part in the system Hamiltonian H is the Förster interaction between the two quantum dot H_F [För48]. The interaction Hamiltonian

$$H_F = \sum_{\substack{i,j \\ i \neq j}} \left(V_{ij} a_{c_i}^\dagger a_{v_j}^\dagger a_{c_j} a_{v_i} + \text{h.a.} \right) \quad (4.8)$$

describes the energy transfer from the j -th quantum dot to the i -th quantum dot (first term) and the process vice versa (h.a. term). The coupling strength is given by the matrix element V_{ij} with a strength of up to 0.45 meV [LRNB03]. There are several cases where the Förster interaction plays an important role, e.g., for energy transfer on the nanometer scale [RAK+06] and in fluorescence resonance energy transfer microscopy [ND05] widely used in medicine and biology. In these fields the Förster interaction is used to investigate molecular interaction in cells [SP03] or for concentration measurements inside cells [MLH+97]. Furthermore, it was found that the Förster energy transfer rate between quantum dots can be enhanced by plasmons [GLK07, SZZ+10, KBR+08].

Using only the Hamilton operators mentioned above, the system energy would only increase since the system is permanently pumped by the external optical field. To describe a physical and realistic case, we introduce losses in the quantum dots and the silver sphere. These losses are caused, e.g., by electron-phonon coupling, radiative losses, pure dephasing and interaction with other electron reservoirs. In the silver sphere the main losses are due to ohmic

damping of the electrons. In the quantum dots coherent and incoherent quantities are damped by radiative losses. In addition, coherent quantities, like the polarization, are also damped by pure dephasing [Tak93]. We incorporate all damping mechanism by the use of Lindblad terms [BP02, WM08]. The Lindblad super-operator describing spontaneous emission reads

$$\begin{aligned}\mathfrak{L}_{sp} &= \frac{\gamma_{sp}}{2} \left(2a\rho a^\dagger - a^\dagger a\rho - \rho a^\dagger a \right) \\ \text{and } \mathfrak{L}_g &= \frac{\gamma_g}{2} \left(2\rho_{vc_i}\rho\rho_{vc_i}^* - \rho_{vc_i}^*\rho_{vc_i}\rho - \rho\rho_{vc_i}^*\rho_{vc_i} \right)\end{aligned}\quad (4.9)$$

for the plasmons (\mathfrak{L}_{sp}) and for the excitons (\mathfrak{L}_g), respectively. $\rho_{vc_i} = a_{v_i}^\dagger a_{c_i}$ is the polarization operator of the i -th QD. Furthermore, we included Lindblad terms for thermal emission

$$\mathfrak{L}_{emi} = \frac{\gamma_{sp}}{2} n_q \left(2a\rho a^\dagger - a^\dagger a\rho - \rho a^\dagger a \right) \quad (4.10)$$

and absorption

$$\mathfrak{L}_{abs} = \frac{\gamma_{sp}}{2} n_q \left(2a^\dagger \rho a - a a^\dagger \rho - \rho a a^\dagger \right) \quad (4.11)$$

for the plasmonic mode with the Bose-Einstein statistics n_q . This is regarded to the finite temperature of silver sphere, which enables thermal emission and absorption of plasmons. However, it turned out that the thermal emission and absorption of plasmons do not play a role at reasonable temperatures if the system is excited optically. Even very weak optical excitations dominate the plasmon and system dynamics. Thus, we omit the terms in the equations of motions in (B.2) - (B.10) to increase readability.

In Chapter 5 we will compare our theory to optical experiments. Therefore, we need to distinguish between pure and radiative dephasing. We regard this discussion to Chapter 5.

4.3 Observables of interest and equation of motion of the hybrid system

In this section, the observables of interest are introduced and their quantum mechanical equations of motion are derived. The observables of interest are the Rayleigh scattering and the second order correlation function ($g^{(2)}$ -function) of the hybrid system. In principle both of this observables are constructed by using the macroscopic polarization operator of the hybrid system

$$P_{mac} = P_{mic}^\dagger + \text{h.a.} = \chi a^\dagger + \sum_i \mu_i a_{c_i}^\dagger a_{v_i} + \text{h.a.} \quad (4.12)$$

which is given by the sum over the microscopic polarization operator of the system (P_{mic}). The microscopic polarization constitutes of the sum over the single polarizations of the constituents of the hybrid system.

The far field signal I_{far} for a hybrid system, using the source field expression (Section 3.1) for the emitted field [Lou83, Car93], reads

$$I_{far} = \left\langle P_{mac}^\dagger P_{mac} \right\rangle \quad (4.13)$$

We will show later, that this quantity shows nonlinear behavior, e.g., the spectra depend on the field amplitude of the external optical field. Therefore, the far field signal is not factorized

in the case of a strong external optical pump field. Besides, a factorization would only be valid in the case of low excitation, for negligible plasmon density $\langle a^\dagger a \rangle$ and conduction band density $a_{c_i}^\dagger a_{c_i}$. It is worth to mention that the far field spectra look the same with or without considering the dipole moment μ_i of the i -th quantum dot [TCRK13]. This is due to the fact that the plasmonic dipole moment is at least one order of magnitude larger than the excitonic one. Therefore, the Rayleigh spectra for the full polarization $P_{mic} = \chi a^\dagger + \sum_i \mu_i a_{c_i}^\dagger a_{v_i}$ are the same as for $P = \chi a^\dagger$, only considering the plasmonic polarization.

The second observable of interest is the second order correlation function

$$g^{(2)} = \frac{\langle P_{mac}^\dagger P_{mac}^\dagger P_{mac} P_{mac} \rangle}{\langle P_{mac}^\dagger P_{mac} \rangle^2} . \quad (4.14)$$

Similar to the far field spectra, the second order correlation function is given by the macroscopic polarization operator of the hybrid system. Nevertheless it turned out that the excitonic contribution does not influence the $g^{(2)}$ -function, since the excitonic dipole moment is very small compared to the plasmonic one [RGTK15]. Without the excitonic contribution the $g^{(2)}$ -function

$$g^{(2)} = \frac{\langle a^\dagger a^\dagger a a \rangle}{\langle a^\dagger a \rangle^2} \quad (4.15)$$

is defined as the ration of the plasmon correlation function $\langle a^\dagger a^\dagger a a \rangle$ divided by the square of the plasmon density $\langle a^\dagger a \rangle$. The second order correlation function is used to determine the emission statistics of the hybrid system. Therefore, the steady state $g^{(2)}(t_{stat})$ of the correlation function is calculated for different frequencies ω_{ext} of the external optical field. Furthermore, the two time correlation function

$$g^{(2)}(t, \tau) = \frac{\langle a^\dagger(t) a^\dagger(t + \tau) a(t + \tau) a(t) \rangle}{\langle a^\dagger a \rangle^2(t)} \quad (4.16)$$

for the plasmons will be investigated. Beside the informations about the emission statistics of the hybrid system for $\tau = 0$, this function additionally gives informations about the correlation time of the hybrid system for $\tau \neq 0$. We investigate the τ -dynamics in Section 4.4.2 for continuous wave excitation.

We assume that the constituents of the hybrid system are uncorrelated for $t = 0$. Therefore, we assume as initial conditions for the quantum dots the electron in the valence band. For the plasmons we use a thermal distribution for the plasmon probability [Fox06]

$$P_n = \langle |n\rangle \langle n| \rangle = \frac{1}{\bar{n} + 1} \left(\frac{\bar{n}}{\bar{n} + 1} \right)^n . \quad (4.17)$$

\bar{n} is the mean value of the thermal excitation and n the number of plasmons. The mean value for the plasmons excited thermally

$$\bar{n} = \frac{1}{e^{\frac{\hbar\omega_{sp}}{k_b T}} - 1} \quad (4.18)$$

is given by the Bose-Einstein distribution. Starting with these initial conditions the time dynamics of the observables are calculated. It is worth to mention that these initial conditions

only influence the results for the time dynamics. For the spectra the initial values of the system do not play a role since the results are calculated for the steady state of the system under continuous wave excitation. This steady state is independent of the initial conditions.

The quantum mechanical dynamics for the observables are calculated via an operator equation [SZ97]

$$\frac{d}{dt}\rho = \frac{i}{\hbar} [\rho, H] + \mathfrak{L}_{sp} + \mathfrak{L}_g \quad (4.19)$$

for the density matrix ρ of the system. The observables of interest like, e.g., the plasmon density correlation $\langle a^\dagger a^\dagger a a \rangle$ is calculated by tracing over the density matrix $\langle a^\dagger a^\dagger a a \rangle = \text{tr}(a^\dagger a^\dagger a a \rho)$. As simple example, we calculate the equation of motion for the plasmon density $\langle a^\dagger a \rangle$ by using the operator equation (4.19), the Lindblad terms (4.9) and the system Hamiltonian (4.2) - (4.8):

$$\frac{d}{dt} \langle a^\dagger a \rangle = -\gamma_{sp} \langle a^\dagger a \rangle - 2 \sum_i \mathfrak{Im} \left[g_i \langle a_{v_i}^\dagger a_{c_i} a^\dagger \rangle \right] - \frac{2}{\hbar} \chi \mathfrak{Im} \left[E_t \langle a^\dagger \rangle \right]. \quad (4.20)$$

The plasmon density is damped by γ_{sp} , coupled via g_i to the excitonic system and via the plasmonic dipole moment χ to the external optical field. The coupling via g_i to the excitonic system involves excitonic assisted plasmonic transition $\langle a_{v_i}^\dagger a_{c_i} a^\dagger \rangle$, to close the system of differential equation one could calculate the equation of motion for $\langle a_{v_i}^\dagger a_{c_i} a^\dagger \rangle$. This equation couples to higher terms which themselves couple to even higher terms and so on and so forth. So the coupling g_i between the excitonic two level system and the plasmonic system, which can in principle have an infinite number of excitations, introduce a so called hierarchy problem in the plasmonic states. This well known hierarchy problem can approximately be solved, e.g., by factorization schemes like the cluster expansion [KK06, KK08]. But it was shown that the cluster expansion can result in unphysical behavior for only a few quantum dots interacting with a bosonic mode [RCSK09]. Therefore we introduce number states $|n\rangle$ for the plasmons and truncate the hierarchy numerically by calculating up to the order where the values of the observables converge. The number states are eigenstates of the bosonic system, thus

$$H_{pl}|n\rangle = \hbar\omega_{sp}n|n\rangle \quad \text{and} \quad \sum_{n=0}^{\infty} |n\rangle\langle n| = 1 \quad (4.21)$$

holds. n represents the number of plasmons in the system. Since the eigenstates $|n\rangle$ form a complete set of eigenvectors, all observables can be expressed through the number states. As an example, we express the expectation value of the macroscopic polarization

$$\begin{aligned} P_{mac} &= \left(\chi \sum_{n=0}^{\infty} \langle a^\dagger |n\rangle\langle n| \rangle + \sum_i \mu_i \langle a_{c_i}^\dagger a_{c_i} |n\rangle\langle n| \rangle \right) + \text{h.a.} \\ &= \left(\chi \sum_{n=0}^{\infty} \sqrt{n+1} \langle |n\rangle\langle n| \rangle + \sum_i \mu_i \langle a_{c_i}^\dagger a_{c_i} |n\rangle\langle n| \rangle \right) + \text{h.a.} \end{aligned} \quad (4.22)$$

and of the second order correlation function

$$g^{(2)} = \frac{\sum_{n=0}^{\infty} \langle a^\dagger a^\dagger a a |n\rangle\langle n| \rangle}{\left(\sum_{n=0}^{\infty} \langle a^\dagger a |n\rangle\langle n| \rangle \right)^2} = \frac{\sum_{n=0}^{\infty} n(n-1) |n\rangle\langle n|}{\left(\sum_{n=0}^{\infty} n \langle |n\rangle\langle n| \rangle \right)^2} \quad (4.23)$$

through the number states. Especially for the macroscopic polarization, off-diagonal elements such as $|n\rangle\langle m|$ with $n \neq m$ are needed to calculate all observables of interest. We derive the equations of motion for the hybrid system in a biexcitonic basis for the two quantum dots

$$\rho_{opqr}^{n,m} = \left\langle a_{o_j}^\dagger a_{p_i}^\dagger a_{q_i} a_{r_j} |n\rangle\langle m| \right\rangle, \quad (4.24)$$

where i and j label the i -th and j -th quantum dot, respectively, and $o, p, q, r \in c, v$ label the conduction and valence band, respectively. Using the conservation of charges for the excitonic system ($n_v + n_c = 1$) a general plasmon probability

$$p_{n,m} = n_{v_1}^{n,m} + n_{c_1}^{n,m} = \rho_{vvvv}^{n,m} + \rho_{vccv}^{n,m} + \rho_{cvvc}^{n,m} + \rho_{cccc}^{n,m} \quad (4.25)$$

can be written in the biexcitonic basis. This general plasmon probability does not only include the probability to find n plasmons in the system (diagonal elements $n = m$) but additionally the probabilities for higher plasmon transitions (off-diagonal elements $n \neq m$). Now, we restrict the system to two quantum dots. With only two quantum dots the hierarchy of the excitonic system is closed at the level of four excitonic operators. As mentioned before, the hierarchy in the plasmonic system will be truncated numerically. Here, we only state the equation of motion for $\rho_{cccc}^{n,m}$:

$$\begin{aligned} \partial_t \rho_{cccc}^{n,m} = & (\dot{\mathfrak{i}}(n-m)\omega_{sp} - \frac{\gamma_{sp}}{2}(n+m) - 2\gamma_g)\rho_{cccc}^{n,m} + \gamma_{sp}\sqrt{n+1}\sqrt{m+1}\rho_{cccc}^{n+1,m+1} \\ & - \dot{\mathfrak{i}}\sqrt{n+1}\left(\frac{g_1}{\hbar}\rho_{cccv}^{m,n+1*} + \frac{g_2}{\hbar}\rho_{ccvc}^{m,n+1*}\right) + \dot{\mathfrak{i}}\sqrt{m+1}\left(\frac{g_1^*}{\hbar}\rho_{cccv}^{n,m+1} + \frac{g_2^*}{\hbar}\rho_{ccvc}^{n,m+1}\right) \\ & - \dot{\mathfrak{i}}\frac{\mu_1}{\hbar}(E_t^*\rho_{cccv}^{m,n*} - E_t\rho_{cccv}^{n,m}) - \dot{\mathfrak{i}}\frac{\mu_2}{\hbar}(E_t^*\rho_{ccvc}^{m,n*} - E_t\rho_{ccvc}^{n,m}) \\ & + \frac{\dot{\mathfrak{i}}}{\hbar}E_t^*\chi^*(\sqrt{m+1}\rho_{cccc}^{n,m+1} - \sqrt{n}\rho_{cccc}^{n-1,m}) + \frac{\dot{\mathfrak{i}}}{\hbar}E_t\chi(\sqrt{m}\rho_{cccc}^{n,m-1} - \sqrt{n+1}\rho_{cccc}^{n+1,m}), \end{aligned} \quad (4.26)$$

where the first line is the result of the free Hamiltonian (4.2) and Lindblad super-operators for spontaneous emission (4.9). The oscillation $\dot{\mathfrak{i}}(n-m)\omega_{sp}\rho_{cccc}^{n,m}$ originates from the free Hamiltonian of the plasmons. We have the decay of $\rho_{cccc}^{n,m}$ due to spontaneous emission of the plasmonic and excitonic systems, and the driving of $\rho_{cccc}^{n,m}$ by the higher state $\rho_{cccc}^{n+1,m+1}$. This process accounts for energy relaxation, since it provides a path for the energy to decay from a plasmonic state n, m into a plasmonic state n', m' with $n > n'$ and $m > m'$. The second line describes the interaction between the plasmons and excitons. $\rho_{cccc}^{n,m}$ couples to excitonic transition in either quantum dot 1 or 2 assisted by plasmonic transition $m, n+1$ or $m+1, n$. In the third line the plasmonic states n, m remain unchanged, since this line describe the interaction between the excitons and the external optical pump field. The last line occur due to the interaction between the plasmons and the external optical field. Therefore, the excitonic states in this line remain unchanged. The rest of the needed equations of motions are given in Appendix B. With these equations the hierarchy for the excitonic system is closed, considering one electron in each quantum dot. A sketch of the coupled equations of motion is given in Figure 4.2, where the red arrows indicate definitions and the black ones coupling of the dynamical quantities.

For the plasmonic system states up to the 4-th order are incorporated since for weak excitation ($\Omega = 10^{-5} eV$) $\rho_{opqr}^{5,5} \approx 0$ holds. Therefore, the hierarchy of the plasmonic system can

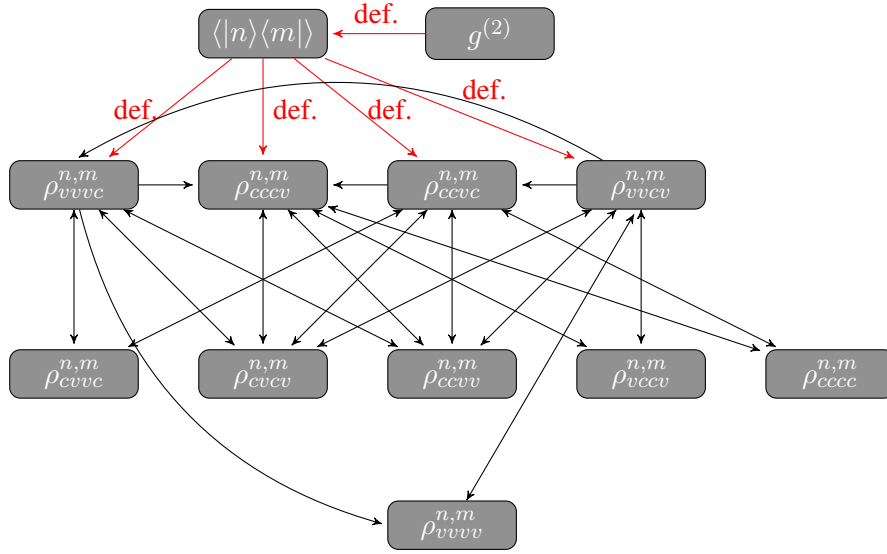


Figure 4.2 | Sketch of the equations of motion for two quantum dots coupled to a metal sphere and to each other by the Förster interaction. The quantum dots has one electron each. Red arrows accounts for definitions and the black ones for coupling of the dynamical quantities. Note, the hierarchy in the excitonic quantities is closed for the case of two quantum dots at this stage.

be truncated numerically and, in this case, higher order plasmonic correlations do not change the results. For a stronger external optical pump field, higher states need to be included for converging results of the observables of interest.

With the equations of motions (4.26), (B.2) - (B.10) for the hybrid system, the Lindblad terms including damping of the single systems (4.9) and the operator equation to calculate the dynamics (4.19) we are able to calculate the dynamics. In the next sections, we will discuss the temporal evolution of the coupled hybrid system, the Rayleigh spectra (4.13) and the second order correlation function. Especially, we will investigate their behavior on changes of the system parameters like the distance between the constituents and influence of the Förster interaction between the two quantum dots.

4.4 Temporal evolution of the coupled hybrid system for different excitations

To gain first insights into the dynamics and characteristics of the coupled hybrid system, we will start with the temporal evolution of the observables of interest. For a pulsed excitation the observable of interest is the polarization of the coupled hybrid system, which will be important when comparing theory and experiment in Chapter 5.

In the case of continues wave excitation, we will focus on the second order correlation function to investigate the emission statistics of the coupled hybrid system (see Section 4.4.2), since the second order correlation function of our system is not defined for pulsed excitation.

4.4.1 Temporal evolution of the system polarization after excitation with an Gaussian pulse

After setting up the theory in the last sections we now start to solve the equations of motions numerically for certain situations. Here, we start with the coupled hybrid system under pulsed excitation. As excitation pulse we used a Gaussian pulse resonantly to the excitons and plasmons. We found that the Förster interaction between the quantum dots do not play a role for the observables of interest here and therefore, we set it 0.

In Figure 4.3 we plot the Rayleigh signal of two quantum dots coupled resonantly to a metal sphere. The hybrid system is excited resonantly by a Gaussian pulse. By varying the distance between quantum dots and metal sphere, different behaviors occur. It is worth to mention that similar curves can be obtained for one quantum dot coupled to a metal sphere, hybrid systems with detuning between the constituents of the hybrid and for excitation with a delta pulse. If the system is excited by a delta pulse, one need to focus on the factorized Rayleigh signal in this particular case since density like terms are not driven by a delta pulse. Furthermore, the curves are shaped very similar if one compares the different parts in the Rayleigh signal (excitonic, mixed and plasmonic part).

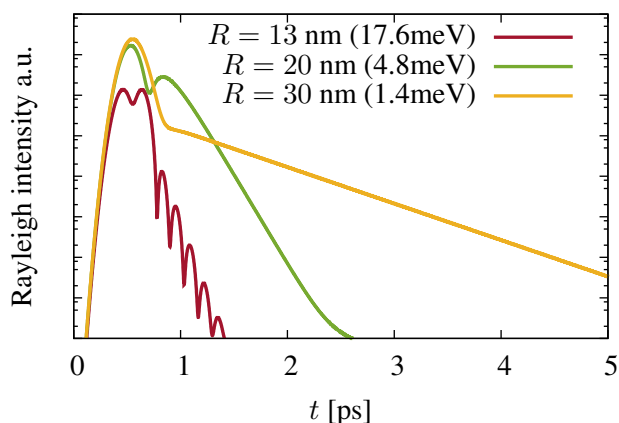


Figure 4.3 | Temporal evolution of the Rayleigh scattering of the hybrid system. The excitonic resonance of both quantum dots and the plasmon resonance are equal. The system is excited on resonance by a Gaussian pump pulse. Note, the y-axis is on a logarithmic scale.

One clear trend visible in Figure 4.3 is the decreased lifetime of the hybrid system for smaller inter particle distances. This is due to a stronger coupling and a resulting higher energy transfer from the excitonic system to the plasmonic one. In the plasmonic system the energy dissipates due to the large losses. Similar shaped curves have been investigated analytically for δ -pulse excitation and numerically for Gaussian pulse excitation in [MTK07]. The different shapes of the curves are related to the ratio of the damping to the coupling strength between excitons and plasmons. By changing the distance R , the coupling strength varies over one order of magnitude (compare legend of plot). The beatings in the strongly coupled case (c.p. red curve in Figure 4.3) are called quantum beats. These beats occur if a hybrid system is excited coherently by a short pulse and has also been found in [MST+95]. There, they referred to the different cases as under damped, critical and over damped case. In the under damped

case, the coupling is strong compared to the damping (red curve in Figure 4.3). In the critical case, the damping and the coupling strength are in the same range (green curve) and in the over damped case, the coupling is way weaker than the damping of the system (yellow curve).

This quantum beats does not only occur in hybrid system but can additionally occur generally in three level systems. They are apparent in V -type three level systems but not in Λ -type ones. A sketch of the level structure of V -type and Λ -type three level systems is given in Figure 4.4. In a V -type system two excited states 3 and 2 share the same ground state. Our hybrid system of a metal sphere and quantum dots is approximately a V -type three level system. Similar to the Fano effect discussed in Section 3.2, the quantum beats occur due to interference of different quantum mechanical paths. Therefore, they occur in V type three level systems and hybrid systems but not in Λ -type systems [SZ97, MST⁺95]. Considering a V -type three level system excited coherently, the decay of the excited states leads to the same ground state under the emission of a photon with energy E_{12} or E_{13} .

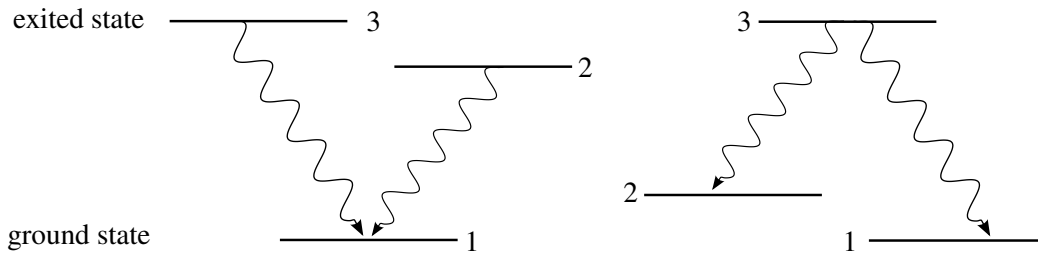


Figure 4.4 | Sketch of the energy levels of a V -type three level system (left) and for a Λ -type one (right).

Quantum beats in hybrid systems can be used for, e.g., coherent laser spectroscopy, the quantum beat spectroscopy [KFvP⁺92]. This technique is used to determine the energetic structure in atoms [DKW64] or more complex systems like molecules [LHZK87, LWK76, BFB⁺89] by measuring the frequency of the quantum beats of a certain transition. This can be used in time domain but also for spectroscopy techniques like, e.g., four-wave-mixing [AMO⁺97]. Furthermore, it is important to ensure, that the beats occur due to interference within a system and not due to interference of the far field signal of different systems at the detector. Since the linear spectra show no difference, one possibility is using four-wave-mixing and compare the third-order polarization between the coupled systems and the uncoupled one [KFvP⁺92]. The the third-order polarization maxima appear at different times depending where the quantum interference takes place. So it is possible to ambiguous distinguish between interference between quantum mechanically coupled systems and several systems where only the far field signal interfere at the detector [KFvP⁺92].

4.4.2 Second order correlation function of the hybrid system for optical continuous wave excitation

In this section we investigate the hybrid system under continuous wave excitation. We focus on the second order correlation function of the plasmons (4.15) since this observable describes the emission statistics of the system. A value smaller than 1 for the second order correlation function indicates a single photon like source, a purely non-classical emission. Coherent emission takes place for a value of 1, which is emitted, e.g., from laser like sources. All values above

one indicate a bunched emission of the hybrid system. Thermal emission is characterized by a value of 2, but higher bunchings will occur in our hybrid system as we will discuss later. The possible statistics are sketch in Figure 4.5. The external optical pump field is weak to avoid any saturation of the excitonic transition [RDSF⁺10], since this would decrease the effects induced by the coupling between the constituents.

In Figure 4.6 we plot the temporal evolution of the plasmonic second order correlation function (4.15) for continuous wave excitation. Note, the $g^{(2)}$ -function is not meaningful for pulsed excitation. Plotted are two different distances between the quantum dots and the metal sphere ($R = 10$ nm and $R = 16$ nm), as well as with and with-

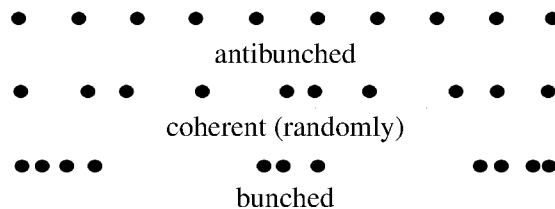


Figure 4.5 | Possible emission statistics.

out Förster interaction between the two quantum dots. The diameter of the silver sphere is 10 nm for each plot. The second order correlation function oscillates in the beginning but reaches a steady state after ≈ 1 ps. The steady marks an equilibrium between the energy pumped into the hybrid system by the external field and the energy dissipated by the system due to losses in the excitonic and the plasmonic system. The strength and frequency of the oscillations is determined by the coupling strength between the quantum dots and the silver sphere. It is clearly visible in Figure 4.6 that the second order correlation functions for a distance of $R = 10$ nm exhibit way stronger and faster oscillations than the one with a distance of $R = 16$ nm. This is due to the fact that $R = 10$ nm gives a coupling strength of $g = 38.8$ meV and $R = 16$ nm leads only to a coupling strength of $g = 9.5$ meV. For the strongly coupled case ($R = 10$ nm) the emission of the hybrid system is bunched [PGC⁺13]. For a weaker coupling ($R = 16$ nm) the emission statistic is antibunched without Förster interaction between the quantum dots, but slightly bunched with Förster interaction. Furthermore, we see the influence of the Förster interaction between the quantum dots on the second order correlation function. The Förster interaction not only changes the temporal development, but additionally the steady state value of the $g^{(2)}$ -function. This will be important for Section 4.7, where we take a closer look at the spectral dependency of the second order correlation function. To obtain the spectra, we calculate several temporal evolutions of the emission statistics of the hybrid to the steady state using different excitation frequencies of the external optical field.

Beside the case excited resonantly (Figure 4.6), we additionally plot the case for slightly off-resonantly excitation. In Figure 4.7 the excitation frequency of the external optical field is 3 meV above the resonance energies of the quantum dots and the plasmonic resonance. The sphere diameter is 10 nm and the external optical field is weak in intensity. Again, after some oscillations the system reaches a steady state. Due to the off-resonant excitation the oscillation are not that strong as in the resonantly pumped case. Interestingly, the steady state changes: For a distance of $R = 10$ nm, the steady state of the second order correlation function increase. For 16 nm distance the same trend occurs, but the increase is not that strong. We will focus on this in more detail in the spectra of the second order correlation function in Section 4.7 and explain why the emission statistics are extremely sensitive to the frequency of the external optical field.

For systems with off-resonantly coupled quantum dots and plasmons, like in the case of the Rayleigh spectra in Figure 4.11. The same trends are visible but weaker. Therefore, these cases are not shown here.

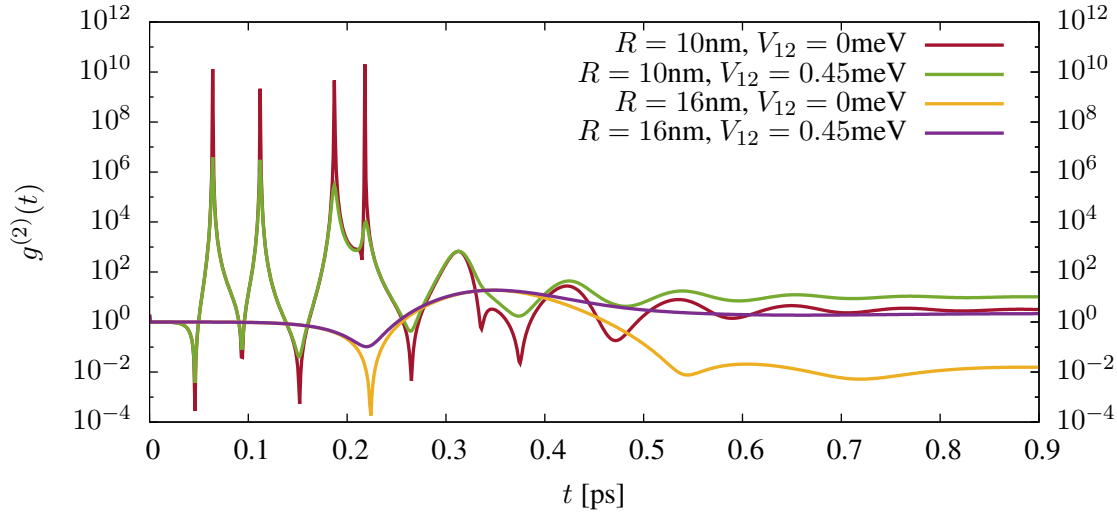


Figure 4.6 | Second order correlation function for resonantly coupled hybrid systems on logarithmic scale. The hybrid system is driven by weak continuous wave excitation. The diameter of the silver sphere is 10nm and we plot two different distances between the constituents ($R = 10\text{nm}$ and $R = 16\text{nm}$) with and without Förster interaction between the quantum dots.

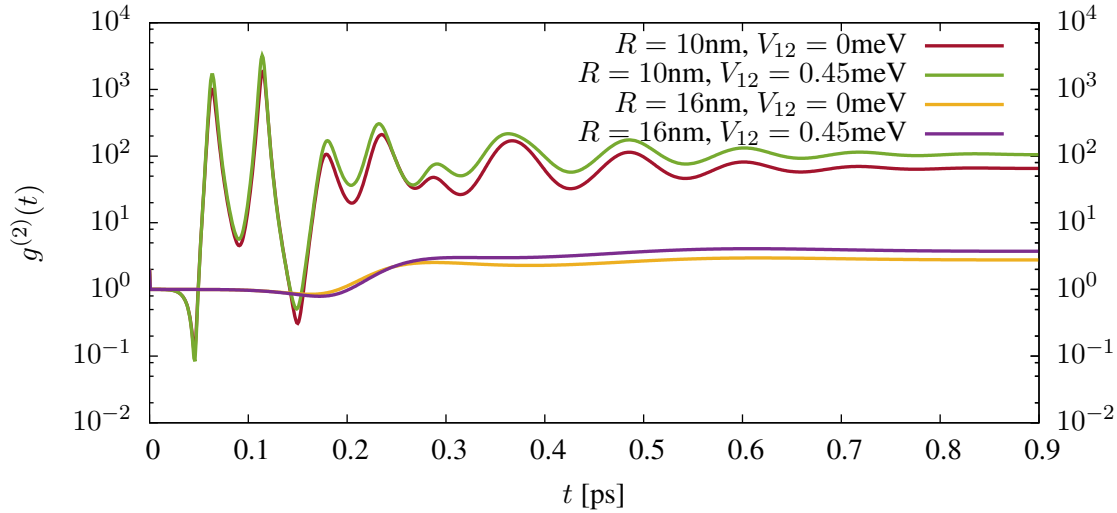


Figure 4.7 | Second order correlation function for resonantly coupled hybrid systems on logarithmic scale excited slightly off-resonant. The hybrid system is driven by weak continuous wave excitation. The diameter of the silver sphere is 10nm and we plot two different distances between the constituents ($R = 10\text{nm}$ and $R = 16\text{nm}$) with and without Förster interaction between the quantum dots.

So far we plotted the dynamics of the second order correlation function in time t (4.15). In Figure 4.8 we plot the $g^{(2)}$ -function in τ (4.16) for the resonantly coupled and pumped case. To calculate the τ -dynamics, we calculate the steady state in t and use this steady state as initial

condition for the τ -dynamics. This procedure follows from the quantum regression theorem [SZ97, Car93]. Additionally, one needs to shift the number state n to $n + 1$ and take the factor $\sqrt{n + 1}$ into account.

Figure 4.8 shows the dynamic of the hybrid system in τ . All curves reach 1 for $\tau \rightarrow \infty$, since the correlation between two plasmons vanishes and 1 is the value for coherent/uncorrelated emission.

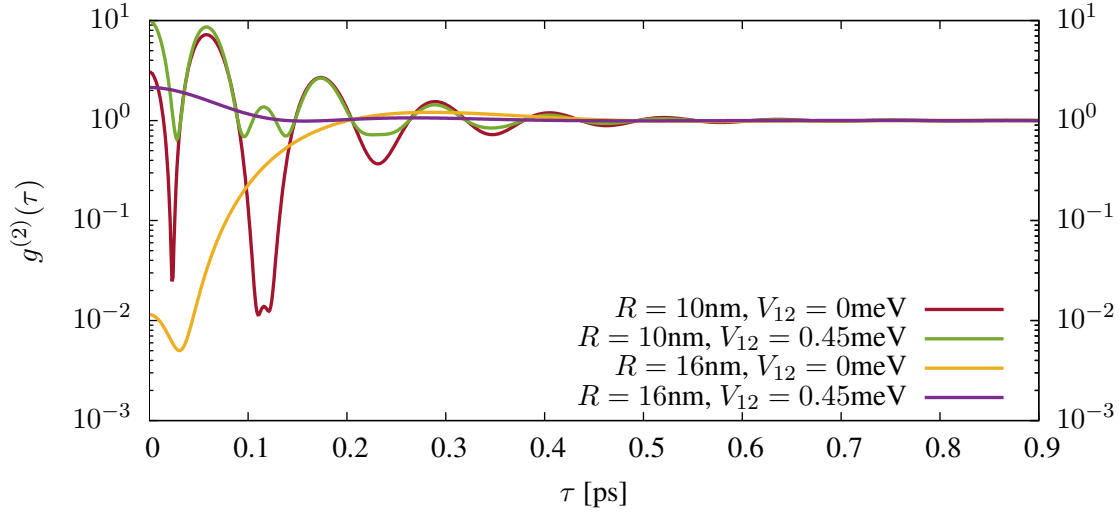


Figure 4.8 | τ -dynamics of the second order correlation function. The hybrid system is excited resonantly by the external optical field.

4.5 Optical emission spectra of the hybrid system

To characterize the hybrid system consisting of two quantum dots and a silver sphere in more detail we calculate the optical emission spectra and vary several system parameters.

It will become apparent in the optical spectra that, due to the interaction between the quantum dots and the metal sphere, new eigenstates are formed in the system. This hybridization of system states is investigated by changing the distance between the quantum dots and the metal sphere, directly changing the coupling strength, changing the Förster interaction between the quantum dots and changing the detuning between the constituents of the system.

Furthermore, the influence of the intensity of the external optical field on the emission spectra is under investigation. Since the emission spectra can be calculated for the weak as well as for strong external optical pumping without factorizations, it shows nonlinear behavior, e.g., scaling with the external optical pump intensity. For higher optical pumping the interaction between the plasmons and the excitons decrease due to saturation of the excitonic transition [RDSF⁺10].

First, we calculate the Rayleigh spectra in the limit of weak excitation ($\Omega = 1 \cdot 10^{-5}$ eV), since in this limit the impact of the coupling on the Rayleigh spectra is the strongest. In the weak field limit, the unfactorized Rayleigh spectra (4.13)

$$I_{far}(\omega_{ext}) = \langle P_{mac}^\dagger P_{mac} \rangle(\omega_{ext}) \quad (4.27)$$

and a factorized Rayleigh spectra

$$I_{far}(\omega_{ext}) \approx \langle P_{mac}^\dagger \rangle(\omega_{ext}) \langle P_{mac} \rangle(\omega_{ext}) = |\langle P_{mac} \rangle(\omega_{ext})|^2 \quad (4.28)$$

yield the same results. This is due to the fact that the excitation by the external optical field is too weak to excite plasmon densities $a^\dagger a \approx 0$ or excitonic densities $a_{c_i}^\dagger a_{c_i} \approx 0$.

4.5.1 Rayleigh spectra of the uncoupled constituents of the hybrid system

We start with the single constituents of the hybrid without coupling between them. We only investigate the Förster interaction between the quantum dots but no interactions between the plasmonic and excitonic system. The spectra in Figure 4.9 are plotted versus the detuning of the transition energies and the optical external field ($\Delta\omega_{ext} = \omega_{ext} - \omega_{g_{1/2}} = \omega_{ext} - \omega_{sp}$).

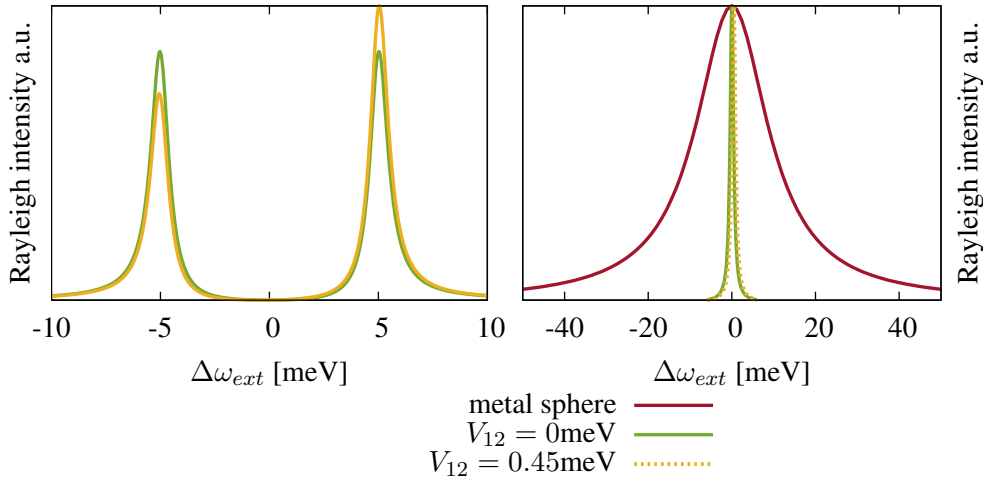


Figure 4.9 | Rayleigh picture of the uncoupled constituents of the hybrid system versus the detuning to the external optical field. **Left:** Two quantum dots with identical parameter but different excitonic transition energies. The detuning is 2 meV. Shown are the spectra with ($V_{12} = 0.45\text{meV}$) and without ($V_{12} = 0\text{meV}$) the Förster interaction between the two quantum dots. **Right:** Bare metal sphere with its broad resonance and two identical quantum dots with and without the Förster interaction between them.

As long as not stated otherwise the dipole moment of the excitons is set to $\mu_i = 1.84\text{nm}$ [EB97], and the Förster interaction between the quantum dots does not exceed $V_{12} = 0.45\text{meV}$ valid for, e.g., CdSe quantum dots [LRNB03, CHTK02]. The damping rate of the excitons is set to $\gamma_{g_i} = 1\text{meV}$.

On the left side of Figure 4.9 the Rayleigh spectra of two identical quantum dots are shown with a detuning of $\Delta = \hbar(\omega_{g_1} - \omega_{g_2}) = 2\text{meV}$, all other parameters are equal. Including the Förster interaction between the quantum dots, their dipole moments are redistributed, indicated by the changes in the height of the peaks, and their resonances are slightly shifted. Due to the Förster coupling between the two quantum dots, the lower resonance is shifted to lower energies

and the energetic higher resonance to higher energies. The Förster induced energy shift and the change in the dipole moments can be evaluated by setting up the system matrix

$$\underline{S} = \begin{pmatrix} -\Delta/2 & V_{12} \\ V_{21} & \Delta/2 \end{pmatrix} \quad (4.29)$$

and calculate the corresponding eigenvalues. These eigenvalues of the system matrix are the new eigenenergies of the two coupled quantum dots. Due to the interaction a hybridization takes place and the new eigenenergies of the coupled system are shifted:

$$E_{new} = \pm \frac{1}{2} \sqrt{4V_{12}^2 + \Delta^2} \quad (4.30)$$

with the detuning between the quantum dots $\Delta = \hbar(\omega_{g1} - \omega_{g2})$. This result is similar to the one given in [DAFK06]. Obviously, the energy needed to create an exciton changes due to the Förster interaction between the quantum dots.

The optical dipole moments of the possible transitions in the coupled quantum dot - quantum dot system are calculated by using the eigenvalues and eigenvectors of the system matrix \underline{S} to

$$\mu_{new} = \mu - \frac{\mu \left(\Delta \pm \sqrt{4V_{12}^2 + \Delta^2} \right)}{2V_{12}}. \quad (4.31)$$

The Rayleigh spectra for the case of two identical quantum dots is shown in Figure 4.9 on the right. In this case the Förster interaction shifts the new energy to higher energies. In fact there is also a new state at lower energies but this one is a so called dark state, which are not optically excitable. For identical quantum dots the new energies due to hybridization of the states simplify to $\hbar\omega_g \pm V_{12}$, cp. (4.30). For two identical quantum dots ($\Delta = 0\text{meV}$) coupled via the Förster interaction, the dipole moments (4.31) simplify to 0nm , corresponding to the dark state, and 2μ , the optical excitable state and usually named bright state.

Beside the spectra of the quantum dots we show the spectra of the silver sphere (Figure 4.9, right). We assume $\varepsilon_{out} = 5$ for the medium surrounding the meta sphere. This yields according to Section 2.1.2 a resonance energy $\hbar\omega_{sp} = 2.43\text{eV}$ and a corresponding damping rate $\gamma_{sp} = 210\text{meV}$ for a silver sphere with a radius of 5nm . The dipole moment of the silver sphere under these conditions is $\chi = 24.1\text{nm}$. Due to high losses in the silver, the plasmonic spectrum is way broader than the excitonic one (cp. Figure 4.9 right). Quite small spheres and a quantum dot at a distance twice the radius of the silver sphere ensure the validity of the dipole approximation [VVKH12] and yield the strongest interaction between the constituents of the system. As long as not stated otherwise, we will use the plasmonic parameter as mentioned above.

4.5.2 Rayleigh spectra of the resonantly coupled hybrid system

Now, we investigate the Rayleigh spectra of the silver sphere coupled to the quantum dots. Furthermore, we investigate the influence of the Förster interaction between the two quantum dots and the influence of the coupling between the quantum dots and the silver sphere (g) on the spectra.

In Figure 4.10 the Rayleigh spectra of the coupled hybrid system are shown versus the detuning of the plasmonic resonance frequency (ω_{pl}) and the external optical field

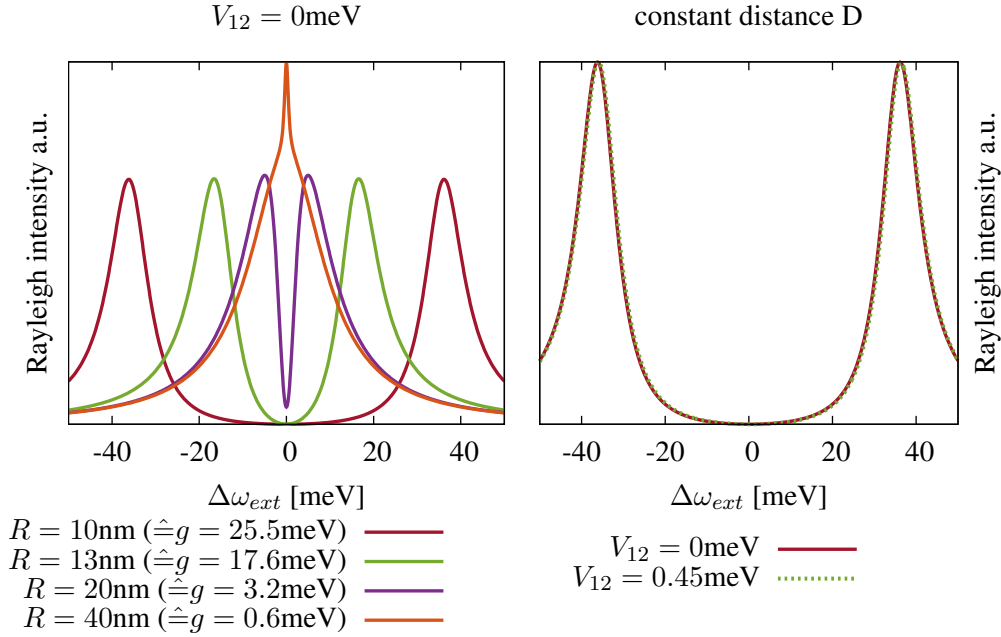


Figure 4.10 | Rayleigh spectra for two quantum dots resonantly coupled to the silver sphere versus the detuning to the external optical pump field. **Left:** Spectra for a silver sphere of $r_m = 5\text{nm}$ radius and several distances between the quantum dots and the silver sphere. **Right:** Rayleigh spectra for a 5nm silver sphere and a distance of 10nm between the quantum dots and the silver sphere with and without the Förster interaction between the quantum dots.

$\Delta\omega_{ext} = \omega_{ext} - \omega_{pl}$. Here, the excitons and the plasmons are resonantly coupled. On the left side of Figure 4.10 the spectra of the coupled hybrid system is shown for different distances between the constituents. A larger distance D decreases the coupling between plasmons and excitons. Similar to the Förster coupling, discussed earlier, the interaction between the plasmonic and excitonic system results in new eigenenergies of the system. These newly formed eigenstates are observed as single peaks in the Rayleigh spectra for quantum dots and silver sphere near to each other. With increasing coupling strength between the plasmons and excitons the peaks move further apart. In the case of quite weak coupling ($R = 30\text{nm}$ corresponding to $g = 0.9\text{meV}$) the single spectra of the constituents of the hybrid system simply add up. We can calculate the the new eigenenergies of the coupled system by calculating the eigenvalues of the system matrix

$$\underline{\underline{S}} = \begin{pmatrix} E & V_{12} & g \\ V_{21} & E & g \\ g & g & E \end{pmatrix}, \quad (4.32)$$

with the interaction between the excitons and plasmons g and for the same resonance frequency ($E_{g_{1/2}} = E_{sp} = E$) for all constituents of the hybrid. This yields for the eigenenergies of the coupled hybrid system

$$E - V_{12} \quad \text{and} \quad \frac{1}{2} \left(2E + V_{12} \pm \sqrt{8g^2 + V_{12}^2} \right) . \quad (4.33)$$

The new resonances of the coupled hybrid system depend on the strength of the interactions. Usually the Förster interaction between the quantum dots (0.45meV) is at least one order of magnitude smaller than the interaction between plasmons and excitons, we can neglect the influence of the Förster interaction on the new eigenenergies. Also easy to see in the Rayleigh spectra for two quantum dots coupled to the plasmonic system with and without Förster interaction between the two quantum dots (Figure 4.10, right). In this case the Rayleigh spectra exhibits almost no changes due to variation of the Förster interaction between the excitons. Therefore, the eigenenergies simplifies to:

$$E \quad \text{and} \quad E \pm \sqrt{2}g , \quad (4.34)$$

which are valid for the Rayleigh spectra shown in 4.10 on the left. It is worth to mention that the energy splitting in the case of two quantum dots coupled to a silver sphere is different by a factor of $\sqrt{2}$ with respect to the energy splitting in a system of one quantum dot coupled to silver sphere, where the energy splitting in the coupled system is given by $E \pm g$ [RDSF+10]. Therefore, the splitting in Figure 4.10 is not the same as the coupling strength between the constituents, but rather $\sqrt{2}g$. The two visible peaks in the spectra already indicate that one of the new formed energies has a vanishing optical dipole moment. Without the Förster interaction between the two quantum dots, the dipole moments of the coupled system are 0 and $\chi/\sqrt{2} \pm \mu$. So their is no optical excitable transition for the resonance energy E . Therefore, only two peaks are visible in the Rayleigh spectra. Calculating the dipole moments including the Förster interaction between the quantum dots is straight forward but, due to the length of the formulas, not given here. Nevertheless, it is worth to mention that even the Förster interaction between the quantum dots does not allow the optical transition at energy E , the optical dipole moment is still vanishing.

To gain a deeper insight into the interactions within the hybrid system, we adapt a theory original developed by Ugo Fano for the interference of a discrete autoionized state and a continuum [Fan35]. This interaction between a discrete two level system and a continuum of states give rise of the Fano effect [Fan61]. Ugo Fano originally described the Fano effect mathematically for inelastic scattering of electrons in a Helium gas [Fan61]. Later, the Fano effect has been found in several systems were a discrete level system interacts with a continuum of states. Examples can be found in several nanostructures [MFK10]. The Fano effect appears if two optical path ways compete with each other. This quantum interference between the two possible paths, ground state to discrete state and ground state to continuum state, give rise of the Fano effect. Beside Fano's theory for the weak field limit, there are also extensions to the nonlinear regime were the excitonic and photonic states hybridize and the Fano effect strongly depend on the field intensity [KGR+08, RDSF+10]. We investigate the nonlinear regime in Section 4.6

Here, in the regime of linear optics, the Fano effect does not depend on the strength of the external optical field. According to the energy splitting in the coupled system of two quantum

dots and a silver sphere (4.34) three energies occur due to the hybridization of the excitonic and plasmonic states. With respect to the corresponding dipole moments (0nm and $\chi/\sqrt{2} \pm \mu$) it turns out that the state at E has no dipole moment, thus it is not optical excitable. Since only two optical path ways can interfere with each other (at the energies $E \pm \sqrt{2}g$). In between both new resonances the interference of both path ways is destructive and causes the dip in the spectra, which drops for certain interaction strength between the quantum dots and the silver sphere to zero. This phenomenon is also known as induced transparency, due to the absence of absorption for a certain frequency. This transparency has been achieved in several systems, e.g., two detuned electrical dipoles [BEP⁺11] or via plasmon induced transparency [LMH⁺11, ZLL⁺13, ZGW⁺08].

Comparing the results for the strongest coupling ($R = 10\text{nm}$) and the weakest ($R = 30\text{nm}$) in Figure 4.10, show how huge the change is. While the absorption is very high for the very weakly coupled case ($R = 30\text{nm}$), the system is transparent in the strongly coupled case ($R = 10\text{nm}$) at zero detuning $\Delta\omega_{ext} = 0$ meV. In the next section we will show that this induced transparency can be tuned by changing the detuning between the excitonic system and the plasmonic one.

4.5.3 Rayleigh spectra of the off-resonantly coupled hybrid system

After we investigated the Rayleigh spectra for resonantly coupled hybrid systems in the last section, we now take a closer look at off-resonantly coupled hybrids. Again, we explore the influence of the coupling strength between the excitonic and plasmonic system on the Rayleigh spectra. Furthermore, we show that the influence of the Förster interaction between the two quantum dots does not affect the shape of the Rayleigh spectra.

In Figure 4.11 on the right the Rayleigh spectra for a silver sphere with a diameter of 5 nm coupled to two quantum dots are shown. The distance between the quantum dots and the silver sphere is 10 nm which corresponds to a coupling strength of 25.5 meV. Due to the coupling between the excitonic system and the plasmonic system new energy eigenstates are formed, indicated by the two peaks in the spectrum. As in the resonantly coupled case in the last section, the Förster interaction between the quantum dots does not affect the Rayleigh spectra. Therefore we will restrict our calculations concerning the new eigenenergies of the system and the corresponding dipole moments to the case without Förster interaction. In the equations for the new eigenenergies and the new dipole moments it represents the limit $V_{12} \rightarrow 0$.

In Figure 4.11 on left we plot the Rayleigh spectra of a system of two quantum dots coupled to a silver sphere for various distances between the constituents. The detuning between the excitonic transition and the plasmonic one is 20 meV. The occurring interference at the energy of the excitonic transition (20 meV) exhibits an asymmetrical line shape. For energy slightly smaller than the excitonic transition, the Rayleigh intensity decreases (induced transparency). For energies slightly above the excitonic transition, the Rayleigh intensity is enhanced. Decreasing the distance between the constituents increases this effect since the coupling strength between the constituents of the hybrid is stronger. For small distances between the quantum dots and the silver sphere (10 nm) the splitting between the new eigenenergies of the system is so strong that no asymmetry is recognizable any more.

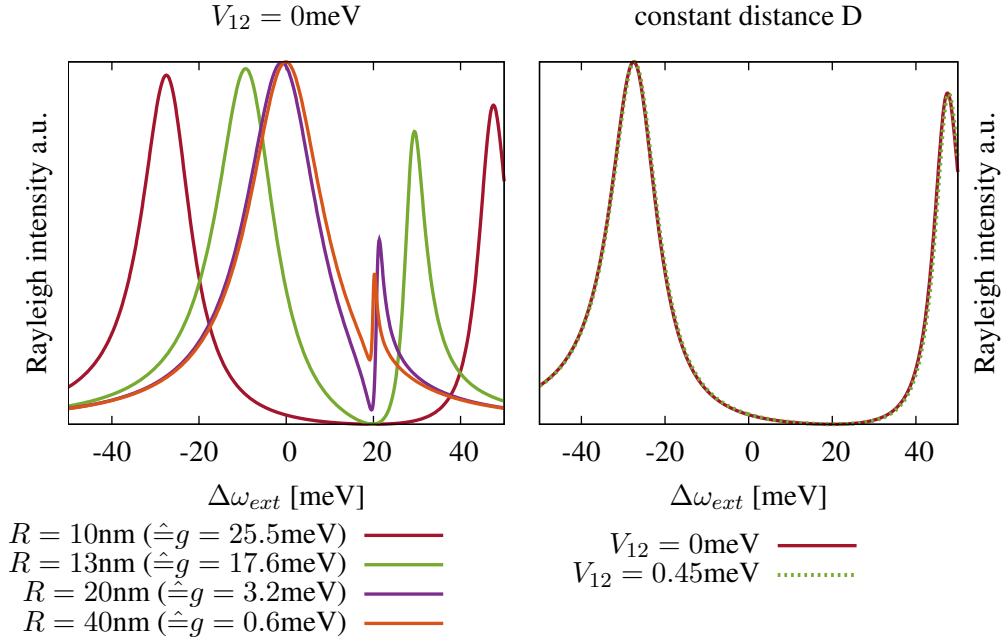


Figure 4.11 | Rayleigh spectra for two quantum dots coupled to the silver sphere versus the detuning of the surface plasmon frequency to the external optical pump field ($\Delta\omega_{ext} = \omega_{ext} - \omega_{pl}$). **Left:** Spectra for a silver sphere of $r_m = 5$ nm radius and several distances between the quantum dots and the silver sphere. **Right:** Rayleigh spectra for a 5 nm silver sphere and a distance of 10 nm between the quantum dots and the silver sphere with and without the Förster interaction between the quantum dots.

The system matrix of the coupled hybrid without the Förster interaction

$$\underline{S} = \begin{pmatrix} E_g & 0 & g \\ 0 & E_g & g \\ g & g & E_{sp} \end{pmatrix} \quad (4.35)$$

now includes the excitonic transition E_g and the plasmonic one E_{sp} . The new eigenenergies of the coupled system are E_g and

$$\frac{1}{2} \left(E_g + E_{sp} \pm \sqrt{E_g^2 - 2E_g E_{sp} + E_{sp}^2 + 8g^2} \right) . \quad (4.36)$$

The corresponding dipole moments show that the transition at E_g is optically not excitable, even the Förster interaction between the quantum dots does not allow this transition. The remaining transition dipole moments are

$$\chi \pm \frac{4g\mu}{E_g - E_{sp} + \sqrt{E_g^2 - 2E_g E_{sp} + E_{sp}^2 + 8g^2}}, \quad (4.37)$$

which are now, in contrast to the dipole moments for the case off a resonantly coupled hybrid, depending on the resonance energies of the single constituents.

The asymmetric line shape at the energy of the excitonic transition in Figure 4.11 on the left is often called Fano resonance [Fan35, Fan61, RDSF⁺10]. It occurs due to quantum interference of two competing optical path ways. One optical excitable path connects the ground state with a discrete state and the other path the ground state with a continuum state. Both, the continuum state and the discrete state, need to be in the same energy regime. Due to the coupling between the constituents of the hybrid system an excitation from the ground state to an excited state can debouch one of both possible paths. This results in destructive interference of both paths in the energetic regime between the resonance energies of the quantum dots and the silver sphere. On the other hand, constructive interference occurs above the excitonic transition energy. Furthermore, the maxima of the Fano resonance shifts to higher energies for increasing coupling strength (cp. Figure 4.11). This shift is typical for the Fano effect in quantum dot and silver hybrid systems and was also found, e.g., in [ZGW⁺08].

In conclusion, we show that the Förster interaction does not change the shape of the Rayleigh spectra. All interesting interference effects are due to the interaction between the plasmonic and excitonic system. In general the effects increase with decreasing distance (higher coupling strength) between the constituents of the hybrid system.

4.6 Rayleigh spectra for different pump intensities of the external optical field

In the last section we discussed the Rayleigh spectra for the weak field limit. Now we investigate the influence of the pump intensity of the external optical field on the Rayleigh spectra. This pump dependent effect is sometimes called the nonlinear Fano effect [ZGW⁺08, KGR⁺08, ZG11]. It is worth to mention that the high pump intensity decreases the numerical stability. Therefore, higher order number states need to be taken into account to ensure numerical convergence.

In Figure 4.12 we show the Rayleigh spectra of two quantum dots coupled to a silver sphere (peak normalized). On the left all constituents are coupled resonantly and on the right the detuning is 20 meV between the quantum dots and the silver sphere. As already discussed the Förster interaction between the quantum dots does not change the spectra significantly. Similar to the previous section, we observe a Fano resonance in the Rayleigh spectra at the resonance frequency of the quantum dots ($\Delta_{\omega_{ext}} = 0$ meV and $\Delta_{\omega_{ext}} = 20$ meV). In the resonantly coupled case as well as in the off-resonantly coupled case the Fano resonance vanishes for higher intensities of the external optical field and the shape approaches the one of the bare silver sphere. This reduction is due to saturation of the excitonic transition [RDSF⁺10]. For high pump intensities of the external optical field, the transition starts to saturate since the electron is most likely in the conduction band. Therefore, the electron is incapable of interacting with the plasmonic system any more. This is due to the fact that the interaction between the excitonic system and the plasmonic one is driven by coherent quantities like, e.g., polarizations. Or in other words, the incoherent quantities grow faster for increasing pump intensities than the coherent quantities. This causes the reduction of the dip in the spectra. For weak intensities of the external pump field, coherent quantities dominate the system and the Fano effect arises in the spectra.

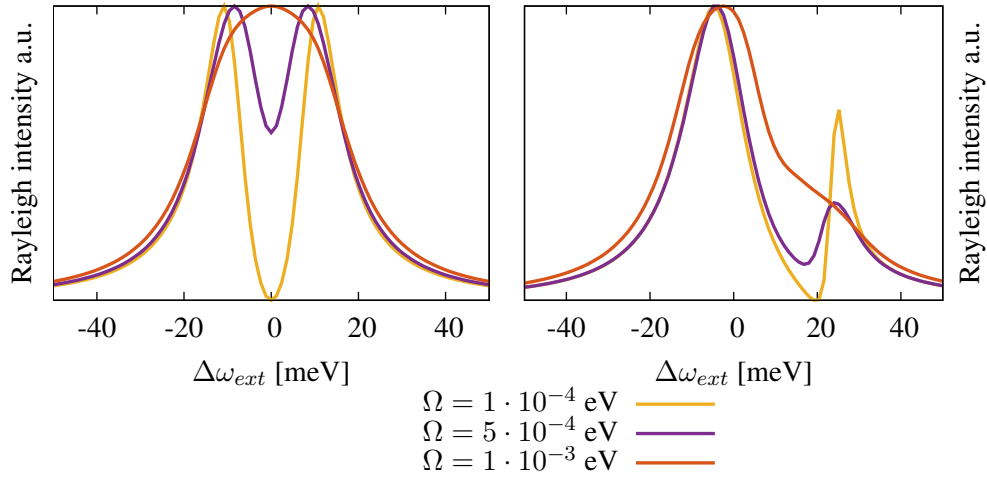


Figure 4.12 | Rayleigh spectra of a resonantly (left) and off-resonantly coupled hybrid system for different pump intensities of the external optical field. Shown is the Rayleigh spectra for a distance of 15nm ($g = 11.5\text{meV}$) between the two quantum dots and the silver sphere ($r_m = 5\text{nm}$). There is no Förster interaction between the quantum dots.

4.7 Second order correlation function of the hybrid system in frequency domain

In the last section it became obvious that the Förster interaction between the quantum dots barely change the emission spectra. Only very small shifts in the order of the Förster interaction strength has been observed. In this section the second order correlation function $g^{(2)}$ of the plasmons

$$g^{(2)} = \frac{\langle a^\dagger a^\dagger a a \rangle}{\langle a^\dagger a \rangle^2} \quad (4.38)$$

is under investigation. It turns out that the Förster interaction has a quite huge impact on the emission statistics of the hybrid system. Furthermore, the Förster interaction is capable of tuning the emission statistics. We found a strong increase of bunching for a certain excitation energy of the external optical field. However, also increased anti-bunching for a slightly detuned external optical field. For certain parameters of the hybrid system it is also possible to tune the emission statistics qualitatively from bunching, to a coherent and in the end to a bunched statistic by changing the Förster interaction from 0 meV up to 0.45 meV [TCRK13]. We calculate the $g^{(2)}$ -function similar to the Rayleigh spectra. The hybrid system is continuously pumped by the external optical field and calculated in time domain until the observables of interest reached a steady state. This is repeated for several excitation frequencies of the external optical pump field to obtain the spectra of interest. In order to get the largest changes in the spectra of the second order correlation function, the external optical pump field is weak ($\Omega = 1 \cdot 10^{-5} \text{ eV}$). For weak excitation we avoid saturation effects of the excitonic transition as we discussed already in 4.6. These saturation effects would weaken the influence of the Förster interaction between the two quantum dots on the spectra of the second order correlation func-

tion. In the following we will restrict our discussion to case of a resonantly coupled hybrid system ($\omega_{sp} = \omega_{g_{1/2}}$). In principal, similar effects are observed for a detuned hybrid system, but less pronounced. It is worth to mention that our explanation is valid for the resonantly coupled case and for the off-resonantly coupled case, too.

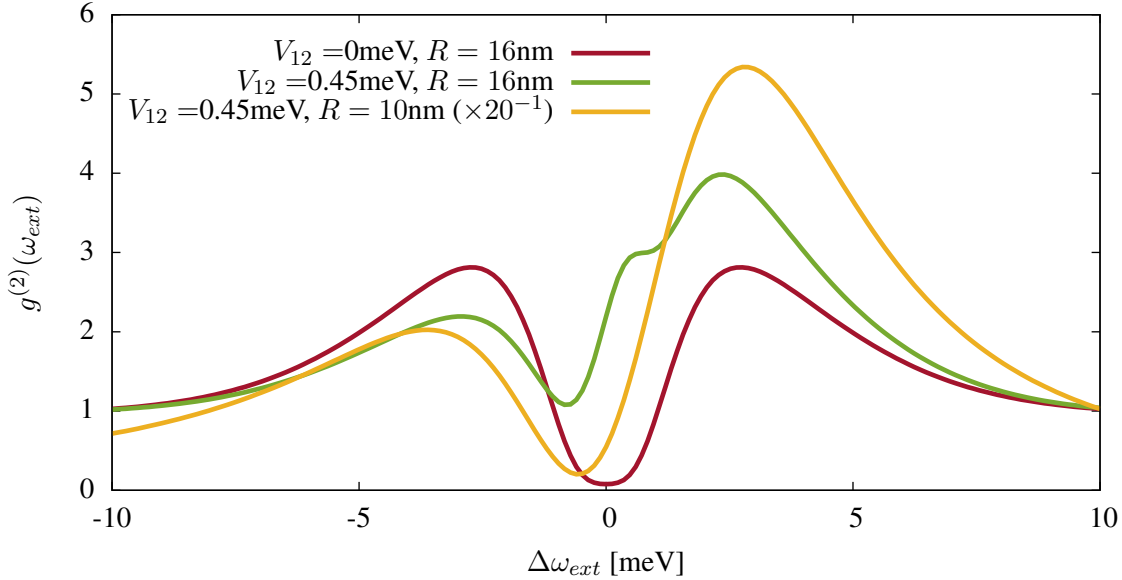


Figure 4.13 | Second order correlation function ($g^{(2)}(\omega_{ext})$) versus detuning of the plasmon frequency to the external pump field ($\Delta\omega_{ext} = \omega_{ext} - \omega_{sp}$). The results are for different distances R and strengths of the Förster interaction between the quantum dots V_{12} . The distance 10 nm between the quantum dots and the silver sphere corresponds to a coupling strength $g = 38.8$ meV, 16 nm corresponds to $g = 9.5$ meV.

In Figure 4.13 we plot the second order correlation function for two quantum dots coupled resonantly to a silver sphere. We observe a symmetrical line-shape of the $g^{(2)}$ -function without Förster interaction between the quantum dots (red curve in Figure 4.13). For resonant excitation the statistic shows antibunching ($\Delta\omega_{ext} = 0$ meV). For a detuning of ≈ 3 meV with respect to the external optical field the $g^{(2)}$ -function shows strong bunching and emits like a single photon source. For a large detuning between the resonances of the system and the external optical field the second order correlation function reaches 1, the coherent case. Far away from the resonances, the resonances do not play a role anymore and the statistic is the same as the one of the external optical pump field (coherent).

Including the Förster interaction between the quantum dots, the shape of the second order function changes drastically. First of all, we note that the shape becomes asymmetric. Later, we will show that this is related to redistributions of the transition dipole moments and the newly formed energies in the coupled hybrid system induced by the Förster interaction between the quantum dots. For a distance of $R = 10$ nm ($g = 38.8$ meV, yellow curve in Figure 4.13) the $g^{(2)}$ -function shows very huge bunching (≈ 110) for a detuning of +3 meV. At a detuning of -3 meV the bunching is a bit lower, approximately around 20. Note, the yellow curve is divided by 20 and does not show antibunching. Comparing to the case without Förster interaction between

the quantum dots, bunching is greatly enhanced for a detuning of +3 meV. We will stress this fact later in more detail in Plot 4.19 and 4.20, where we plot the second order correlation function versus the Förster interaction between the two quantum dots.

In the second case with Förster interaction between the quantum dots (green curve in Figure 4.13) the distance between the quantum dots and the silver sphere is 16 nm ($g = 9.5\text{meV}$). The raise of bunching is seen at a detuning of $\approx +3$ meV compared to the case without Förster interaction (red curve in Figure 4.13). This can be seen in more detail in Figure 4.19 and 4.20.

To gain a deeper insight into the system and the reasons for the certain line-shapes of the second order correlation function, we need to discuss how the function is calculated. The $g^{(2)}$ -function is given by the density correlation function divided by the square of the plasmon density (4.39). Therefore, we take a closer look at these observables in Figure 4.14:

For the case with a distance of $R = 15$ nm and without Förster interaction between the two quantum dots, we observe symmetrical line-shapes as it is the case for the second order correlation function (cp. Figure 4.13). The dip of the plasmon density correlation, green curve, under the square of the plasmon density, red curve, gives rise of the antibunching in the $g^{(2)}$ -function for resonant excitation. For a larger detuning $\Delta\omega_{ext}$ the square of the plasmon density correlation is larger than the density correlation giving rise of bunching. Considering a quite large detuning of the external optical field with respect to the surface plasmon resonance, both quantities are equal ($\langle a^\dagger a^\dagger aa \rangle \approx \langle a^\dagger a \rangle^2$) and the hybrid system shows a coherent statistic.

For a distance of $R = 10$ nm and a Förster interaction of $V_{12} = 0.45$ meV between the quantum dots, a asymmetric line-shape of the plasmon density and density correlation occur. Interestingly, the density correlation is way more shifted than the plasmon density. This is regarded to the fact that the excitation of density correlations are in a higher order of excitation from the ground state by the external optical field. Due to this higher order the induced changes of the dipole moments by the Förster interaction between the quantum dots enters in a higher order for higher quantities, this enhances the asymmetry in the spectrum. We will discuss this in more detail during the investigation of the plasmon probabilities $\langle |n\rangle \langle n| \rangle$. Since the square of the plasmon density is always smaller than the density correlation, the system show bunching over the whole spectral range under investigation. It is worth to mention that for a large detuning the system adopt the coherent statistic of the external optical field.

If the distance between the quantum dots and the silver sphere is increased to $R = 16$ nm and the Förster interaction between the quantum dots is included, the line-shapes of the square of the plasmon density and density correlation changes. Compared to the case with stronger interaction ($R = 10$ nm) especially the square of the plasmon density is way narrower. Again, we observe the asymmetry induced by the Förster interaction for the density correlation function $\langle a^\dagger a^\dagger aa \rangle$. This induced dip, $\langle a^\dagger a \rangle^2$ is smaller than $\langle a^\dagger a^\dagger aa \rangle$, give rise to bunching at $\approx 3\text{meV}$. For larger detuning both observables are almost equal ($\langle a^\dagger a^\dagger aa \rangle \approx \langle a^\dagger a \rangle^2$) and the statistic of the hybrid system is coherent.

In the following, the occurrence of the asymmetry and in general the shape of the squared plasmon density $\langle a^\dagger a \rangle^2$ and the plasmon density correlation $\langle a^\dagger a^\dagger aa \rangle$ is discussed. Since we are using number states for the plasmons, the density $\langle a^\dagger a \rangle$ and the density correlation

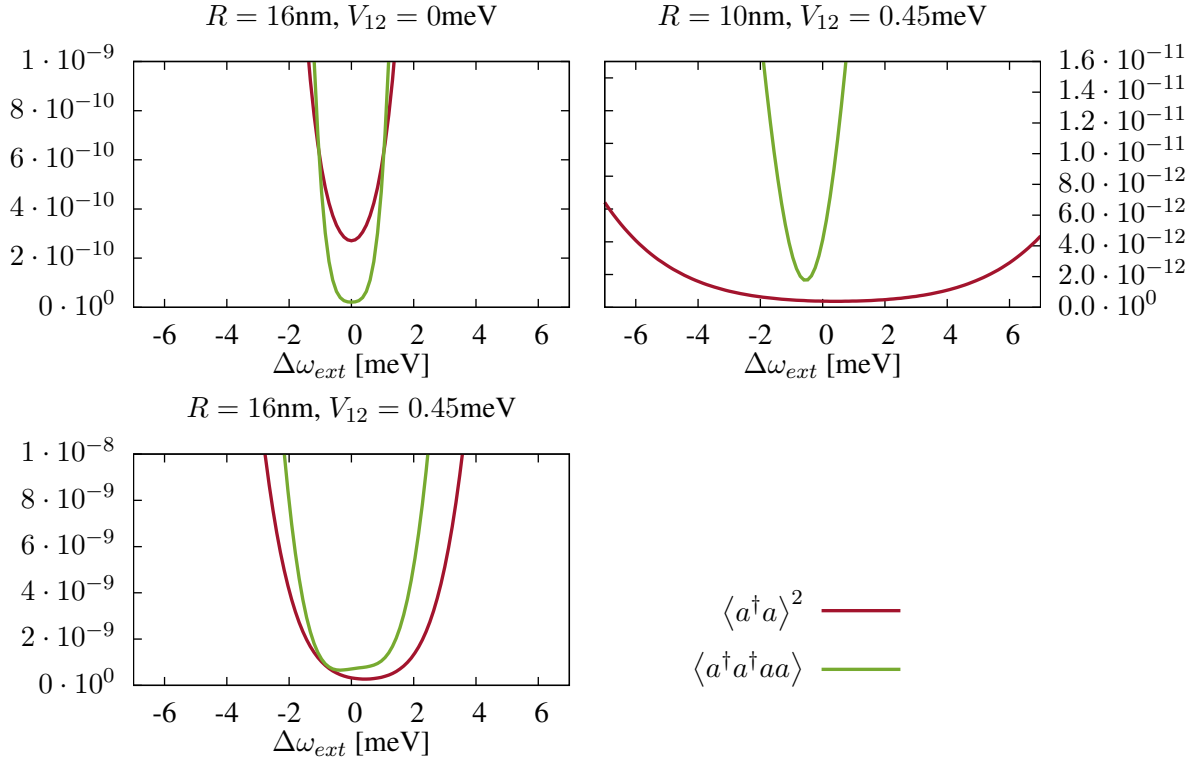


Figure 4.14 | Plasmon density correlation ($\langle a^\dagger a^\dagger a a \rangle$) and the square of the plasmon density ($\langle a^\dagger a \rangle^2$) versus the detuning to the external optical field. The parameters for the single plots correspond to the one chosen for the second order correlation function in Figure 4.13

$\langle a^\dagger a^\dagger a a \rangle$ are calculated by using the probabilities to find a certain plasmon number in the system ($|n\rangle\langle n|$). The $g^{(2)}$ -function written with the plasmon probabilities reads

$$g^{(2)} = \frac{\sum_{n=0}^{\infty} \langle a^\dagger a^\dagger a a |n\rangle\langle n| \rangle}{\left(\sum_{n=0}^{\infty} \langle a^\dagger a |n\rangle\langle n| \rangle \right)^2} = \frac{\sum_{n=2}^{\infty} n(n-1) \langle |n\rangle\langle n| \rangle}{\left(\sum_{n=1}^{\infty} n \langle |n\rangle\langle n| \rangle \right)^2} . \quad (4.39)$$

In the last step we used the fact that the density correlation function $\langle a^\dagger a^\dagger a a \rangle$ lowest order is $n = 2$ and for the plasmon density $\langle a^\dagger a \rangle$ the lowest order is $n = 1$, respectively.

In Figure 4.15 we plot the first 5 orders ($n=0-4$) for the coupled system. Note, beside the 0-th order ($\langle |0\rangle\langle 0| \rangle$) all plots are on a logarithmic scale. Between one order and the next higher one are approximately three orders of magnitude difference, due to the fact that the external optical field is weak. Since we are in the weak field limit, the lower the plasmon order n , the higher the corresponding probability. Therefore, the lowest order entering the observable will dominate the observable. For the plasmon density it will be $\langle |1\rangle\langle 1| \rangle$ and for the plasmon density correlation $\langle |2\rangle\langle 2| \rangle$, due to the occurring prefactors in (4.39). Similar to the $g^{(2)}$ -function, without Förster interaction between the quantum dots the line-shape is symmetric (red curve in Figure 4.15). The curve of $\langle |1\rangle\langle 1| \rangle$ is almost like the one of $\langle a^\dagger a \rangle$ and

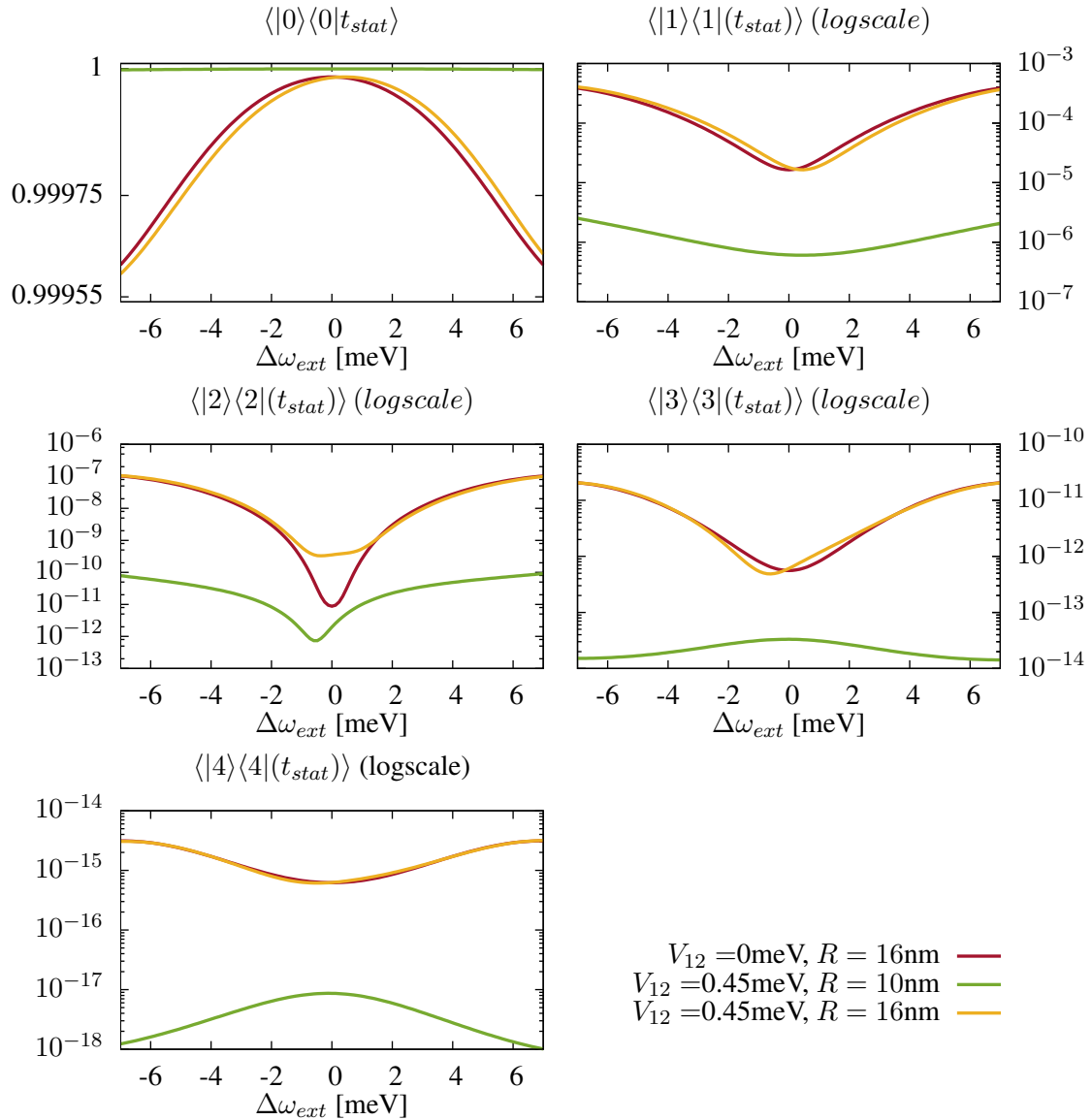


Figure 4.15 | First lowest order of the coupled hybrid system with and without Förster interaction between the quantum dots. Besides the Förster interaction the distance R between the quantum dots and the silver sphere is varied. The orders 1 up to 4 are plotted on a logarithmic scale.

$\langle |2\rangle\langle 2|$ almost as the plasmon density correlation $\langle a^\dagger a^\dagger a a \rangle$ in Figure 4.14, showing that the lowest order entering the observable of interest dominate its behavior. The same is valid for the cases including the Förster interaction between the quantum dots. To understand the occurring asymmetries in more detail, we calculate the eigenenergies and corresponding transition dipole moments for excitations from the ground state to one excitation in the hybrid system. Since we are now interested in the occurring asymmetries, we need to include the Förster interaction between the quantum dots. This is in contrast to the calculations done in Section 4.5.2 and 4.5.3 for the Rayleigh spectra where the Förster interaction does not play a role. For a hybrid

system consisting of two quantum dots coupled to each other by the Förster interaction and both coupled to a metal sphere the system matrix reads

$$\underline{\underline{S}} = \begin{pmatrix} E_{g_1} & V_{12} & g \\ V_{21} & E_{g_2} & g \\ g & g & E_{sp} \end{pmatrix} \quad (4.40)$$

for one excitation in the system, either one exciton or one plasmon is excited. We assume the same coupling between quantum dot 1/2 to the plasmonic system g . Furthermore all constituents of the hybrid system should be in resonance ($E_{g_1} = E_{g_2} = E_{sp}$). The newly formed eigenenergies of the coupled system are

$$\hbar\omega_{sp} - V_{12} \quad \text{and} \quad 1/2(2\hbar\omega_{sp} + V_{12} \pm \sqrt{8g^2 + V_{12}^2}). \quad (4.41)$$

As in the cases before, the new energies depend on the interaction between the constituents of the hybrid system. In the same manner we find the transition dipole moments from the ground state to a state with one excitation μ_{tot} in the system to be

$$\mu_{tot} = 0 \text{enm} \quad \text{and} \quad \mu_{tot} = \sqrt{2 \pm \frac{2V_{12}}{\sqrt{8g^2 + V_{12}^2}}} \left(\frac{\chi}{2} + \mu \frac{V_{12}}{4g} \mp \mu \sqrt{\frac{1}{2} + \frac{V_{12}^2}{16g^2}} \right). \quad (4.42)$$

Comparing this result to the one without Förster interaction ($\mu_{tot} = \chi/\sqrt{2} \pm \mu$) it is obvious that including the Förster interaction between the two quantum dots causes a coupling strength g dependency of the transition dipole moments. Therefore, one can expect different asymmetries for different coupling strengths due to their influence on the transition dipole moments. A higher coupling strength reduces the redistribution of the dipole moments by the Förster interaction between the quantum dots. This behavior is shown in Figure 4.16 for different strengths of the Förster interaction between the quantum dots. Without the Förster interaction, the total transition dipole moment is independent of the coupling strength g between the excitonic and plasmonic system (red curve). For a small coupling strength g , the total dipole transition is enhanced and equal for different Förster interactions V_{12} . It is worth to mention that the case $g = 0 \text{meV}$ and $V_{12} = 0 \text{meV}$ is not defined since in this case the dipole transition does not exist, no new states are formed. Only the interactions within the hybrid system allows these new transition dipole moments calculated in (4.42). For a higher coupling strength g in Figure 4.16 the influence of the Förster interaction V_{12} on the total transition dipole moment decreases. This behavior can also be seen by taking a closer look at Figure 4.15 for the different plasmon order, it is clear that the case for weaker coupling ($R = 19 \text{nm}$) shows way stronger asymmetries than the one for stronger coupling ($R = 10 \text{nm}$). Which is in good agreement with Equation (4.42) and Figure 4.16. It is important to keep in mind that the calculated eigenenergies and transition dipole moments of the coupled hybrid system are only valid for one excitation in the system. To calculate the corresponding eigenenergies and transition dipole moments for higher excitations in the system is straightforward but leads to large expressions which are only evaluated numerically. Not only the equations are way larger, additionally a lot more transitions are allowed between different excitations in the hybrid system. But they explain why the transition dipole moments are redistributed to higher energies, like for $\langle |2\rangle \langle 2| \rangle$

yellow curve in Figure 4.15, or to lower energies, like for $\langle|3\rangle\langle 3|\rangle$ and $\langle|4\rangle\langle 4|\rangle$ yellow curve in Figure 4.15.

To understand the spectra of different orders n in Figure 4.15 in more detail we need to take a closer look at the polariton states formed in the system. These states are formed by the interaction between the excitonic system and the plasmonic one. In the uncoupled system $g = 0$ meV the four excitonic states, two valance and two conduction band states, as well as the multiple excitations of the plasmonic system are present (top of Figure 4.17). The transition energies are chosen to be resonant ($E_{g_i} = E_{sp}$). The plasmonic system is represented by an infinite number of states. If the coupling between the constituents is taken into account, hybridization of the energies take place and plasmon polaritons are formed. We show these newly formed eigenenergies schematically in the bottom of Figure 4.17. In the coupled system one ground state is present. The electrons in the quantum dots are in the valence band and no plasmon is excited. For one excitation in the coupled hybrid system three states are possible. First, the one electron in either one of the quantum dots is in the valence band or second, on plasmon on the silver sphere is excited.

For all higher excitations ($n \geq 2$) four possible states exist. Both quantum dots could be excited and $n - 2$ plasmons, either one of the quantum dots and $n - 1$ plasmons or n plasmons. All these possible states are depicted in Figure 4.17. Transitions from one of these manifolds to another one may occur. Without interactions between the constituents these states are proper eigenstates of the system.

Including the Förster interaction between the quantum dots V_{12} and the coupling between the excitons and the plasmons g , new eigenstates, polaritons, are formed, see bottom of Figure 4.17. The newly formed polariton states determine the dynamics of all observables of interest. In principle, these states correspond to a Jaynes-Cummings ladder with multiple states on each step. It is possible to calculate the eigenenergies and corresponding transition dipole moments via diagonalization of the system matrix. Nevertheless, the resulting equations are quite large and aggravating to handle. Therefore, to gain deeper insight into the new eigenenergies we calculate the spectra for transitions from one manifold to the next higher one in Figure 4.18. We plot the spectra for the plasmon density $\langle a^\dagger a \rangle$ and the excitonic polarization ρ_{vc} , respectively. Beside the transitions between a coupled manifold, we additionally vary the damping of the plasmonic system. This variation enables us to make the new resonances visible in the coupled hybrid system. Beside the new eigenenergies some basic trends are also visible. For both cases, without and with the Förster interaction between the two quantum dots, decreasing the damping of the plasmon strongly decrease the linewidth of the resonances in the spectra. Furthermore, the number of excited plasmons is increased, recognizable in the large area underneath the

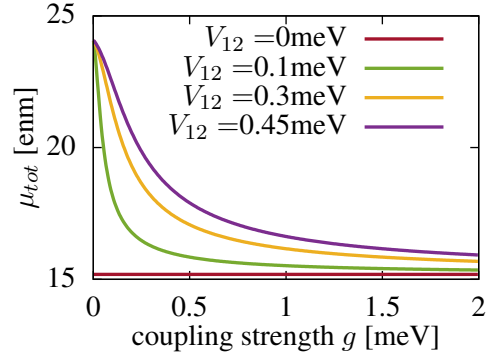


Figure 4.16 | Total transition dipole moment (Equation 4.42) for different Förster interaction strength between the two quantum dots versus the coupling strength between excitonic and plasmonic system.

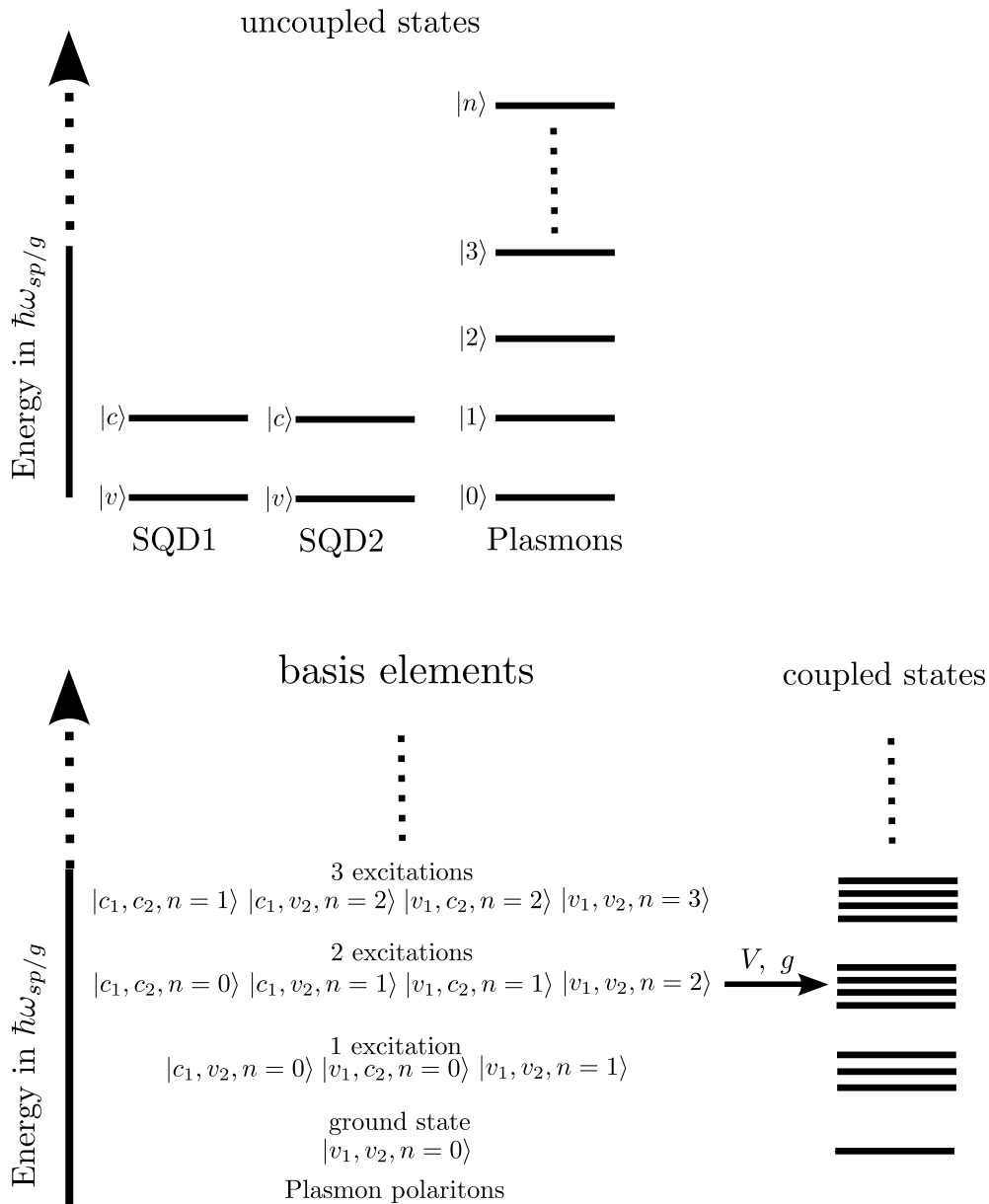


Figure 4.17 | Sketch of the system states. **Top:** System states for the case without interaction between the excitons and plasmons. **Bottom:** System states (polaritons) for the case with coupling between the constituents of the hybrid. In both cases excitonic and plasmonic transition are in resonance ($E_{g_i} = E_{sp}$). The picture is taken from [TCRK13].

spectra. Even the excitonic polarization is increased for decreasing plasmon damping (second and fourth row in Figure 4.18).

Necessary for basic insights into the results of the $g^{(2)}$ -function is the understanding of the asymmetries occurring in the spectra. As mentioned already earlier, these asymmetries are introduced by the Förster interaction between the quantum dots. Since this interaction shifts

eigenenergies and redistributes the transition dipole moments for certain transition. To make this shifts and redistribution visible, we calculated the plasmon density $\langle a^\dagger a \rangle$ and the excitonic polarization ρ_{vc} versus the detuning to the external optical pump field (Figure 4.16). Due to the large damping of the plasmonic system, the spectra are spectrally very broadened, which makes it impossible to recognize the proper eigenenergies in the system. Even the redistribution of the dipole moments can be barely seen for a realistic plasmon damping of 21 meV. For a plasmonic damping rate of 10 meV, it starts to become obvious that some single peaks consist of several peaks. This can be nicely seen in Figure 4.16. If we now decrease the plasmon damping further to a unrealistic value of only 1 meV, the new eigenenergies are nicely visible in the spectra. One can easily see how the number of transitions increases for increasing excitations in the hybrid system. For a small damping of the plasmonic system it is also possible to observe the redistribution of the transition dipole moments due to the Förster interaction between the quantum dots. Clearly recognizable in the different heights of several peaks when comparing the case without Förster interaction with the case with Förster interaction.

In the case without Förster interaction (upper two rows) all the spectra of the plasmon density $\langle a^\dagger a \rangle$ and the excitonic polarization ρ_{vc} are symmetric. The two optical resonances are clearly visible for transitions from the ground state to the state with one excitation in the system (manifold $0 \rightarrow 1$). The transition at $\omega_{ext} = 0$ meV has no optical transition dipole moment, thus this transition is forbidden. With increasing excitations in the system, the number of possible transitions increases. This can be seen by the raising number of peaks in the spectra for higher manifolds. The maximum number of possible transitions from manifold n to manifold $n + 1$ is eight. It is worth to mention that some of the transitions may be dipole forbidden or degenerated, which leads to a smaller number of peaks in the spectra than eight.

Finally, we plot the second order correlation function for two different hybrid systems versus the Förster interaction between the quantum dots. Again, we consider the distances 10nm and 16nm between the quantum dots and the silver sphere. The plasmons and excitons are resonantly coupled and we assume excitation on resonance and by a detuning of 0.9meV. Changing the Förster interaction strength between 0meV and 0.45meV changes the emission statistic of the hybrid system drastically.

Figure 4.19 shows the $g^{(2)}$ -function versus the Förster interaction. For a distance of 10nm between the constituents of the hybrid system bunching is increased. The more interesting case is the one with a distance of 16nm between the quantum dots and the silver sphere. In this case the emission statistic is antibunched without Förster interaction between the quantum dots. With increasing Förster interaction the emission statistics changes to the coherent and finally to a bunched statistic for a strong interaction between the quantum dots.

The second case is shown in Figure 4.20. The hybrid system is excited off-resonantly, the detuning between the external optical field and the resonances of the hybrid system is 0.9meV. In this case, the bunching is strongly enhanced by the Förster interaction between the quantum dots for a distances of 10nm (38.8meV) between the quantum dots and the silver sphere. For a distance of 16nm the emission statistics change from bunched over coherent and finally to a bunched statistic.

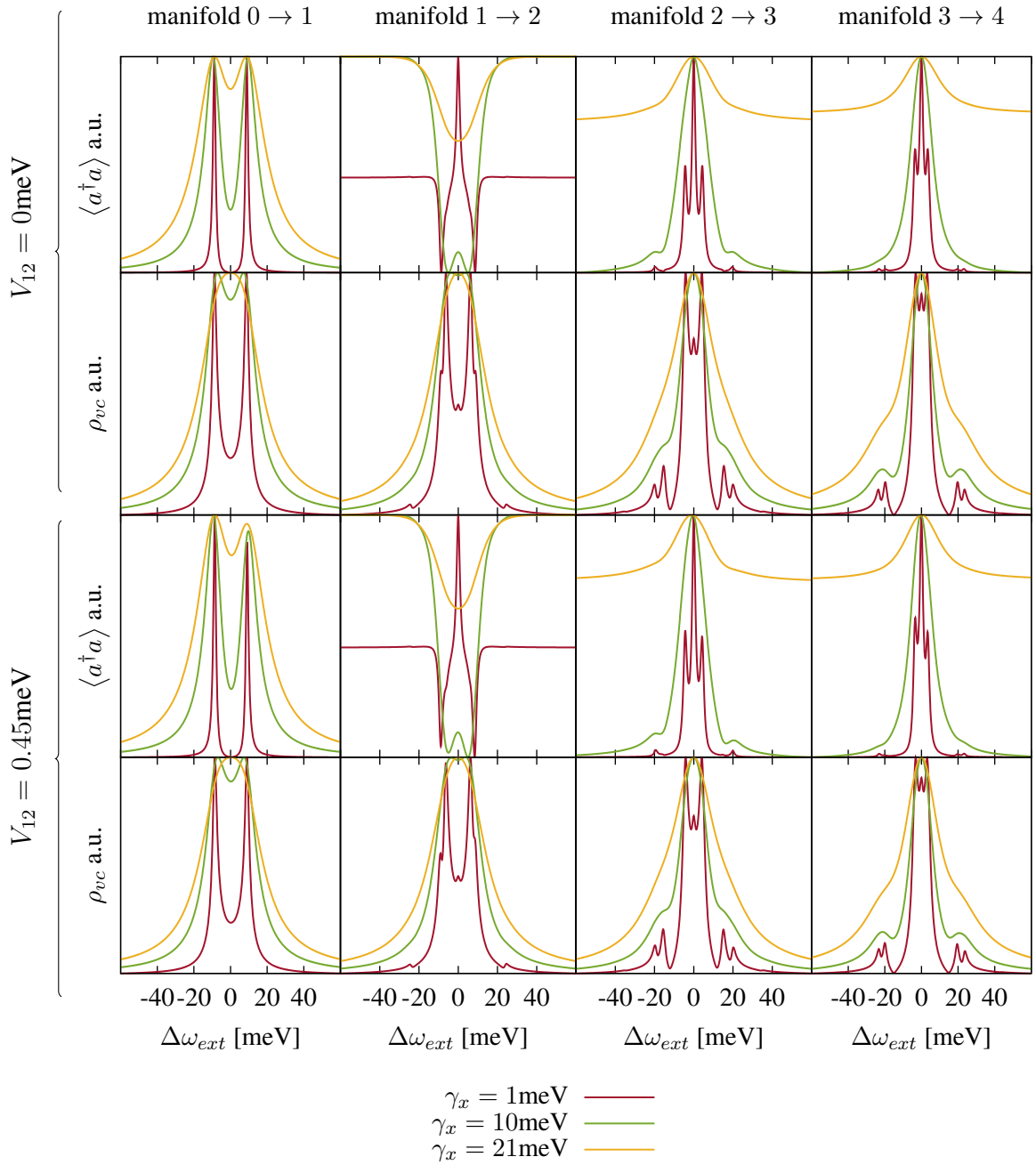


Figure 4.18 | Hybrid system restricted to transitions from one manifold to the next higher one. The distance between the quantum dots and the silver sphere is $R = 15$ nm, corresponding to an interaction strength of $g = 11.5$ meV. We show the spectra for the plasmon density $\langle a^\dagger a \rangle$ and the excitonic polarization ρ_{vc} without the Förster interaction ($V_{12} = 0$ meV) between the quantum dots (upper two rows) and with the Förster interaction ($V_{12} = 0.45$ meV) between the quantum dots (two lower rows). Furthermore, we varied the damping of the plasmons to make the newly formed resonances visible in the coupled hybrid system. The spectra are normed.

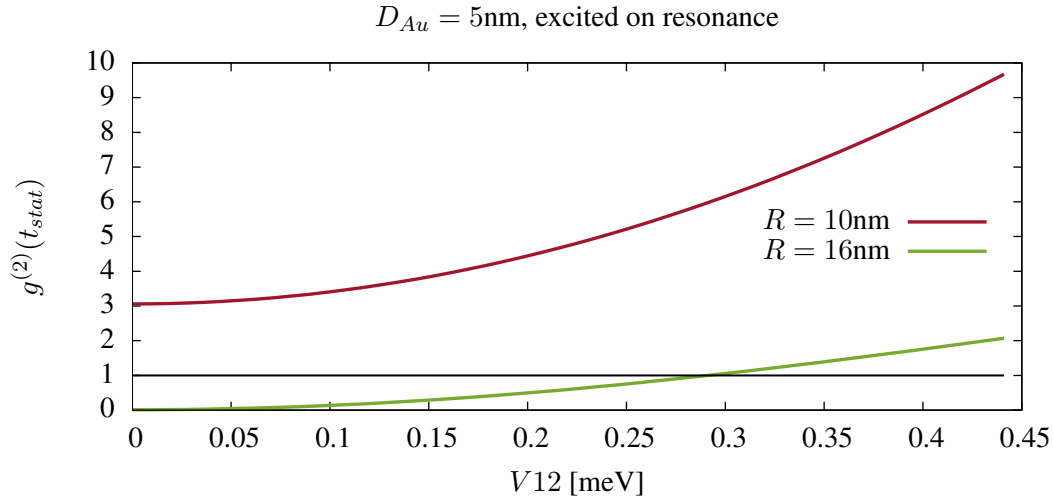


Figure 4.19 | Second order correlation function versus the Förster interaction between the quantum dots. The hybrid system is excited resonantly by the external optical field.

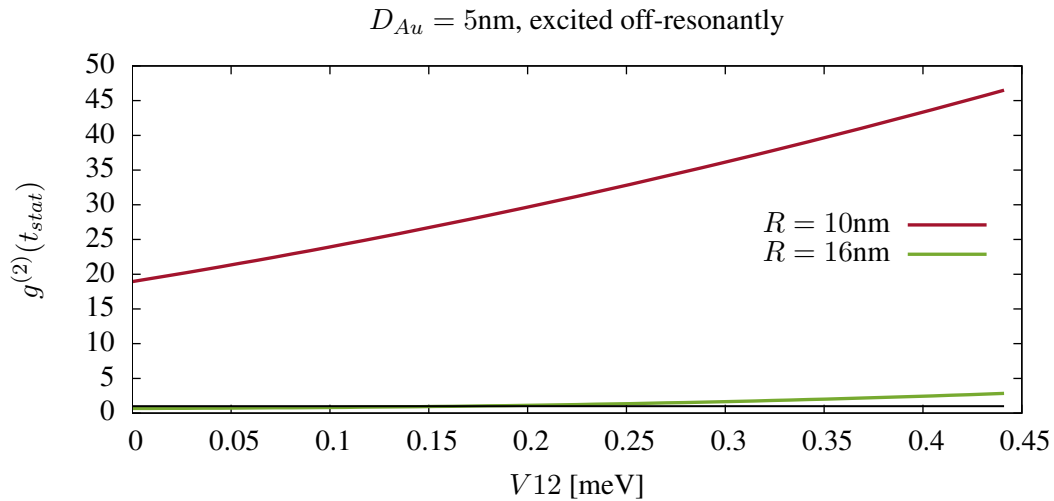


Figure 4.20 | Second order correlation function versus the Förster interaction between the quantum dots. The hybrid system is excited off-resonantly ($\Delta = 0.9\text{meV}$) by the external optical field.

Chapter 5

Ensemble of coupled quantum dot and gold sphere hybrid systems

In this chapter we use our theory to compare with experiments. First, the experimental setup and the wet chemical synthesis are briefly explained. Second, we will introduce our theoretical system. After setting up a parameter free theory, we calculate the absorption spectra and compare the theoretical results with the experiments. After reproducing all qualitative trends as observed in the experiment, we investigate the temporal evolution of the coupled hybrid system. For the coupled case we compare weakly and strongly coupled hybrids and discuss the influence of the coupling between the constituents on the temporal dynamics of the far field. We found that hybrids with a strong coupling decay temporally way faster than weakly coupled hybrid system. This can be traced back to excitation transfer between the constituents and the huge damping in the plasmonic system mostly due to Ohmic losses and surface scattering. In the end, to finally compare our theoretical calculations with the experimental data, we introduce the averaging process used to model the ensemble of many hybrid systems measured in the experiments. We find great qualitative agreement and for small gold spheres the quantitative agreement is pretty striking, too.

5.1 Introduction to the hybrid system and experimental setup

The hybrid systems were synthesized in the group of Horst Weller (Institut für Physikalische Chemie, Universität Hamburg and The Hamburg Center for Ultrafast Imaging, Hamburg). The optical measurements were carried out in the group of Tony Heinz (Department of applied Physics, Stanford University and SLAC, National Accelerator Laboratory, Menlo Park) and in the group of Holger Lange (Institut für Physikalische Chemie, Universität Hamburg and The Hamburg Center for Ultrafast Imaging, Hamburg). A sketch of the system is shown in Figure 5.1. The Cd/Se quantum dots are surrounded by a polymer shell to ensure a certain distance to the metal sphere and to attach the lipoic acid needed for the connection to the metal sphere. With this lipoic group it is possible to connect the metal spheres and quantum dots by simply mixing the two water-based solutions. Details for the chemical preparation of the systems are given, e.g., in [PSF⁺12]. The minimum distance between quantum dots and metal sphere is at least 5nm to ensure coupling between both constituents of the hybrid system, but to avoid direct electron transfer from the quantum dots to the metal sphere and vice versa.

Furthermore, this distance ensures no overlap of the electronic wave functions, thus Dexter like energy transfer processes do not play a role [SKR15]. The synthesis was designed in such way that no/very few free quantum dots are in the solution. On the other hand it was checked that no clusters are formed and that in most of the cases only one quantum dot is coupled to a metal sphere. Therefore, a hybrid system consisting of one quantum dot coupled to a metal sphere is the proper subunit to describe the sample. It turned out that the best mixture between the solutions containing the quantum dots and the one with the gold spheres is 1:1. For a high ratio of quantum dots to gold spheres, a lot of the quantum dots remain uncoupled in solution. These uncoupled quantum dots lead to a very long living fluorescence signal and would cover the signal of the coupled hybrid systems of interest. In the other extreme case with a low ratio of quantum dots to gold spheres, the gold spheres start to cross-link and form clusters. This creation of clusters leads, e.g., to a "shoulder" arising in the absorption spectra for decreasing distance between two gold spheres due to the excitation of higher order plasmon modes [LJC⁺12].

Two different species of quantum dots were synthesized: The first ones are CdSe/ZnS core-shell quantum dots with a photoluminescence maximum at 528 nm, called "green quantum dots" in the following. The second type synthesized are CdSe/CdS/ZnS core-shell-shell quantum dots with a maximum of the photoluminescence at 596 nm, called "red quantum dots" in the following.

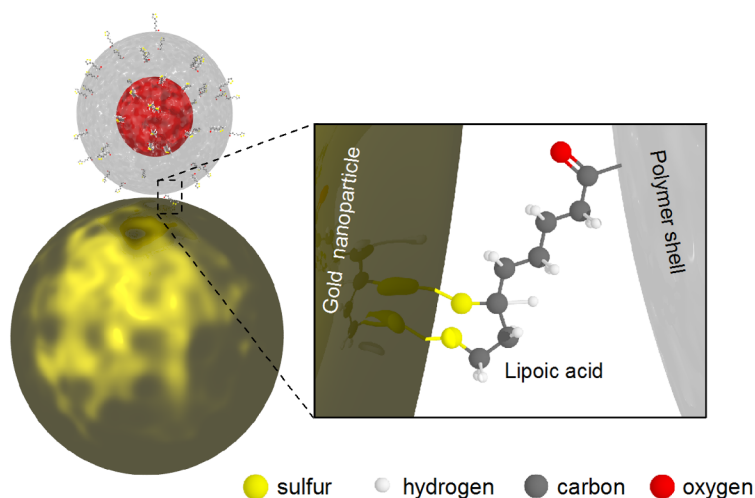


Figure 5.1 | Sketch of the gold sphere and the quantum dot surrounded by polymer shell securing the right distance between the gold sphere and the quantum dot. The lipoic acid group, linking gold sphere and the polymer shell, is magnified. (Picture taken from (in submission))

We will start with a brief introduction in the theoretical framework we established to model the experimental setup. First of all, the excitation in the experimental setup needs to be modeled. Therefore, we start with fitting the pump pulse in frequency domain to the measured spectra. The pulse width in time domain is taken from the handbook of the laser system. We assume a pump pulse with a Gaussian shape

$$E(t, \omega) = \frac{n}{\tau} \exp \left[-\frac{1}{2} \left(\frac{t - t_{off}}{\tau} \right)^2 - i\omega t + i\frac{k}{2} (t - t_{off})^2 \right] \quad (5.1)$$

where τ is the width of the pulse, t_{off} the time offset and ω the frequency. Important is additionally the quadratic chirp of the pulse k . This chirp needs to be included to fit the experimental pulse in frequency domain. The pulse used in the experiment is not Fourier limited. Consequently, it contains more than one frequency. Without the quadratic chirp in Equation (5.1) the Fourier transform of the pulse in time domain would be extremely narrow in frequency domain. Including the chirp allows us to obtain a good fit.

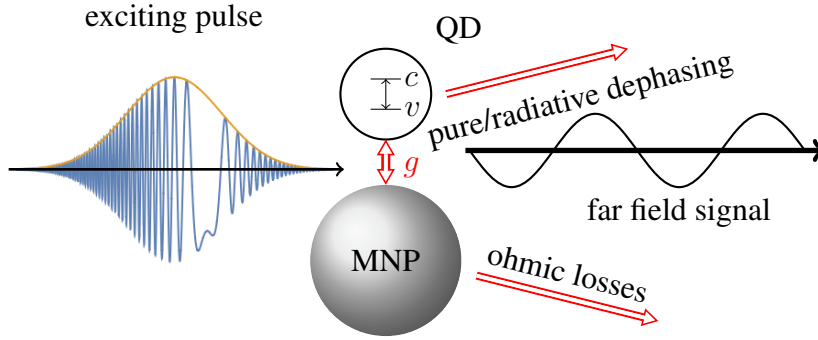


Figure 5.2 | Sketch of the theoretical framework employed to model the experiments. The system is excited with a chirped pump pulse. The excitons in the quantum dots interacts via Coulomb coupling with the plasmons on the metal sphere. Both sub-systems, the excitonic one as well as the plasmonic one are damped. The damping for the plasmons is mostly due to ohmic losses and the excitonic one to pure dephasing, nevertheless we also include radiative dephasing for incoherent quantities to describe the fluorescence lifetime properly. Including all these parameters, we calculate the far field signal/fluorescence signal.

After modeling the excitation pulse we proceed with a proper description of the experiment. To model the quantum dot we include the dominant exciton. This allows us to describe the quantum dot as a two level system. For the metal spheres we take the dipole mode into account [RDSF⁺10]. We neglect higher order modes in the quantum mechanical calculations, since their resonances are detuned with respect to the dipole resonance of the plasmon [SK11, BSSB06]. The resonance energy

$$\omega_l = \omega_{sp} \sqrt{\frac{\omega_l}{l + (l + 1)\epsilon_{out}}} \quad (5.2)$$

of the l -th plasmon mode is determined by the resonance energy of the dipole mode ω_{sp} and the dielectric function of the environment ϵ_{out} of the metal sphere. This spectral shift of the resonance energies for higher order modes drastically decrease the spectral overlap between the excitons and plasmons. Due to the resulting small overlap, we do not expect strong coupling and thus no deviations in the dynamics if higher order plasmon modes are included. Furthermore, higher order plasmonic modes are not excitable by the external optical field as long as the wavelength of the external field is way larger than the diameter of the metal sphere. This assumption holds in all cases we investigate. Therefore, we neglect all higher plasmonic modes

in our calculations. For the case of large gold spheres attached to quantum dots with only a small spacer additionally classical calculations were performed by Ziliang Ye (group of Tony Heinz) to ensure the validity range of the dipole approximation. We will see that for large gold spheres and small spacers the agreement between theory and experiment is not that striking as it is for small gold spheres and large spacers.

To model the experiment, we describe the plasmons and excitons in the formalism of second quantization, cp. Hamilton operators [4.2](#)-[4.4](#) and the operator equation [4.19](#) in Chapter [4](#). In contrast to Chapter [4](#) we consider only one quantum dot coupled to the metal sphere, since this is the proper subunit for the description of the sample investigated experimentally. This was checked by TEM pictures of single hybrid systems (c.p. Figure [5.3](#)). This pictures additionally provides information about the distances between the quantum dots and gold spheres, the diameter of the spheres and information whether clusters have been formed or not.

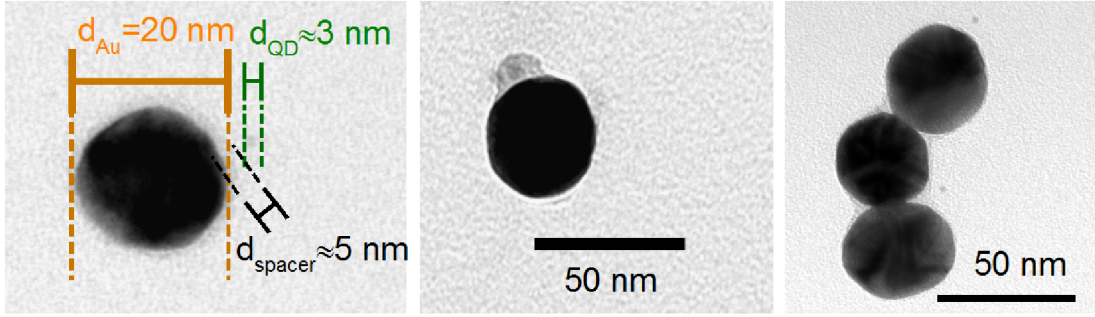


Figure 5.3 | TEM pictures of single systems. The diameter of the gold sphere is 20 nm and the spacer thickness 5 nm (left and middle). The image on the right shows cross-linking of the gold spheres for a high ratio of gold spheres to quantum dots. (Pictures taken from (in submission))

The equation of motion for such a system can be easily extracted from the one for the case of two quantum dots coupled to a metal sphere given in the Appendix [B](#). Assuming conservation of charges in the conduction band n_c and the valence band n_v of the quantum dot ($n_v + n_c = 1$), the generalized plasmon probability $p_{n,m}$ can be expressed in a single exciton basis. We give, as an example, the rule to transcribe from the biexcitonic basis to the single exciton basis for quantum dot 1:

$$p_{n,m} = \rho_{vvvv}^{n,m} + \rho_{vccv}^{n,m} + \rho_{cvvc}^{n,m} + \rho_{cccc}^{n,m} = n_{v_1}^{n,m} + n_{c_1}^{n,m} . \quad (5.3)$$

For a proper description of the losses of the excitonic system we distinguish between radiative and pure dephasing. Radiative dephasing is determined by emission of the excitonic system into the far field and affects coherent quantities (like polarizations) and incoherent quantities (like densities). In contrast, the pure dephasing only affects coherent quantities and is way larger than the radiative dephasing [[Tak93](#)]. The radiative dephasing is included in the same manner as the pure dephasing by a corresponding Lindblad term [[RGTK15](#)]:

$$\mathcal{L}_{pure} = \frac{\gamma_{pure}}{2} \left(2A\rho A^\dagger - A^\dagger A\rho - \rho A^\dagger A \right) . \quad (5.4)$$

The general operator A is in the case of radiative dephasing $a_{c_i}^\dagger a_{c_i} - a_{v_i}^\dagger a_{v_i}$ and $\rho_{vc} = a_v^\dagger a_c$ in the case of pure dephasing. These Lindblad terms are used additionally in the operator

equation 4.19 to obtain the equations of motions including pure and radiative dephasing. The pure dephasing strength is extracted from [Tak93]. To determine the strength of the radiative dephasing we fit the far field signal of a single quantum dot to the experimental results of an ensemble of quantum dots (Figure 5.4). We assumed a mono-exponential decay of the far field signal for quantum dots only.

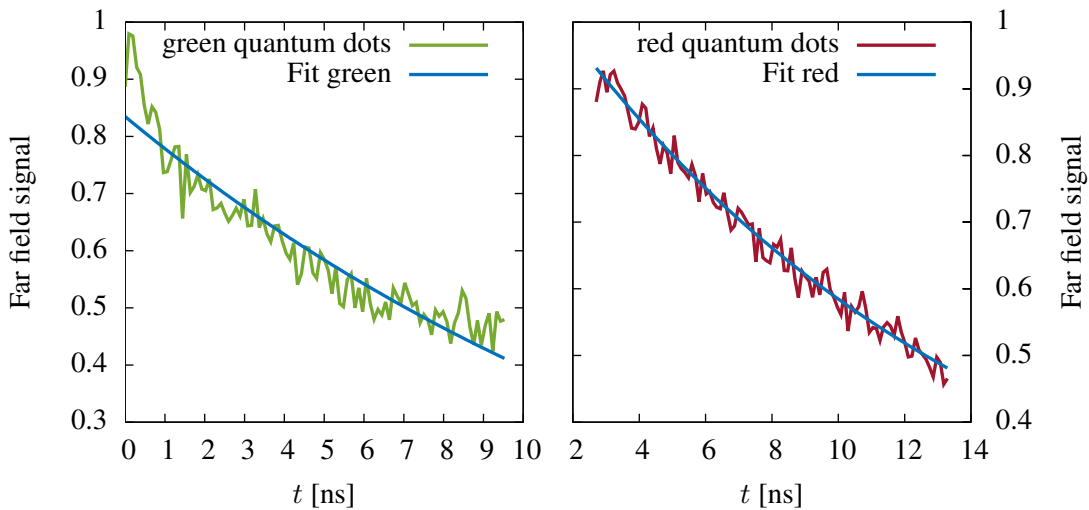


Figure 5.4 | Mono-exponential fit to determine the radiative dephasing of the quantum dots. **Left:** Measurement of the green quantum dots and fit to the data. **Right:** Comparison between experiment and fit to the data for the red quantum dots.

Considering only the relaxation of the quantum dot after an arbitrary excitation, the far field signal is given by

$$I_{far}(t) = e^{-\gamma_{rad}t} - b \quad (5.5)$$

with the radiative dephasing γ_{rad} and an offset parameter b . This implies that the conduction band density decays mono-exponentially after an arbitrary excitation when no interactions are present. We find the best fit for a radiative dephasing of $\gamma_{rad} = 2 \cdot 10^{-8}\text{fs}^{-1}$ for the green quantum dots and $\gamma_{rad} = 6 \cdot 10^{-8}\text{fs}^{-1}$ for the red quantum dots. The offset parameter b is of no physical interest. Obviously, the fit for the red quantum dots is more striking than the one for the green. The green quantum dots show especially for short times a stronger decay. This may be related to defects within the quantum dots. The radiative decay rate, we are interested in, is given by the decay for larger times ($t > 2\text{ns}$). In this regime the fit to data of the green quantum dots is pretty striking.

Since the experimental measurement of pure dephasing is challenging, we use the theoretical results of Takagahara [Tak93]. We obtain 0.053fs^{-1} as pure dephasing for CdSe quantum dots at room temperature. The dipole moment of the quantum dots $\mu = 1.84 \text{ enm}$ was taken from [EB97]. The resonance of the quantum dots are taken from the measured spectra and the size of the gold spheres as well as the distances between the quantum dots and the gold spheres are extracted from TEM images. Resonances and damping rates for the plasmons are derived from the material parameter of gold and the dielectric function of the environment using the theory introduced in Section 2.1.2.

A table summarizing all parameters used to model the measurements and about their derivation or references is given in Appendix C.

5.2 Characterization of the uncoupled hybrid system constituents and introducing observables of interest

After all parameters for the system are fixed, we start with the single constituents of the system. Without any interaction between the plasmons and the excitons, we compare our theory with the experimental measurements. We start with the absorption spectra of the uncoupled quantum dots and gold spheres shown in Figure 5.5. The green quantum dots are close to the plasmonic resonances (green curve). In contrast, the red quantum dots are detuned to the plasmonic resonances by roughly 300-400 meV (red curve). The plasmonic resonance energy shifts for larger spheres towards lower energies [CSW89, KDD06]. To calculate the shown theoretical spectra we only extract the resonance energies of the quantum dots from experimental spectra. All other parameters are calculated theoretically or obtained from independent experiments. The quantum dot spectra are broadened mainly by pure dephasing. Concerning the experimental spectra in Figure 5.6 it is worth to mention that the spectra of the metal spheres are measured as absorption spectra and the ones of the quantum dots as photoluminescence spectra. Due to the very weak absorption of quantum dots in solution it is hard to measure their spectrum in absorption.

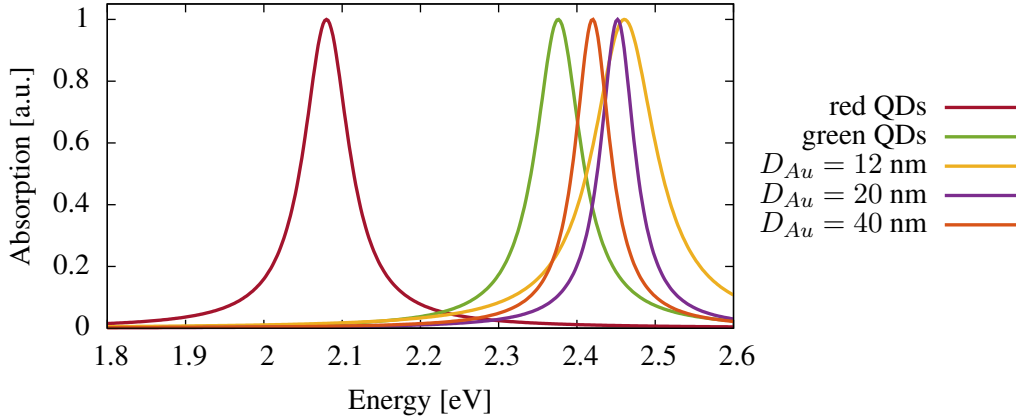


Figure 5.5 | Linear spectra of the uncoupled single constituents of the hybrid system (quantum dots and metal spheres with different diameter D_{Au}). Note, the resonance energy of the quantum dots was determined by spectral measurements, all other parameters are obtained theoretically or by independent measurements.

To investigate the temporal evolution of the hybrid system and to calculate the spectra afterwards, we focus on the far field emission of the system (Section 4.4.1):

$$\begin{aligned}
 I_{far}(t) &= \langle P^\dagger P \rangle = \langle (\mu a_c^\dagger a_v + \chi a^\dagger) (\mu a_v^\dagger a_c + \chi a) \rangle \\
 &= \chi^2 \langle a^\dagger a \rangle + 2\chi\mu \operatorname{Re} [\langle a_c^\dagger a_v a \rangle] + \mu^2 \langle a_c^\dagger a_c \rangle
 \end{aligned} \tag{5.6}$$

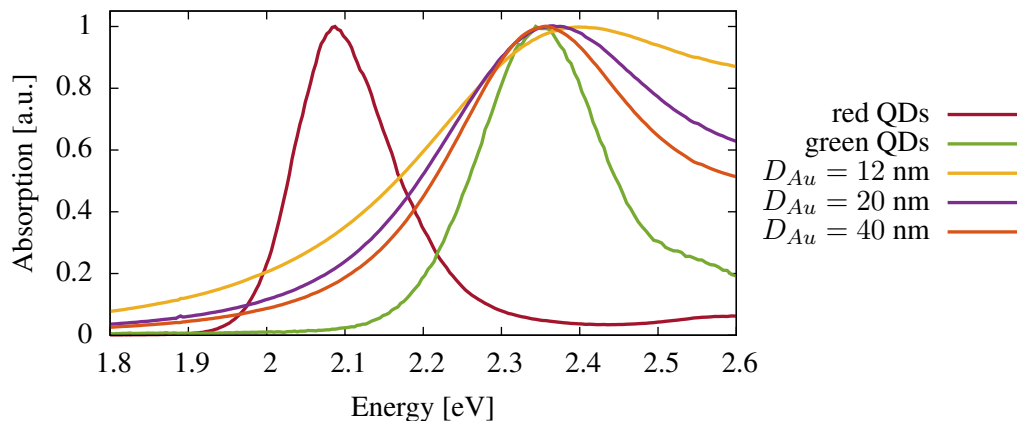


Figure 5.6 | Measured spectra of the uncoupled constituents of the hybrid system. The spectra of the green and red quantum dots are fluorescence spectra. The gold spheres are measured in absorption.

which is given by the product of the polarization operators P of the hybrid system. The far field intensity is an incoherent quantity since it comprises of density like terms, i.e. the plasmon density $\langle a^\dagger a \rangle$ and the conduction band density $\langle a_c^\dagger a_c \rangle$. One could think about factorizing the far field intensity on the level of classical polarizations, but this would lead to false results. The major point is for example the polarization of the quantum dot: In the case of a factorized far field intensity, the occurring quantum dot polarizations are mainly damped by pure dephasing. In the case of the unfactorized far field signal, the occurring density are damped by radiative dephasing only. Since the pure dephasing is orders of magnitude larger than the radiative dephasing a factorized far field intensity would decay much faster than an unfactorized one. Therefore, the unfactorized far field signal is of major interest when we compare theory and experiments.

The measured spectra are plotted in Figure 5.6. Comparing the theoretical results with the measurements, one clearly recognize the quantitative agreement. The size dependent shifts within the theoretical spectra are the same as in the experimental ones. The plasmon resonances shift for larger sphere diameters to lower energies. It is worth to mention that the measured spectra are spectrally broadened in comparison to the theoretically ones. This is due to inhomogeneous broadening, which is the result of different metal sphere diameters in the ensemble. Different metal sphere diameters result in slightly different resonance frequencies and averaging over all broadens the peak in the spectrum. A similar explanation holds for the quantum dots. Again, inaccuracies during the synthesis results in a number of resonance frequencies in the ensemble of quantum dots, which broadens the spectrum. It is worth to mention that this inhomogeneous broadening is not included in our theory.

In Figure 5.7 the spectra of the red quantum dots (red curve) and the spectra of the red quantum dots coupled to gold spheres with different diameters are plotted. For the coupled hybrid system, a filter is used to block the laser excitation and the scattering of the gold spheres. Therefore, only the excitonic part is detected. The pump pulse excites the system at an energy of 2.1 eV, indicated by the arrow in Figure 5.7.

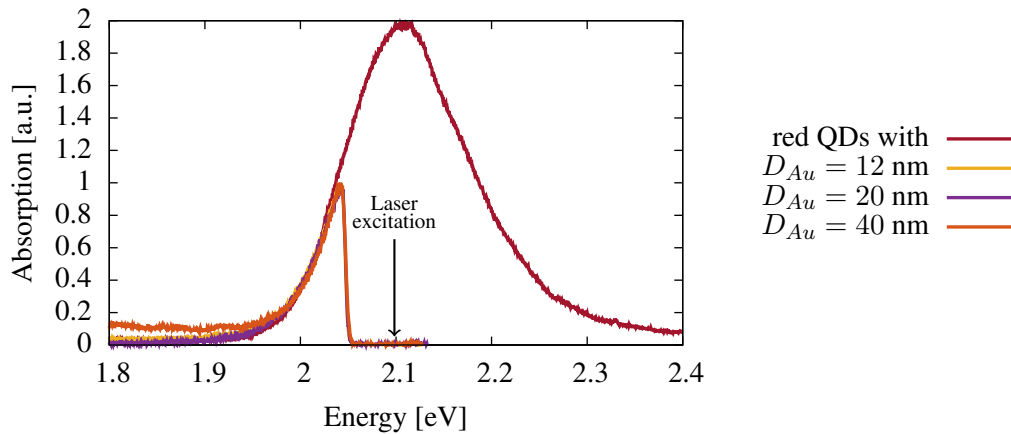


Figure 5.7 | Spectra of the red quantum dots only (red curve) and the red quantum dots coupled to gold spheres with different diameters. For the coupled systems the spectra are recorded with the used spectral filter to block the laser pulse and the light scattered by the gold.

5.3 Coupling between the constituents of the hybrid: Comparison between the dipole-dipole interaction and a full classical calculation

In the following we will discuss the coupling between the constituents of the hybrid system. The coupling between the plasmons and the excitons is modeled as in Chapter 4 as a dipole-dipole coupling in the quantum mechanical calculations. Nevertheless, to ensure the validity of the dipole approximation in the range of interest, classical calculations were performed by Ziliang Ye (Group of Tony Heinz). In this classical calculations the electric field distribution of an electric dipole in front of a gold sphere is calculated by solving the Maxwell equations numerically [ABN06]. To obtain the losses of the electric dipole due to the presence of the metal sphere, the field inside the sphere, induced by the electric dipole, is calculated and a volume integration over the sphere is performed [Rup82]. It is worth to mention that the results are the induced losses of the excited electric dipole into the metal sphere and not the coupling between excitons and plasmons. This calculation is repeated for several diameters of the metal sphere and different spacer thicknesses. A comparison of both theories is shown in Figure 5.8.

For spacer thicknesses of 10 nm and 15 nm both, the coupling strength and the losses induced by the metal sphere, show the same trends (cp. Figure 5.8). As one would expect, for small distances between the quantum dot and the metal sphere, the results starts to deviate. The deviation becomes quite strong when the radius of the metal sphere is larger than the distance (spacer thickness) to the quantum dot. If the metal sphere is large compared to the distance to the quantum dot, higher modes start to influence the coupling between excitons and plasmons. The effect is a near field effect and is not driven by the external field. The higher modes act as additional loss channels for the excitation of the quantum dot. Therefore, the losses calculated classically do not show a pronounced weakening for larger diameters as it is the case for the dipole-dipole coupling strength for, e.g., a 5 nm spacer (red curve in Figure

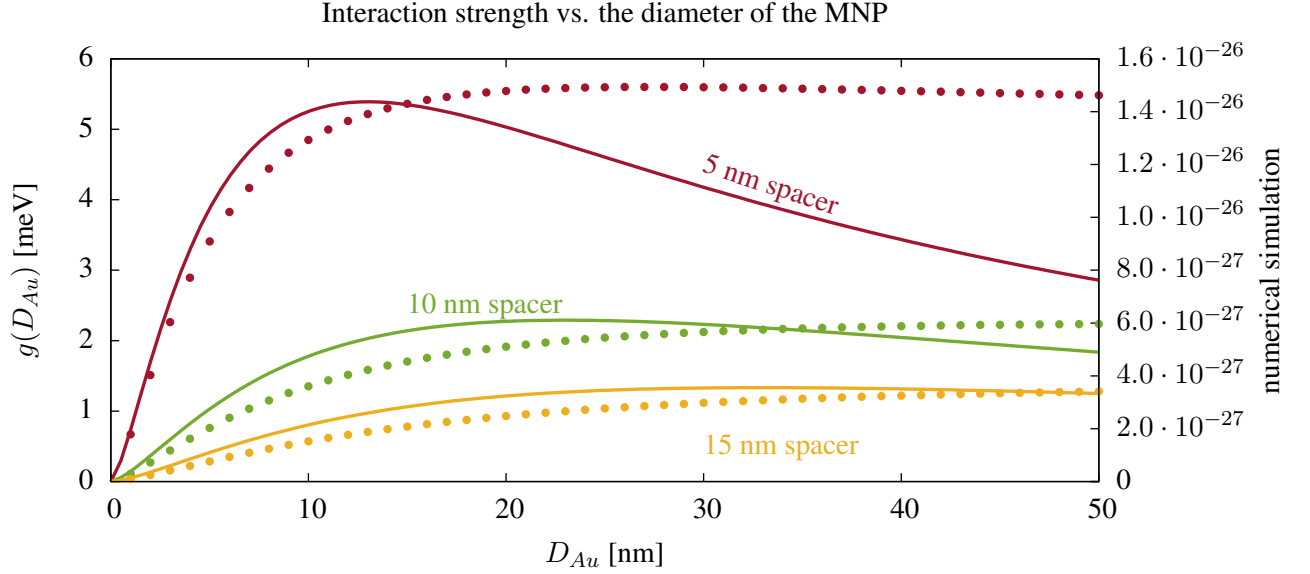


Figure 5.8 | Coupling strength between the excitons and plasmons (solid lines, left scale) versus the diameter of the metal sphere according to Equation 4.5 and the results for the losses of an excited electric dipole nearby a metal sphere (dots, right scale) versus the diameter of the metal sphere. The classical calculation of the losses was done by Ziliang Ye from the group of Tony Heinz.

5.8). The weakening of the coupling strength for larger diameters of the metal sphere is due to two competing terms occurring in the formula of the coupling strength

$$g = \frac{\ddot{s}_\alpha}{\hbar \left(d_{sp} + r_{QD} + \frac{D_{Au}}{2} \right)^3} \sqrt{\frac{6\hbar\eta \left(\frac{D_{Au}}{2} \right)^3}{\pi\epsilon_0}}. \quad (5.7)$$

The first one represents the dipole moment of the gold sphere $\left(\frac{D_{Au}}{2} \right)^{3/2}$ entering the coupling strength. This term increases for larger metal sphere diameter, so it leads to a larger coupling strength. On the other hand, the second term $\left(d_{sp} + r_{QD} + \frac{D_{Au}}{2} \right)^3$ represents the distance between quantum dot and metal sphere and causes a decrease of coupling strength for larger metal sphere diameters. Due to these competing terms the coupling strength is maximized for a certain gold sphere diameter.

It is worth to stress that classical calculations only describe the losses of the quantum dot due to the presence of the metal sphere. However, the calculations are not capable of describing certain optical excitation nor give deeper insights into the microscopic processes occurring in the coupled hybrid system. Therefore, we choose a microscopic model using the dipole approximation to describe the hybrid system. This enables us, for instance, to include proper decay channels for the quantum dot, like pure and radiative dephasing and an exact description of the excitation by the external optical field.

5.4 Temporal evolution of single hybrid systems

We start to investigate the temporal evolution of single hybrid systems first. These single hybrids are needed to calculate the ensemble average in the next section, which will model the measurements performed on the ensemble of hybrid systems. We will determine a lower limit and upper limit for the coupling strengths within a certain ensemble of hybrid systems. The minimum and maximum of the coupling strength is due to variations in the spacer thickness and diameter of the gold metal spheres. Beside their importance for the ensemble averaging, the temporal evolution of single hybrid systems additionally enables us a deeper insight into the physical processes taking place. Therefore, we calculate the temporal evolution for weakly and strongly coupled hybrids. These two extreme systems mark the lower and upper limit of the coupling strength range for the calculation of the ensemble average done later.

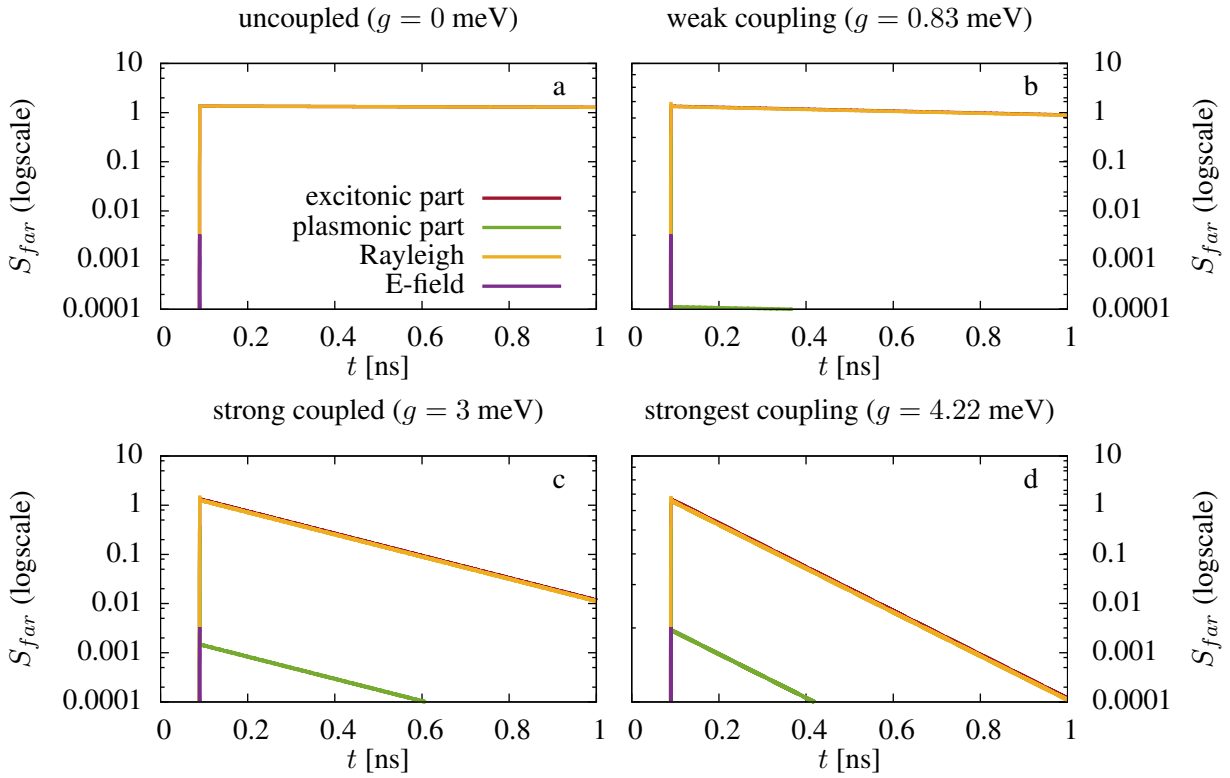


Figure 5.9 | Temporal evolution of single hybrid systems consisting of a red quantum dot and a gold sphere with a diameter of 12 nm. The distance between both constituents is ensured by a 15 nm spacer. **a)** uncoupled hybrid system with a very fast plasmonic decay, within pulse duration, and a very slow excitonic decay due to small radiative dephasing. **b-d)** coupled single hybrid systems for weak and strong coupling between the constituents. Due to the coupling the plasmonic and excitonic parts show the same decay.

We start with the hybrid system consisting of red quantum dots coupled to gold spheres. This system turned out to be the most promising for comparing theory and experiment. The hybrid system with the green quantum dots, which are coupled resonantly to the gold sphere (compare single spectra of the constituents in Figure 5.5), show such a fast decay that it cannot

be resolved with the experimental setup used. We will show later that the hybrid systems with the green quantum dots decay at least 3 orders of magnitude within only a few picoseconds.

In Figure 5.9 we plot the temporal evolution of the plasmonic and excitonic part of the far field signal Equation 5.6 for single hybrid systems. Displayed is the situation with the red quantum dots, a 12 nm gold sphere diameter and a spacer thickness of 15 nm. The weak Gaussian pulse has a pulse duration of 300 fs and is slightly shifted in time. In the case without coupling between the constituents (Figure 5.9 a) the plasmonic part decays within the femtosecond pulse duration, the curve of the pulse and the plasmonic one lie on top of each other. On the other hand, the excitonic part, given by the conduction band density, shows barely any decay within 1 ns. This is due to the small radiative dephasing of the conduction band density. It is worth to mention, that these result could not be obtained if one would express the far field signal (5.6) on the level of classical polarizations by using a factorization scheme. In this uncoupled case, this is due to the large pure dephasing of the polarization of the quantum dot excitation. One could try to avoid this behavior by neglecting the pure dephasing of the polarization which would increase their lifetime drastically. Nevertheless this would be an unphysical and unnecessary approximation, since it can be avoided by a fully quantized theory without factorizations, as it is discussed here. Furthermore, even neglecting the pure dephasing of the quantum dot polarizations would fail when considering coupling between the excitons and plasmons. Polarizations, even without pure dephasing, decay much faster than the incoherent quantities, like the conduction band density, since they couple in first order to the plasmonic system. In contrast, incoherent quantities couple via coherent assisted quantities to the plasmonic system which need to build up first, so the coupling is in second order of the external field.

The temporal evolutions in Figure 5.9 b-d are for 3 selected couplings used later to calculate the ensemble average. It is obvious that the decay of both parts of the far field signal, the plasmonic and the excitonic one, decay faster for increasing coupling between the constituents of the hybrid system. This is due to the large damping of the plasmons. With increasing coupling strength, excitation is more likely transferred from the quantum dots to the gold sphere and in general vice versa. However, because of the large plasmon damping, an excitation transfer from the plasmonic system to the excitonic system is very unlikely since the excitation usually dissipates within the plasmonic system. Therefore, the coupling between the constituents of the coupled hybrid system induces an additional decay channel for the excitonic quantities. This energy transfer highly increases the decay of the excitonic part of the far field signal. On the other hand, this transfer slows down the plasmonic decay (only compared to the uncoupled case!). The height of the kink between the fast decay and the slower long time decay of the plasmonic part is determined by the coupling strength, too. A stronger coupling causes a higher transfer of excitation from the excitonic system to the plasmonic one. Therefore, this transferred energy supports the plasmonic signal earlier than in the case of weak coupling. This can be seen by a higher kink for stronger coupling in the plasmonic part of the signal for an ensemble of hybrid systems.

We also show the results for the hybrid system with the resonantly coupled green quantum dots in Figure 5.10. Note the picosecond timescale in contrast to the nanosecond timescale for the hybrid system with the red quantum dots. For the green quantum dots a system with a 5nm spacer was experimentally realized. Again, the hybrid system is excited by a weak Gaussian pulse with a pulse width of 300fs and the diameter of the gold sphere is 12nm. In the uncoupled case (a in Figure 5.10) the plasmonic part decays instantaneously with the pulse while the

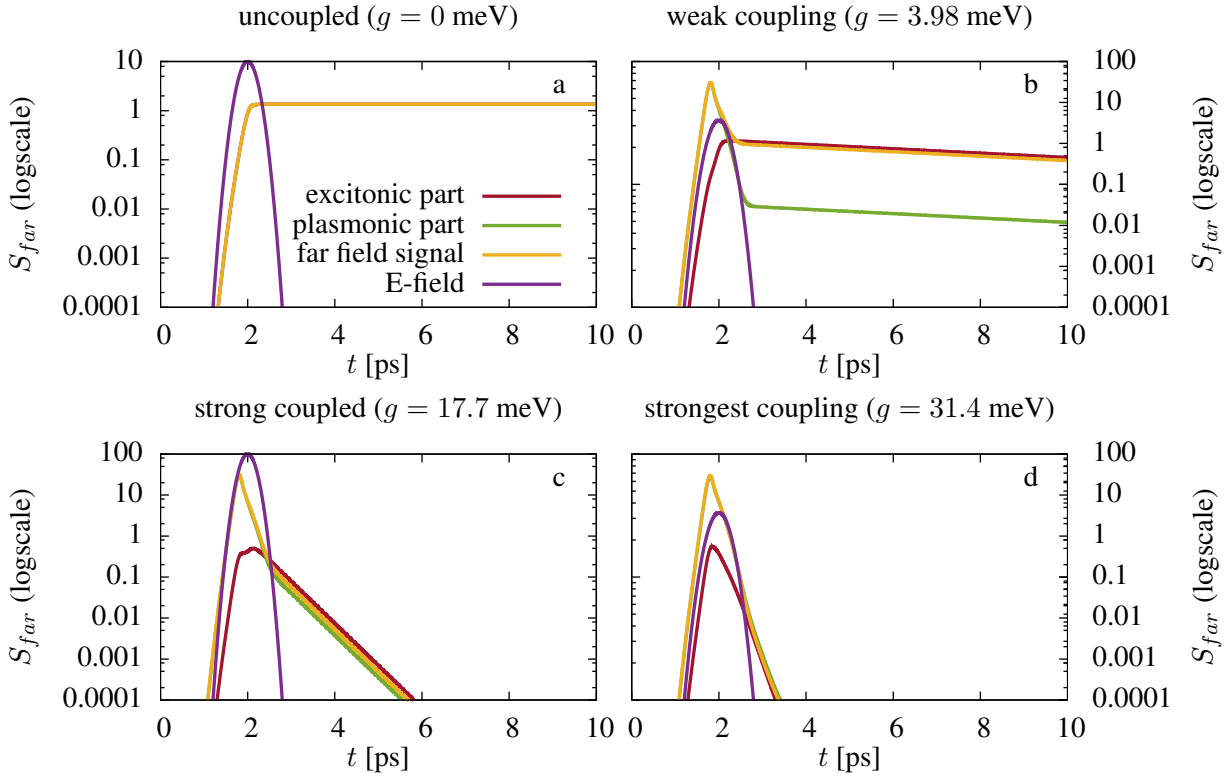


Figure 5.10 | Excitonic and plasmonic part of the far field signal versus time for the hybrid system with green quantum dots and gold sphere with 12nm diameter. **a)** uncoupled constituents, the plasmonic part follows the pulse. **b-c)** coupled hybrid system for different coupling strengths used to calculate the ensemble average.

excitonic part and in consequence the (full) far field signal exhibit a very slow decay. For the coupled hybrid systems (b-d in Figure 5.10) the decay on the long timescale is for all parts of the far field signal and the full signal the same due to the coupling. Similar to the case with the red quantum dots, the decay increases for increasing coupling between the constituents. Additionally, different behaviors during pulse excitation are recognizable. For instance, the excitonic part shows some dips during pulse excitation in c and d in Figure 5.10. These dips are related to the different dipole moments of the excitons and plasmons, which couple these subsystems to the external optical field. Since the dipole moment of the plasmons is way larger than the excitonic ones, energy transfer from the plasmons to the excitons takes place during pulse excitation. For stronger coupling the excitons gain energy from the plasmonic one causing a faster rise time of the excitation. This effect is more pronounced for stronger coupling. In Figure 5.10 d the excitonic part rises almost instantaneously with the plasmonic one, while it is slower for weaker coupling. Since these features take place on a picosecond or femtosecond timescale, they are hard to observe experimentally. Another important point is that any kind of inhomogeneous broadening, due to size variation etc., would smear out the features in the time evolution of the signal.

In the end we can state that the coupling in the hybrid system mixes the damping rates of both constituents with respect to the coupling strength and gives rise to the same decay rates of the plasmonic and excitonic part of the far field for times longer than the pulse duration. The

collective decay is stronger for increasing coupling, which will be important for the discussion of the experimental results. After we have understood the single system, we need to consider several hybrid systems to model the ensemble of hybrid systems measured in the experiment. In the next section we additionally include the measuring process itself by the convolution of the theoretical results with the measured instrumental response.

5.5 Temporal evolution of an ensemble of coupled hybrid systems

In this section we model the ensemble of hybrid systems measured experimentally by calculating a minimal and maximal coupling between the constituents. This variation in the coupling strength is due to variations in the spacer thickness and gold sphere diameter caused by manufacturing fluctuations. Furthermore, we include the measuring process itself into the theoretical description via a convolution of calculated and averaged theory curves with the instrumental response function of the experimental setup. We find good agreement for the red quantum dots and reproduce all trends observed in the experiments. But we will also show that the decay for the resonantly coupled hybrid system, the one with the green quantum dots, is decaying way too fast to resolve with the used experimental setup. The hybrid system of the green quantum dot coupled to a gold sphere decays at least three orders of magnitude within a few picoseconds and can only be investigated theoretically at the moment.

To model the ensemble of hybrid system that is measured in the experiments we need to make a rough estimation of the coupling strengths present in the ensemble. To get an educated guess we take manufacturing fluctuations and angle mismatches between the excitonic and plasmonic dipole into account. As manufacturing errors we assume fluctuations in the gold sphere diameter and the spacer thickness which results together in a center to center distance variation between the constituents of the hybrid system of ± 2 nm. This has been verified by TEM images. The angle dependent factor in the coupling strength (4.5) s_α varies from $2/3$ to 2 for the randomly orientated quantum dot dipole moments. The range does not go down to zero (could be expected since $s_\alpha = 3 \cos^2(\theta) - 1$) since the dipole mode is degenerated three times due to rotational symmetry. Therefore, the gold sphere has three dipole modes and the least efficient coupling is $2/3$ and not 0 for varying angles θ between the hybrid axis and the external optical field. Using these angle and distance variations, we calculate the weakest and strongest coupling for ensembles produced and measured in the experiments. We assume that the coupling strengths follow a Gaussian distribution. We weight the computed curves according to this Gaussian distribution and sum over all curves with the certain weight. It is worth to mention that changing the width of this Gaussian distribution over one order of magnitude does not change the results quantitatively. Thereby we ensure that our results are not made up by the average process itself rather than by the ensemble of hybrid systems.

In Figure 5.11 we plot one example illustrating how the average over the ensemble of hybrid systems is calculated. We plot the different temporal evolutions for a system of a gold sphere with a diameter of 40 nm and a spacer thickness of 15 nm. This results, incorporating the manufacturing variations, in a lowest coupling strength of about 2 meV between both constituents of the hybrid system and a strongest coupling of about 5 meV. Shown are the resulting curves for the single hybrid systems and the color code on the right corresponds to the respective coupling used in the calculation of the temporal evolution. The stronger the coupling the stronger the decay of the far field signal, which can be traced back to the huge damping of the plasmons (see Section 5.4 for the single hybrid systems). Beside all the single hybrid

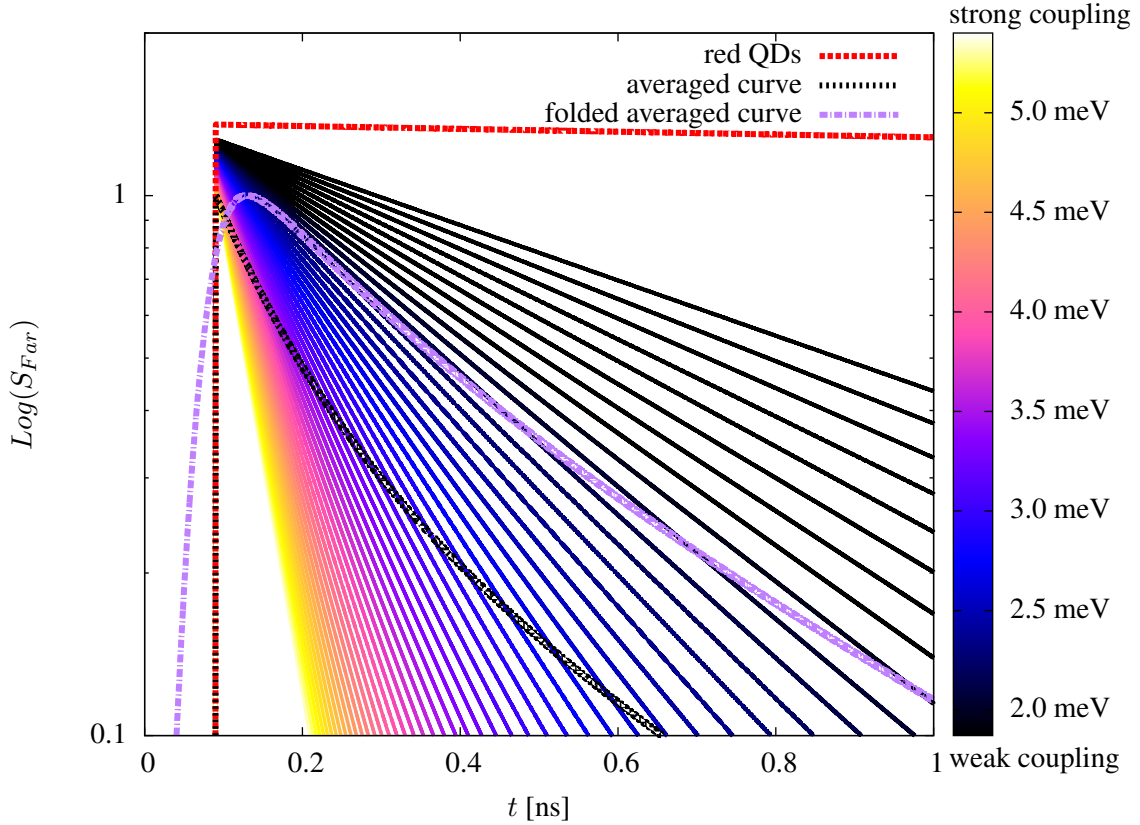


Figure 5.11 | Far field signal for 50 hybrid systems to compute the ensemble average (solid lines). The coupling strength between the constituents of the single hybrid systems is given by the color code on the right. For comparison we additionally plot the curve for uncoupled red quantum dots (red dashed). The averaged curve of the hybrid system ensemble (black dashed) and the averaged curve convolved with the instrumental response function (purple dashed) are shown, too. The systems are excited by a 300fs chirped Gaussian pulse.

systems used, we also show the calculated ensemble average (black dashed curve). This curve incorporates all curves weighted by a Gaussian distribution. Since the experimental setup does not respond instantaneously we need to consider the measuring process itself by convolving the average curve with the instrumental response function. The resulting curve (purple dashed) now includes all necessary information to model the experiment properly, namely the ensemble average and the measuring process. Due to the instrumental response of the experimental setup, e.g., the pump pulse appears way larger in the measurement than it actually is (pulse duration 300 fs).

In Figure 5.12 we plot the different parts of the far field signal (5.6) and the full signal. The curves are for several diameters of gold spheres, for a fixed spacer thickness of 15 nm and for gold spheres coupled to the red quantum dots. Additionally, the time evolution of the uncoupled red quantum dots is plotted for comparison. Similar to the single hybrid systems investigated in Section 5.4, the decay of the signal increases for increasing coupling between the constituents. Experimentally the coupling is adjusted by the spacer thickness and the diameter of the gold

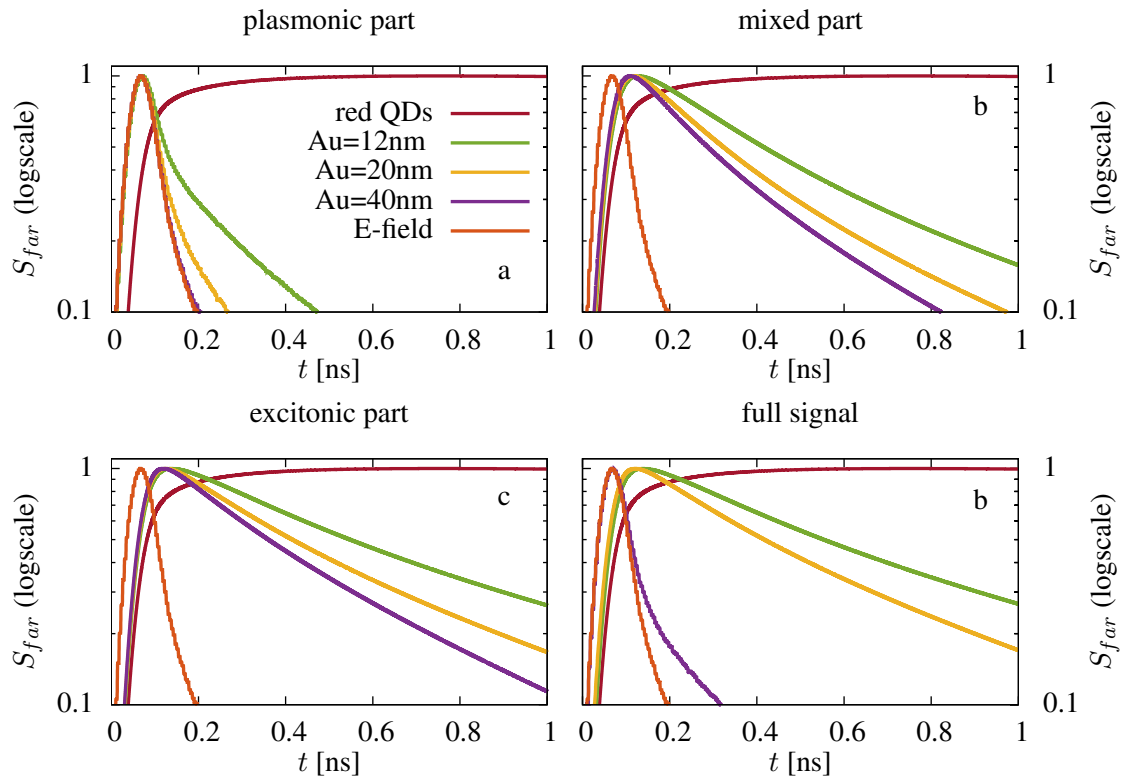


Figure 5.12 | Theoretical curves averaged over an ensemble of 50 single hybrid systems and convolved with the instrumental response function. Shown in a-d are the different parts of the far field signal (5.6) for a spacer thickness of 15 nm and for several diameters of the gold spheres. In c) the complete signal of the hybrid system is shown.

sphere. For a spacer thickness of 15 nm the coupling strength increases for increasing gold sphere diameter (cp. Figure 5.8). Therefore, the systems with the 40 nm gold spheres exhibit the fastest decay. Note, this is no longer valid if the spacer thickness changes due to the competing trends in the coupling strength (4.5): Increasing the gold sphere diameter increases the dipole moment of the gold sphere, this enhances the coupling to the excitons. But on the other hand, increasing the sphere diameter increases also the distance to the quantum dot which reduces the coupling between both constituents of the hybrid system (cp. maxima in Figure 5.8). Nevertheless, for a spacer thickness of 15 nm the trend is monotonic. As one could expect, the plasmonic part shows the fastest decay due to the large losses in the metal. The mixed part is only plotted for sake of completeness, usually it is very small and does not play a role. The excitonic part shows a similar behavior to the one of the single systems in Section 5.4. Increasing the coupling strength between excitons and plasmons increases the decay. We will use this signal to compare the theoretical calculations with the experiments since the plasmonic part is filtered out in the measurements. The last plot in Figure 5.12 shows the full signal. This plot shows clearly which part dominates the full far field signal: For smaller gold spheres (12 nm and 20 nm) the full signal is dominated by the excitonic part, since the excitation of plasmons is too low and they are damped very strong. But, for large gold sphere diameters (40 nm) the huge resulting dipole moment plays a role and more plasmons are

excited. Furthermore, a higher plasmonic dipole moment increases the plasmonic contribution to the far field signal (5.6). Therefore, the full signal is rather dominated by the plasmonic part than the excitonic one. The corresponding plots for a 5 nm and 10 nm spacer are given in the Appendix D.

To compare our results with the experiment we focus on the excitonic part of the far field signal only. This is possible since the elastically scattered plasmonic part is filtered out. We compare our result with the experiment in two different ways: First, we compare the curves for constant sphere diameter and varying spacer thickness (c.p. Figure 5.13) and second, different gold sphere diameters at a constant spacer thickness in one plot (c.p. Figure 5.14).

The explanation for the first case, different spacer thicknesses with a fixed sphere diameter, is pretty simple: Reducing the spacer thickness increases the coupling strength between the excitons and plasmons, this increases the decay strongly which is clearly recognizable in Figure 5.13. Additionally, one can see that the decay becomes faster for larger metal sphere diameters, since larger metal spheres have a higher dipole moment. Therefore, they exhibit a stronger coupling (cp. Equation (4.5)) and stronger decay. The second case, plotted in Figure 5.14, is a bit more complex. Carefully comparing the different plots it becomes obvious that the sequential arrangement of the curves changes: For a 5 nm spacer, the smallest gold sphere ($D_{Au}=12$ nm) shows the fastest decay and the 40 nm metal sphere the slowest. In contrast, for the case with a 15 nm spacer the order is inverse. The 40 nm gold sphere hybrid system exhibits the fastest decay and the ones with 12 nm gold spheres the slowest. Here, two competing mechanisms which determine the coupling strength mix: The first one scales with the gold sphere diameter. Increasing the diameter increases the dipole moment and the coupling strength between the excitons and plasmons leading to a faster decay. On the other hand, increasing the gold sphere diameter also increases the distance between the quantum dots and the gold sphere, which reduces the coupling strength between both constituents of the hybrid system. This interplay provokes the changes in the sequential arrangement of the different curves in Figure 5.14. This behavior can additionally be seen in Figure 5.8 where the coupling strength is displayed versus the diameter of the sphere.

For sake of completeness we show the results for the green quantum dots coupled resonantly to gold spheres, too. As mentioned earlier, this type of hybrid system decays very fast due to the strong coupling between the constituents. In Figure 5.15 we plot the averaged curve and the curve convoluted with the instrumental response function for a system of green quantum dots with a 5 nm spacer. The quantum dots are coupled to gold spheres with different diameters. In the left plot of Figure 5.15 the average over the ensemble is already calculated but not convoluted with the instrumental response function. One can recognize small differences between the differently sized gold spheres. Furthermore, the very short pulse is visible as sharp line. The right plot in Figure 5.15 shows the averaged curves of the hybrid system convoluted with the instrumental response function. Due to convolution, the fast dynamics of the ensemble of hybrid systems are no longer resolved temporally. This result is the same as in the experiments, where the measurements of the green quantum dots coupled to gold spheres results in the instrumental response function.

In conclusion, we find good agreement between the theoretical results and the experimental ones. For the red quantum dots coupled to gold spheres, both, theory and experiments, show the same trends. We reproduce the dependency on the spacer thickness for the decay of the far field signal, small spacer thickness results in a faster decay of the far field signal. Furthermore, we explained the changes in the sequence of the curves for a constant spacer thickness

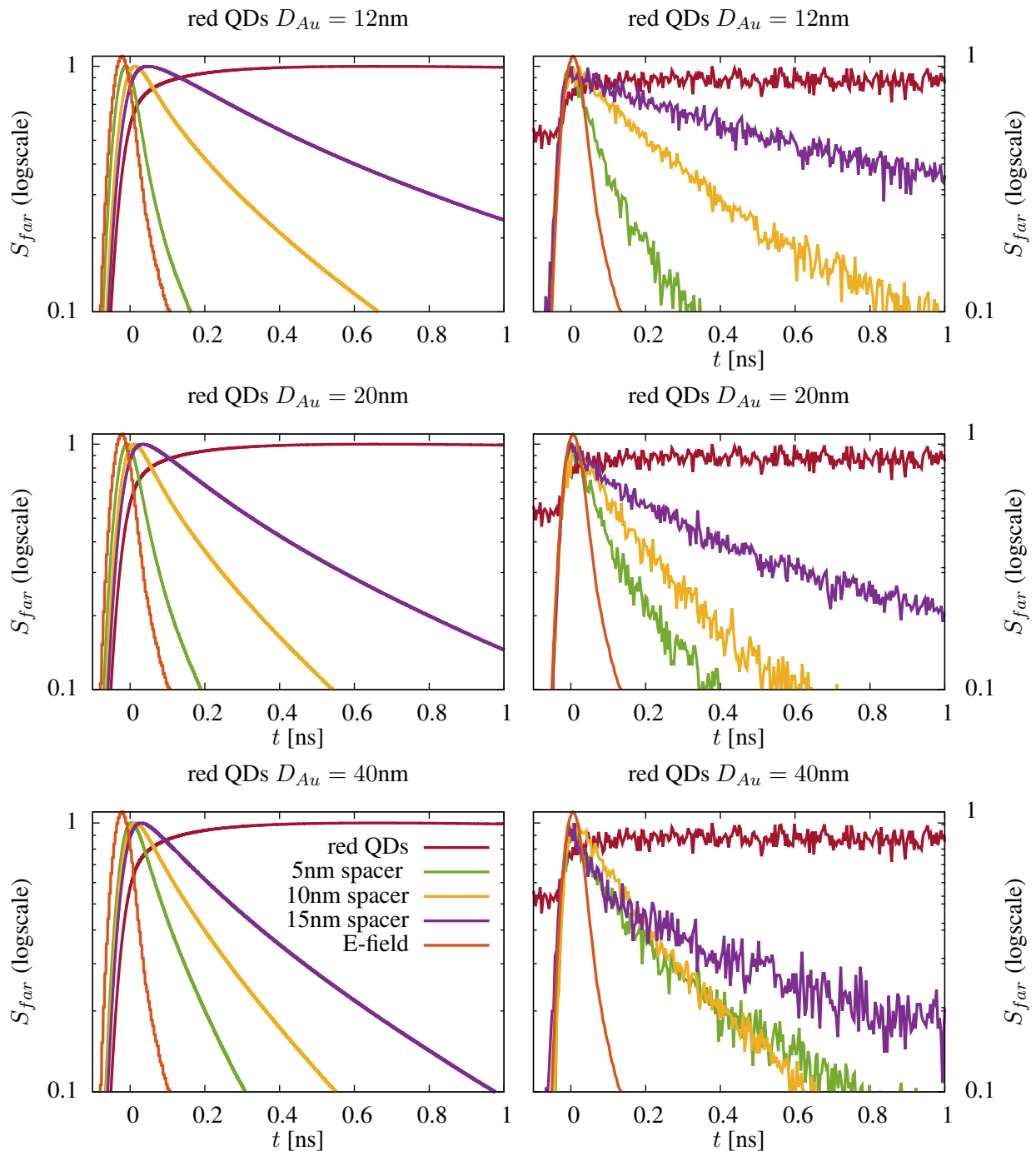


Figure 5.13 | Comparison between the theoretical calculations (left column) and the experimental results (right column). Each plot shows the temporal evolution of the far field signal for a certain gold sphere diameter and different spacer thicknesses. The plots are on a logarithmic scale and normed.

and differently sized gold spheres. For small gold spheres and larger spacer thicknesses even the qualitative agreement is pretty striking. From a theoretical point of view we are able to

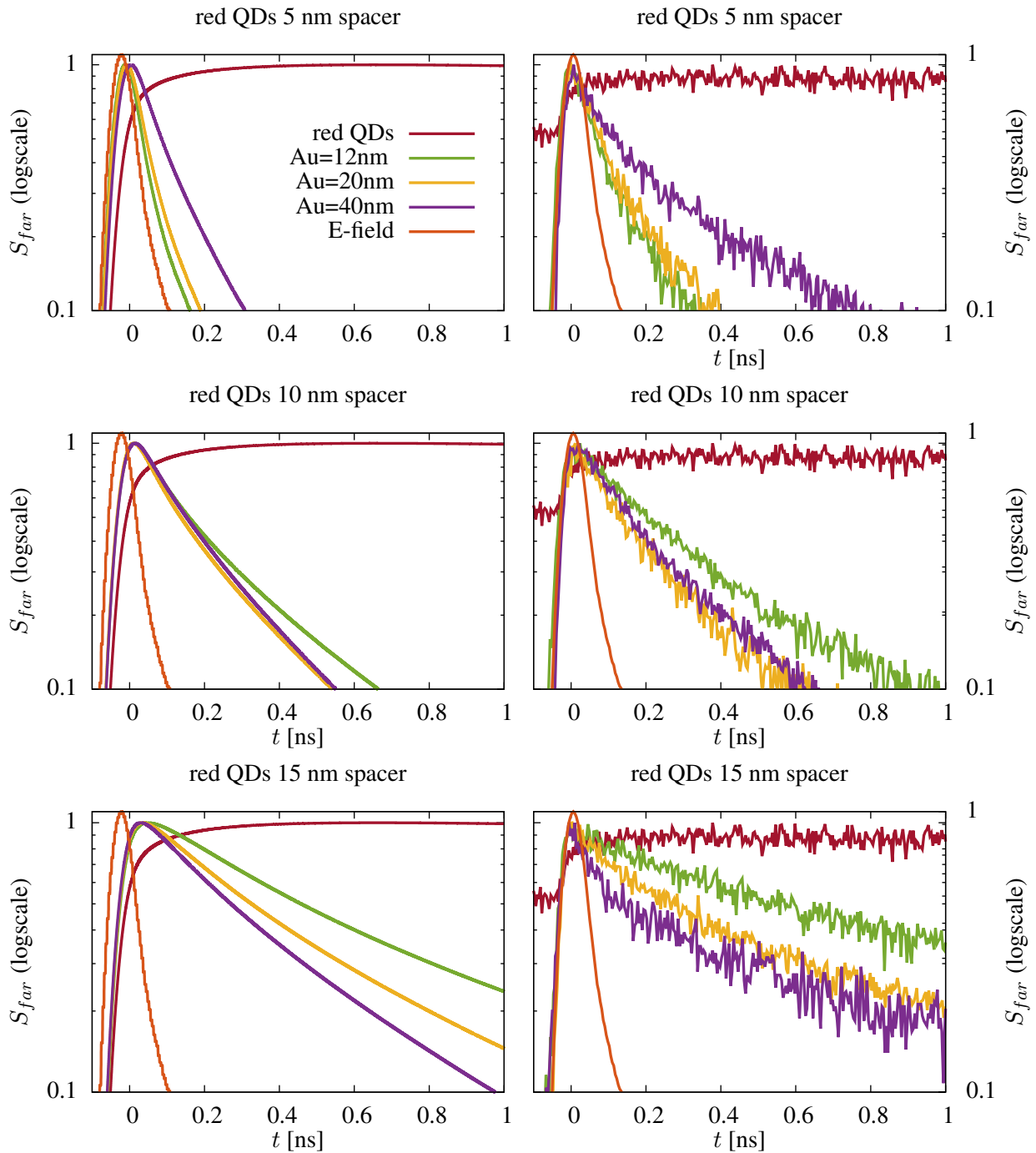


Figure 5.14 | Comparison between the theoretical calculations (left column) and the experimental results (right column). Each plot shows the temporal evolution of the far field signal for a certain spacer thickness and different gold sphere diameters. The plots are on a logarithmic scale and normed.

investigate the hybrid system consisting of green quantum dots and gold spheres. Due to the large spectral overlap, these hybrid systems exhibits an enormously fast decay. On very short

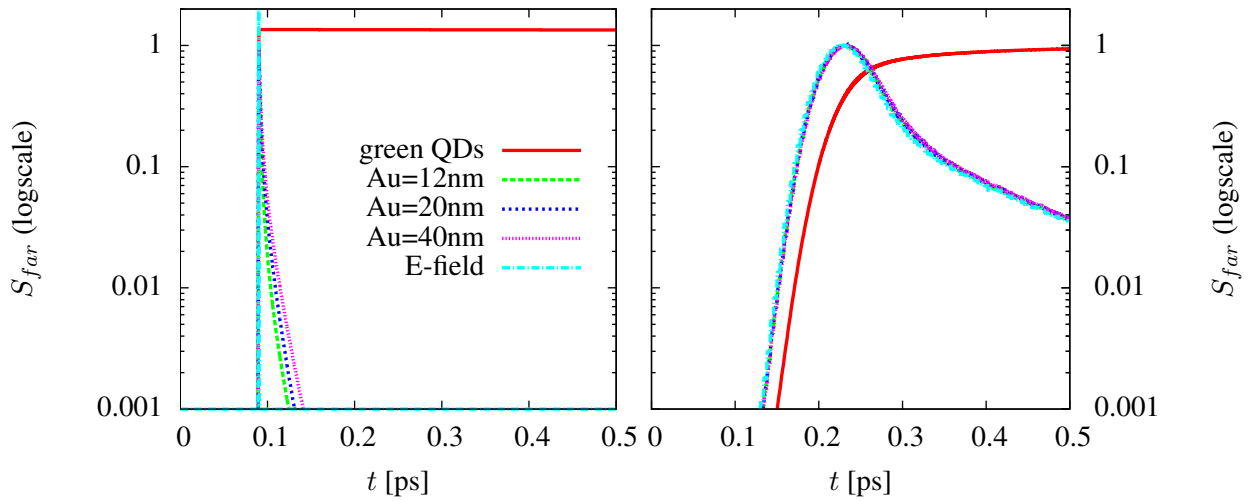


Figure 5.15 | Temporal evolution of the far field signal for hybrid systems consisting of green quantum dots coupled to gold spheres. **Left:** The ensemble average is shown for different gold sphere diameters. **Right:** Far field signal convolved with the instrumental response function.

time scales, the time needed to build up excitations within the hybrid system changes due to the diameter of the gold spheres attached to the quantum dots. However, the dynamics are so fast that they cannot be resolved experimentally, which we also show by investigating the theory curves convolved with the experimental response functions. All these curves share the same slope and cannot be distinguished.

Part IV

Hybrid inorganic organic systems

Chapter 6

Molecules coupled to a semiconductor quantum well

In this chapter we develop a model to describe the energy transfer between a semiconductor substrate and a molecular layer beyond the dipole approximation. These hybrid systems are in the focus of current research since their combination allows them to overcome the limitations of their single constituents. On the one hand, the semiconductor substrate provides high charge-carrier mobility [VKR⁺14] and can be pumped, e.g., electrically. On the other hand, one can design, e.g., the molecules' transition energy according to the required needs. Non radiative energy transfer between the semiconductor substrate and the molecular layer has been investigated theoretically within the point dipole approximation [VKR⁺14, BLRBA99, BLRBA02] and using transition charges [PZMM15]. Such an energy transfer is also found experimentally between a ZnO layer and a molecular monolayer [FKS⁺15, BSX⁺06] and in light-emitting inorganic-organic systems [NCCP08]. Recently it was found that these hybrid systems are capable of exhibiting efficient light emission compared to the organic molecules alone [SBB⁺15]. The theoretical calculations on this subject were started by Eike Verdenhalven, continued by T. Sverre Theuerholz and will be proceeded by Judith Specht.

6.1 Coupling elements of hybrid inorganic/organic systems

In the following we derive the coupling elements between the semiconductor substrate and the molecular layer. Therefore, we use spatial charges, provided by the Fritz-Haber-Institut Berlin, to derive the Coulomb interaction between the molecular layer and the semiconductor substrate. The main idea of this technique is to arrange point charges at the atomic positions in such a way that the complex field distribution of, e.g., a molecule is reproduced. It is worth to mention that the point charges only reproduce the electric field outside the molecule. For our purpose, spatial charges are computed for the molecule (L4P) and the semiconductor layer (ZnO). This technique is very powerful if the electric potential is already known from DFT calculations.

Following [MAR06], we start with the general coupling element $V_{a',b'}^{a,b}$ for the coupling of two molecules. The coupling element is composed of the electron - electron, the electron - nuclei and the nuclei - nuclei coupling.

$$V_{a',b'}^{a,b} = \frac{e^2}{4\pi\epsilon_0} \int d\mathbf{r}_1 \dots d\mathbf{r}_N \int d\bar{\mathbf{r}}_1 \dots d\bar{\mathbf{r}}_N \psi_a^*(\mathbf{r}_1, \dots, \mathbf{r}_N) \psi_b^*(\bar{\mathbf{r}}_1, \dots, \bar{\mathbf{r}}_N) \left[\underbrace{\sum_{i,j}^N \frac{1}{|\mathbf{r}_i - \bar{\mathbf{r}}_j|}}_{\text{el-el}} - \underbrace{\sum_{i,J}^N \frac{Z_J}{|\mathbf{r}_i - \bar{\mathbf{R}}_J|}}_{\text{el-nucl}} - \underbrace{\sum_{I,j}^N \frac{Z_I}{|\mathbf{R}_I - \bar{\mathbf{r}}_j|}}_{\text{el-nucl}} + \underbrace{\sum_{IJ}^N \frac{Z_I Z_J}{|\mathbf{R}_I - \bar{\mathbf{R}}_J|}}_{\text{nucl-nucl}} \right] \psi_{a'}^*(\mathbf{r}_1, \dots, \mathbf{r}_N) \psi_{b'}^*(\bar{\mathbf{r}}_1, \dots, \bar{\mathbf{r}}_N) \quad (6.1)$$

The coordinates of electrons are denoted by the lowercase letters (i, j) and the nuclei ones by the capital letters I and J . $Z_{I/J}$ is the atomic number for the I -th, J -th nucleus of molecule a and b , respectively. To simplify the coupling element, they use that electrons are indistinguishable and thus it is possible to reduce the summation to only two electrons at \mathbf{r}_1 and $\bar{\mathbf{r}}_1$ times N^2 for the coupling between the electrons of molecule a and the electrons of molecule b . They reduce the complexity of the electron - nuclei coupling in the same way.

$$V_{a',b'}^{a,b} = \frac{e^2}{4\pi\epsilon_0} \int d\mathbf{r}_1 \dots d\mathbf{r}_N \int d\bar{\mathbf{r}}_1 \dots d\bar{\mathbf{r}}_N \psi_a^*(\mathbf{r}_1, \dots, \mathbf{r}_N) \psi_b^*(\bar{\mathbf{r}}_1, \dots, \bar{\mathbf{r}}_N) \left[N^2 \frac{1}{|\mathbf{r}_1 - \bar{\mathbf{r}}_1|} - N \sum_J \frac{Z_J}{|\mathbf{r}_1 - \bar{\mathbf{R}}_J|} - N \sum_I \frac{Z_I}{|\mathbf{R}_I - \bar{\mathbf{r}}_1|} + \sum_{IJ}^N \frac{Z_I Z_J}{|\mathbf{R}_I - \bar{\mathbf{R}}_J|} \right] \psi_{a'}^*(\mathbf{r}_1, \dots, \mathbf{r}_N) \psi_{b'}^*(\bar{\mathbf{r}}_1, \dots, \bar{\mathbf{r}}_N) \quad (6.2)$$

They introduce the single particle density $\rho_{a,a'}(\mathbf{r}_1)$ for molecule A

$$\rho_{a,a'}(\mathbf{r}_1) = N \int d\mathbf{r}_2 \dots d\mathbf{r}_N \psi_a^*(\mathbf{r}_2, \dots, \mathbf{r}_N) \psi_{a'}^*(\mathbf{r}_2, \dots, \mathbf{r}_N) \quad (6.3)$$

and in the same manner for the density of molecule B. Due to the orthogonality of the wave functions ψ , the single particle densities fulfill the relation

$$\int d\mathbf{r}_1 \rho_{a,a'}(\mathbf{r}_1) = N \delta_{a,a'} \quad (6.4)$$

with the normalization constant N [Sch03]. Using the single particle density and the orthogonality relation, one can rewrite the Coulomb coupling element $V_{a',b'}^{a,b}$ to

$$V_{a',b'}^{a,b} = \frac{e^2}{4\pi\epsilon_0} \int d\mathbf{r}_1 \int d\bar{\mathbf{r}}_1 \rho_{a,a'}(\mathbf{r}_1) \frac{1}{|\mathbf{r}_1 - \bar{\mathbf{r}}_1|} \rho_{b,b'}(\bar{\mathbf{r}}_1) - \frac{e^2}{4\pi\epsilon_0} \sum_J \int d\mathbf{r}_1 \frac{Z_J}{|\mathbf{r}_1 - \bar{\mathbf{R}}_J|} \rho_{a,a'}(\mathbf{r}_1) \delta_{b,b'} - \frac{e^2}{4\pi\epsilon_0} \sum_I \int d\bar{\mathbf{r}}_1 \frac{Z_I}{|\mathbf{R}_I - \bar{\mathbf{r}}_1|} \rho_{b,b'}(\bar{\mathbf{r}}_1) \delta_{a,a'} + \frac{e^2}{4\pi\epsilon_0} \sum_{IJ} \frac{Z_I Z_J}{|\mathbf{R}_I - \bar{\mathbf{R}}_J|} \delta_{b,b'} \delta_{a,a'} \quad (6.5)$$

By introducing the potential $\Phi_{b,b'}(\mathbf{r})$, they rewrite the coupling element

$$V_{a',b'}^{a,b} = -e \int d\mathbf{r}_1 \rho_{a,a'}(\mathbf{r}_1) \Phi_{b,b'}(\mathbf{r}_1) + \sum_I Z_I \Phi_{b,b'}(\mathbf{R}_I) \delta_{a,a'} \quad (6.6)$$

with the potential for molecule B

$$\Phi_{b,b'}(\mathbf{r}) = -\frac{e^2}{4\pi\epsilon_0} \int d\bar{\mathbf{r}}_1 \frac{1}{|\mathbf{r} - \bar{\mathbf{r}}_1|} \rho_{b,b'}(\bar{\mathbf{r}}_1) + \sum_J \frac{Z_J}{|\mathbf{r} - \bar{\mathbf{R}}_J|} \delta_{b,b'}. \quad (6.7)$$

The potential for the molecule A $\Phi_{a,a'}(\mathbf{r})$ is defined in the same way. The main idea is to approximate this potential by atomic charges, since there exist standard programs to fit the electrostatic potential by atomic charges [MAR06]. With this approximation

$$\Phi_{b,b'}(\mathbf{r}) \approx \frac{1}{4\pi\epsilon_0} \sum_J \frac{q_J(b,b')}{|\mathbf{r} - \bar{\mathbf{R}}_J|} \quad (6.8)$$

they rewrite the coupling element

$$\begin{aligned} V_{a',b'}^{a,b} &= \sum_J q_J(b,b') \left[-\frac{e}{4\pi\epsilon_0} \int d\mathbf{r}_1 \frac{1}{|\bar{\mathbf{R}}_J - \mathbf{r}_1|} \rho_{a,a'}(\mathbf{r}_1) + \sum_I Z_I \frac{1}{|\bar{\mathbf{R}}_J - \bar{\mathbf{R}}_I|} \delta_{a,a'} \right] \\ &= \sum_J q_J(b,b') \Phi_{a,a'}(\bar{\mathbf{R}}_J) \end{aligned} \quad (6.9)$$

with the definition of the electrostatic potential $\Phi_{a,a'}(\mathbf{r})$ of molecule A, analog to (6.7). By inserting the same atomic charges approximation of the electrostatic potential of molecule A, as for the molecule of B, they derive the final form of the Coulomb coupling element in terms of atomic charges

$$V_{a',b'}^{a,b} = \frac{1}{4\pi\epsilon_0} \sum_{I,J} \frac{q_I(a,a') q_J(b,b')}{|\bar{\mathbf{R}}_I - \bar{\mathbf{R}}_J|} \quad (6.10)$$

In the strict sense this approach is only valid for the interaction between two molecules, but it can be generalized to periodic structures [CMW09, CSSJ10]

Now we start to use the formalism of atomic charges for our hybrid inorganic organic systems. Therefore, we calculate the coupling elements between the molecular layer and the semiconductor substrate. First, we need to transform the coupling element from real space into the reciprocal space. Second, we neglect the interaction between the molecules of the molecular layer in a first approach, similar to the case in [VKR⁺14]. Without this interaction, the matrix of the Eigenvectors $c_{\mathbf{1}\mathbf{1}}^{\mathbf{q}}$ is equal the identity matrix $\mathbb{1}$.

6.2 Band structure of the semiconductor

To describe the band structure of the semiconductor properly, we use the effective mass approximation [Czy04]. This approximation includes the momentum dependency of the conduction and valence band by using parabolic bands with a band gap E_{gap} . As commonly used, we use a positive mass for the conduction band ($m_c > 0$) and a negative one for the valence band ($m_v < 0$).

$$E_{\mathbf{k}\mathbf{k}'} = E_{gap} - \frac{\hbar^2 \mathbf{k}^2}{2m_v} + \frac{\hbar^2 \mathbf{k}'^2}{2m_c} \quad (6.11)$$

The effective masses as well as the gap energy are calculated by the Fritz-Haber-Institut Berlin by using an ab-intio framework [VKR⁺14].

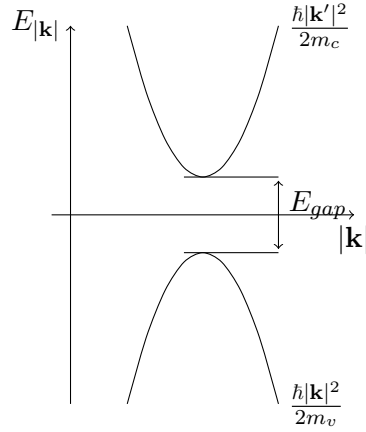


Figure 6.1 | Sketch of the band structure of the substrate using the effective mass approximation.

6.3 Hamilton Operator of the HIOS

The Hamiltonian of the HIOS is given by the free Hamiltonians of the molecular layer, the semiconductor substrate and the coupling between both constituents

$$\begin{aligned}
 H = & \underbrace{\sum_{\alpha, \mathbf{R}_\nu} E_\alpha a_{\alpha, \mathbf{R}_\nu}^\dagger a_{\alpha, \mathbf{R}_\nu}}_{\text{molecular layer}} + \underbrace{\sum_{\beta, \mathbf{k}} E_\beta^{\mathbf{k}} a_{\beta, \mathbf{k}}^\dagger a_{\beta, \mathbf{k}}}_{\text{semiconductor substrate}} \\
 & + \underbrace{\frac{e_0^2}{4\pi\epsilon_0} \sum_{\alpha, \alpha', \mathbf{R}_\nu} \sum_{\beta, \beta', \mathbf{k}, \mathbf{k}'} \left[V_{\beta', \mathbf{k}'}^{\beta, \mathbf{k}} a_{\beta, \mathbf{k}}^\dagger a_{\alpha, \mathbf{R}_\nu}^\dagger a_{\alpha', \mathbf{R}_\nu} a_{\beta', \mathbf{k}'} + \text{h.a.} \right]}_{\text{substrate-molecular layer interaction}} \quad (6.12)
 \end{aligned}$$

with the energies E of the excitons and the coupling matrix element $V_{\beta', \mathbf{k}'}^{\beta, \mathbf{k}} a_{\alpha, \mathbf{R}_\nu}^\dagger a_{\alpha', \mathbf{R}_\nu}$. α represents the states of the molecules (only HOMO and LUMO in the following), \mathbf{R}_ν the position of the ν -th molecule and β the band of the semiconductor (in the following only conduction c and valence band v). As commonly used, we describe the semiconductor substrate using a Bloch basis representation with the wave vector \mathbf{k} . For a consistent description of the molecular layer and the semiconductor substrate in one theory, we need to transform the Hamiltonian of the molecules to a Bloch basis, too. This is possible if we assume a regular and infinitely extended arrangement of molecules on top of the semiconductor substrate. We transform the electronic operators of the molecules using

$$a_{\alpha, \mathbf{R}_\nu} = \sum_{\mathbf{l}} \frac{1}{\sqrt{N_m}} e^{-i\mathbf{l} \cdot \mathbf{R}_\nu} a_{\alpha, \mathbf{l}} \quad \text{and} \quad a_{\alpha, \mathbf{l}} = \sum_{\mathbf{R}_\nu} \frac{1}{\sqrt{N_m}} e^{i\mathbf{l} \cdot \mathbf{R}_\nu} a_{\alpha, \mathbf{R}_\nu} \quad (6.13)$$

, respectively. The reciprocal space vectors \mathbf{l} and \mathbf{k} are restricted to the first Brillouin zone of the molecular layer and substrate, and $N_m(N_{uc})$ is the number of molecules and unit cells, respectively. The Hamiltonian in Bloch basis

$$H = \sum_{\mathbf{l}} \sum_{\alpha \in \{H,L\}} E_{\alpha}^{\dagger} a_{\alpha,\mathbf{l}} + \sum_{\mathbf{k}} \sum_{\beta \in \{v,c\}} E_{\mathbf{k}} a_{\mathbf{k}}^{\dagger} a_{\mathbf{k}} + \frac{e_0^2}{4\pi\epsilon_0} \frac{1}{N_m N_{uc}} \sum_{\mathbf{l}\mathbf{l}'} \sum_{\mathbf{k}\mathbf{k}'} \sum_{\mathbf{R}_{\nu}} \left[V_{v,\mathbf{k}'}^{c,\mathbf{k} H, \mathbf{R}_{\nu}} e^{i(\mathbf{k}-\mathbf{k}')\mathbf{R}_{\nu}} a_{c,\mathbf{k}}^{\dagger} a_{H,\mathbf{l}}^{\dagger} a_{L,\mathbf{l}'} a_{v,\mathbf{k}'} + \text{h.a.} \right] \quad (6.14)$$

now treats the electrons of the semiconductor substrate as well as the electrons of the molecular layer in the same manner.

We employ some calculation on the coupling element

$$V_{v,\mathbf{k}'}^{c,\mathbf{k} H, \mathbf{R}_{\nu}} = \frac{1}{N_m N_{uc}} \sum_{\mathbf{R}_{\nu}} V_{v,\mathbf{k}'}^{c,\mathbf{k} H, \mathbf{R}_{\nu}} e^{i(\mathbf{k}-\mathbf{k}')\mathbf{R}_{\nu}} \quad (6.15)$$

to reduce the numerical costs.

We express the coupling element via atomic charges using Equation (6.10):

$$V_{v,\mathbf{k}'}^{c,\mathbf{k} H, \mathbf{R}_{\nu}} = \sum_{I_{uc}, J_{\nu}} \frac{q_{I_{uc}}(c, v) q_{J_{\nu}}(H, L)}{|\mathbf{R}_{\nu} + \mathbf{R}_{J_{\nu}} - \mathbf{R}_{uc} - \mathbf{R}_{I_{uc}}|} \quad (6.16)$$

Here, we divided the vector pointing to the atomic charges in one vector pointing to the unit cell of the semiconductor substrate/molecular layer ($\mathbf{R}_{uc}/\mathbf{R}_{\nu}$) and one vector pointing from the origin of the unit cell to the position of the atomic charge of the substrate/ molecular layer ($\mathbf{R}_{I_{uc}}/\mathbf{R}_{J_{\nu}}$). The charges $q_{I_{uc}}$ labels the I -th atomic charge in the unit cell of the substrate and the charges $q_{J_{\nu}}$ to the J -th atomic charge in the unit cell at \mathbf{R}_{ν} of the molecular layer, respectively.

Since the sum over \mathbf{R}_{uc} is infinite and $\mathbf{R}_{uc} * n = \mathbf{R}_{\nu}$ for $n \in \mathbb{Z}$ holds (we assume only whole-number ratios of the coverage), we can make the replacement $\mathbf{R}_{uc} \rightarrow \mathbf{R}_{uc} + \mathbf{R}_{\nu}$. With this replacement, the sum over the atomic charges is independent of \mathbf{R}_{ν} and we can apply the discrete Fourier transformation

$$\sum_{\mathbf{R}_{\nu}} \frac{1}{N_m} e^{i(\mathbf{k}-\mathbf{k}'+1-\mathbf{l}')\mathbf{R}_{\nu}} = \sum_{\mathbf{G}_{\nu}} \delta_{\mathbf{k}-\mathbf{k}'+1-\mathbf{l}', \mathbf{G}_{\nu}} \quad (6.17)$$

with the reciprocal unit cell vector of the molecular layer \mathbf{G}_{ν} .

$$\begin{aligned} & \frac{e_0^2}{4\pi\epsilon_0} \frac{1}{N_m N_{uc}} \sum_{\mathbf{R}_{\nu}} V_{v,\mathbf{R}_{uc}}^{c,\mathbf{R}_{uc} H, \mathbf{R}_{\nu}} e^{i(1-\mathbf{l}')\mathbf{R}_{\nu}} \\ &= \frac{1}{4\pi\epsilon_0} \frac{1}{N_{uc}} \sum_{\mathbf{G}_{\nu}} \delta_{\mathbf{k}-\mathbf{k}'+1-\mathbf{l}', \mathbf{G}_{\nu}} \sum_{I_{uc}, J_{\nu}} \frac{q_{I_{uc}} q_{J_{\nu}}}{|\mathbf{R}_{J_{\nu}} - \mathbf{R}_{uc} - \mathbf{R}_{I_{uc}}|} \\ &\equiv V_{\mathbf{k}', v}^{\mathbf{k}, c, \mathbf{l}', H} \end{aligned} \quad (6.18)$$

This yields for the interaction Hamiltonian between the semiconductor substrate and the molecular layer:

$$H_{sub-mol} = \sum_{\mathbf{l}\mathbf{l}'} \sum_{\mathbf{k}\mathbf{k}'} V_{\mathbf{k}', v}^{\mathbf{k}, c, \mathbf{l}', H} a_{c,\mathbf{k}}^{\dagger} a_{H,\mathbf{l}}^{\dagger} a_{L,\mathbf{l}'} a_{v,\mathbf{k}'} + \text{h.a.} \quad (6.19)$$

6.4 Equation of motion for the HIOS

After calculating the desired Hamiltonians for the hybrid inorganic organic system, we calculate the equations of motions via the Von-Neumann-Equation to obtain the dynamics of the system

$$\partial_t \langle O | \rho | O \rangle = -\frac{\hbar}{\hbar} \langle O | [H, \rho] | O \rangle \quad (6.20)$$

for a given state O and the density matrix ρ . We find for the exciton density in the molecular layer

$$\partial_t \langle X_{\mathbf{q}} | \rho | X_{\mathbf{q}} \rangle = -\frac{2}{\hbar} \sum_{\mathbf{k}\mathbf{k}'} \Im \left[V_{\mathbf{k}',v L}^{\mathbf{k},c H} \langle X_{\mathbf{q}} | \rho | \mathbf{k}'\mathbf{k} \rangle \right] \quad (6.21)$$

where we use the definition of the state $|X_{\mathbf{q}}\rangle = \sum_{l_1, l_2} c_{l_1, l_2}^{\mathbf{q}} |l_1 l_2\rangle$ and define the matrix element $V_{\mathbf{k}',v L}^{\mathbf{k},c H}$ as

$$V_{\mathbf{k}',v L}^{\mathbf{k},c H} = \sum_{l, l'} c_{ll'}^{\mathbf{q}} V_{\mathbf{k}',v l', L}^{\mathbf{k},c l, H}. \quad (6.22)$$

To calculate the exciton density in the semiconductor substrate, we use the completeness relation of the coefficients $\sum_{\mathbf{q}} c_{l_1 l_2}^{\mathbf{q}*} c_{l_1' l_2'}^{\mathbf{q}} = \delta_{l_1, l_1'} \delta_{l_2, l_2'}$ and end up with

$$\partial_t \langle \mathbf{k}\mathbf{k}' | \rho | \mathbf{k}'\mathbf{k} \rangle = -\frac{2}{\hbar} \sum_{\mathbf{q}} \Im \left[V_{\mathbf{k}',v L}^{\mathbf{k},c H} \langle X_{\mathbf{q}} | \rho | \mathbf{k}'\mathbf{k} \rangle \right]. \quad (6.23)$$

The polarization like term $\langle X_{\mathbf{q}} | \rho | \mathbf{k}'\mathbf{k} \rangle$ is calculated with the use of the above mentioned relations and we only consider the diagonal elements $\langle \mathbf{k}\mathbf{k}' | \rho | \mathbf{k}'\mathbf{k} \rangle$.

$$\begin{aligned} \partial_t \langle X_{\mathbf{q}} | \rho | \mathbf{k}'\mathbf{k} \rangle &= \frac{\hbar}{\hbar} (E_{\mathbf{k}\mathbf{k}'} - E_{\mathbf{q}}) \langle X_{\mathbf{q}} | \rho | \mathbf{k}'\mathbf{k} \rangle \\ &\quad - \frac{\hbar}{\hbar} \left[V_{\mathbf{k}',v L}^{\mathbf{k},c H} \langle \mathbf{k}\mathbf{k}' | \rho | \mathbf{k}'\mathbf{k} \rangle - \left(V_{\mathbf{k}',v L}^{\mathbf{k},c H} \right)^* \langle X_{\mathbf{q}} | \rho | X_{\mathbf{q}} \rangle \right] \end{aligned} \quad (6.24)$$

We solve this equation by using the Markov approximation and later insert the solution into the exciton densities of the semiconductor substrate and the molecular layer, respectively.

First, we solve the inhomogeneous ordinary differential equation for the polarization term $\langle X_{\mathbf{q}} | \rho | \mathbf{k}'\mathbf{k} \rangle$ with constant coefficients of first order by variation of parameters. To obtain convergence, we introduce a factor $\hbar\gamma$ (this is equivalent to include damping phenomenologically). Formal integration of (6.24) and the substitution $t' = t - s$ yields:

$$\begin{aligned}
\langle X_{\mathbf{q}}|\rho|\mathbf{k}'\mathbf{k}\rangle(t) &= -\frac{\dot{\hbar}}{\hbar} \int_{-\infty}^t dt' e^{\frac{\dot{\hbar}}{\hbar}(E_{\mathbf{k}\mathbf{k}'}-E_{\mathbf{q}}+\dot{\hbar}\gamma)(t-t')} \\
&\quad \times \left[V_{\mathbf{k}',vL}^{\mathbf{k},cH} \langle \mathbf{k}\mathbf{k}'|\rho|\mathbf{k}'\mathbf{k}\rangle(t') - \left(V_{\mathbf{k}',vL}^{\mathbf{k},cH} \right)^* \langle X_{\mathbf{q}}|\rho|X_{\mathbf{q}}\rangle(t') \right] \\
&= -\frac{\dot{\hbar}}{\hbar} \int_0^{\infty} ds e^{\frac{\dot{\hbar}}{\hbar}(E_{\mathbf{k}\mathbf{k}'}-E_{\mathbf{q}}+\dot{\hbar}\gamma)(s)} \\
&\quad \times \left[V_{\mathbf{k}',vL}^{\mathbf{k},cH} \langle \mathbf{k}\mathbf{k}'|\rho|\mathbf{k}'\mathbf{k}\rangle(t-s) - \left(V_{\mathbf{k}',vL}^{\mathbf{k},cH} \right)^* \langle X_{\mathbf{q}}|\rho|X_{\mathbf{q}}\rangle(t-s) \right]
\end{aligned} \tag{6.25}$$

The Markov approximation neglects the s dependency of the densities $\langle \mathbf{k}\mathbf{k}'|\rho|\mathbf{k}'\mathbf{k}\rangle$ and $\langle X_{\mathbf{q}}|\rho|X_{\mathbf{q}}\rangle$. This is the same as to neglect memory effects, since the integration over $t-s$ integrates over all times before t . From a more mathematical point of view one can argue, that the Markov approximation is valid as long as the exponential function oscillates much faster than the function with time argument $t-s$. If this is the case, we can neglect the s dependency and take the terms out of the integral.

In our case we neglect the parameter s in the densities for the substrate and molecular layer excitation, respectively. These quantities vary way slower than i.e. the polarizations between the substrate and the molecular layer ($\langle X_{\mathbf{q}}|\rho|\mathbf{k}'\mathbf{k}\rangle$) as long as the energy gap $|E_{\mathbf{k}\mathbf{k}'} - E_{\mathbf{q}}|$ is way larger than the coupling between the excitons in the semiconductor substrate and the excitons in the molecular layer $V_{\mathbf{k}',vL}^{\mathbf{k},cH}$.

Integration of the e -function and use of Dirac's identity [HK09] yields

$$\frac{\dot{\hbar}}{E_{\mathbf{k}\mathbf{k}'} - E_{\mathbf{q}} + \dot{\hbar}\gamma} = P \left(\frac{\hbar}{E_{\mathbf{k}\mathbf{k}'} - E_{\mathbf{q}}} \right) + \pi\hbar\delta(E_{\mathbf{k}\mathbf{k}'} - E_{\mathbf{q}}). \tag{6.26}$$

In the following, we neglect the principle value P and find the solution for the polarization

$$\langle X_{\mathbf{q}}|\rho|\mathbf{k}'\mathbf{k}\rangle = \hbar\pi\delta(E_{\mathbf{k}\mathbf{k}'} - E_{\mathbf{q}}) \left[V_{\mathbf{k}',vL}^{\mathbf{k},cH} \langle \mathbf{k}\mathbf{k}'|\rho|\mathbf{k}'\mathbf{k}\rangle - \left(V_{\mathbf{k}',vL}^{\mathbf{k},cH} \right)^* \langle X_{\mathbf{q}}|\rho|X_{\mathbf{q}}\rangle \right] \tag{6.27}$$

with the energy conserving delta function $\delta(E_{\mathbf{k}\mathbf{k}'} - E_{\mathbf{q}})$. In order to calculate the energy transfer rate between the semiconductor substrate and the molecular layer, we will eliminate the polarization in the equations of motions of the densities.

6.5 Transfer rates

Now we calculate the energy transfer between a molecular layer and a semiconductor substrate by using spatial charges for the unit cells of both constituents in real space. Using different Fermi-Dirac distributions for the electrons and holes in the semiconductor substrate accounts for electrical pumping of the substrate.

We use the previous results from Section 6.4, i.e. the solution for the polarization obtained via Markov approximation, and insert this solution (6.27) into the equation of motion of the densities for the molecular layer (6.21) and the semiconductor substrate (6.23).

$$\begin{aligned} \partial_t \langle X_{\mathbf{q}} | \rho | X_{\mathbf{q}} \rangle &= \frac{2\pi}{\hbar} \sum_{\mathbf{k}, \mathbf{k}', \mathbf{q}} \left| V_{\mathbf{k}', v L}^{\mathbf{k}, c H} \right|^2 \langle X_{\mathbf{q}} | \rho | X_{\mathbf{q}} \rangle \delta(E_{\mathbf{k}\mathbf{k}'} - E_{\mathbf{q}}) \\ &\quad - \frac{2\pi}{\hbar} \sum_{\mathbf{k}, \mathbf{k}'} \left| V_{\mathbf{k}', v L}^{\mathbf{k}, c H} \right|^2 \langle \mathbf{k}\mathbf{k}' | \rho | \mathbf{k}'\mathbf{k} \rangle \delta(E_{\mathbf{k}\mathbf{k}'} - E_{\mathbf{q}}) \end{aligned} \quad (6.28)$$

$$\begin{aligned} \partial_t \langle \mathbf{k}\mathbf{k}' | \rho | \mathbf{k}'\mathbf{k} \rangle &= \frac{2\pi}{\hbar} \sum_{\mathbf{q}} \left| V_{\mathbf{k}', v L}^{\mathbf{k}, c H} \right|^2 \langle X_{\mathbf{q}} | \rho | X_{\mathbf{q}} \rangle \delta(E_{\mathbf{k}\mathbf{k}'} - E_{\mathbf{q}}) \\ &\quad - \frac{2\pi}{\hbar} \sum_{\mathbf{k}\mathbf{k}'\mathbf{q}} \left| V_{\mathbf{k}', v L}^{\mathbf{k}, c H} \right|^2 \langle \mathbf{k}\mathbf{k}' | \rho | \mathbf{k}'\mathbf{k} \rangle \delta(E_{\mathbf{k}\mathbf{k}'} - E_{\mathbf{q}}) \end{aligned} \quad (6.29)$$

Assuming an electrically pumped semiconductor, we identify the term

$$\Gamma = -\frac{2\pi}{\hbar} \sum_{\mathbf{k}, \mathbf{k}'} \left| V_{\mathbf{k}', v L}^{\mathbf{k}, c H} \right|^2 \langle \mathbf{k}\mathbf{k}' | \rho | \mathbf{k}'\mathbf{k} \rangle \delta(E_{\mathbf{k}\mathbf{k}'} - E_{\mathbf{q}}) \quad (6.30)$$

as energy transfer rate between both constituents of the HIOS. We further simplify this energy rate by evaluating the delta functions caused by the Markov approximation. We start by rewriting the k-sums as integrals, suitable for quasi discrete systems,

$$\sum_{\mathbf{k}} = \sum_{\mathbf{k}} \frac{(\Delta\mathbf{k})^D}{(\Delta\mathbf{k})^D} \rightarrow \left(\frac{L}{2\pi} \right)^D \int d\mathbf{k}^D \quad (6.31)$$

with the size in real space L and the dimension D [HK09].

We use the property of the delta function:

$$\int dx f(x) \delta(g(x)) = \sum_{n_i} \int dx f(x) \frac{\delta(x - n_i)}{|g'(n_i)|} = \sum_{n_i} \frac{f(n_i)}{|g'(n_i)|} \quad (6.32)$$

with the sum over the zeros of $g(x)$ n_i . The delta distribution is fulfilled for $E_{\mathbf{k}\mathbf{k}'} = E_{\mathbf{q}}$ which leads, in Cartesian coordinates and solved for k_{x_i} , to

$$k_{x_i} = \sqrt{-k_y^2 + \mathbf{k}'^2 \frac{m_v}{m_c} + 2 \frac{m_v}{\hbar^2} (E_{gap} - E_{\mathbf{q}})} \quad (6.33)$$

with the gap energy of the semiconductor E_{gap} and the transition energy of the molecular layer $E_{\mathbf{q}}$ (cf. 6.2), which can depend on the momentum vector \mathbf{q} . Note, we neglect the negative solution of the square root, since negative k-vectors are senseless in reciprocal space.

Evaluating the delta function using the above mentioned relations, we find for the energy transfer rate

$$\Gamma = \frac{2\pi m_v}{\hbar^4 N_m^2} \int dk_y \int d\mathbf{k}' \left| V_{\mathbf{k}', v}^{k_{x_i}, k_y, c H} \right|^2 \langle \mathbf{k}'\mathbf{k} | \rho | \mathbf{k}\mathbf{k}' \rangle \frac{1}{k_{x_i}} \quad (6.34)$$

To account for electrical pumping of the semiconductor substrate, we approximate the exciton density in the semiconductor substrate $\langle \mathbf{k}\mathbf{k}' | \rho | \mathbf{k}'\mathbf{k} \rangle$ by two Fermidistributions, one for the electrons f_e and one for the holes f_h

$$f = \frac{1}{e^{\frac{E - \mu}{k_B T}} + 1} \quad (6.35)$$

Since the numerical calculations scaled with the discretization of the \mathbf{l} and \mathbf{k} wave vectors, we regard numerical solutions for the energy transfer rate to further investigations.

In conclusion, we introduce spatial charges to describe the interaction between the semiconductor substrate and the molecular layer beyond the dipole approximation. We derive the equations of motions for the coupled hybrid system and apply the Markov approximation to the polarization between the semiconductor substrate and the molecular layer. Therefore, we are able to formulate the energy transfer rate between molecules and the semiconductor substrate. Understanding the basic mechanism of energy transfer in the system is crucial to design and optimize hybrid organic inorganic systems, since the transfer rate depends on the molecular coverage and distance.

Part V

Epilogue

Chapter 7

Conclusion and Outlook

We investigate a hybrid system consisting of two quantum dots coupled to a metal sphere. For such a device, we theoretically propose a tunable emission statistic by only changing one system parameter, the Förster interaction between the two quantum dots. We explain the huge impact of this interaction on the emission statistic via redistribution of dipole-moments and shifts in the eigenenergies of the coupled hybrid system.

For one quantum dot coupled to a metal sphere, we compare our theory with experimental results and find good qualitative agreement in time and frequency domain. For small metal spheres and a large distance between the constituents, the quantitative agreement is pretty striking, too. The quantitative mismatch might be related to higher order plasmon modes which are not included in our theory. Including these modes could open paths to the rich variety of plasmonic physics. For instance, the quadrupole mode usually does not couple to the far-field and is thus not effected by radiative decay. This could be an useful feature if one would use it as a resonator for a spaser. Beside higher order modes of metal spheres, one could also change the shape of the metal structure to achieve certain properties. This could include guiding of plasmons or focusing of electric fields. While these features are often included in classical calculations based on Maxwell's equations, there are no quantum mechanical calculations dealing with all these features. The quantization of plasmons within irregular shaped metal structures or of higher order modes is an interesting and challenging field for theoretical physicists.

In the last part, we derive the energy transfer rate between a semiconductor quantum well and a molecular layer. These systems are promising candidates for high efficient light sources and have been recently reported experimentally [SBB⁺15]. Nevertheless, a fundamental theoretical understanding is crucial for an efficient development and improvement of such optical devices. Beside the interaction between the molecular layer and the semiconductor quantum well, one could additionally include disorder within the molecular layer and the interaction between the molecules in the molecular layer for a more realistic model of the system.

Danksagung

Zuerst möchte ich Professor Andreas Knorr für seine unermüdliche Unterstützung und Betreuung danken, dadurch wurde diese Arbeit erst möglich. Die Arbeit in der Arbeitsgruppe war sehr inspirierend und es herrschte stets ein sehr angenehmes Arbeitsklima. Ich danke ihm ferner für zahlreiche und hilfreiche Anmerkungen in den unterschiedlichsten Bereichen. Zu guter Letzt danke ich ihm für die Erstellung des Gutachtens zu dieser Arbeit.

Dr. Heiko Appel und Dr. Marten Richter danke ich für die Erstellung der weiteren Gutachten. Professor Thomas Möller danke ich, dass er sich bereit erklärt hat den Vorsitz des Promotionsausschusses zu übernehmen.

Im Besonderen möchte ich Dr. Marten Richter danken, da er maßgeblich mit an der Betreuung dieser Arbeit beteiligt war. Seine Ideen und sein physikalisches Verständnis waren immer sehr hilfreich.

Sandra Kuhn, Judith Specht und Anke Zimmermann gebührt mein Dank für das Korrekturlesen dieser Arbeit. All meinen ehemaligen und aktuellen Büronachbarn danke ich für die ein oder andere Alberei.

Last but not least möchte ich meiner Familie für Ihre Unterstützung während des Studiums und der Promotion danken.

Appendices

Appendix A

Parameter for fit of the dielectric function

The following table gives an overview over the parameters obtained by fitting the function [ELRM06]

$$\varepsilon_{Au} = \varepsilon_{\infty} - \frac{1}{\lambda_p^2 \left(\frac{1}{\lambda^2} + \frac{i}{\gamma_p \lambda} \right)} + \sum_{i=1,2} \frac{A_i}{\lambda_i} \left[\frac{e^{i\phi_i}}{\frac{1}{\lambda_i} - \frac{1}{\lambda} - \frac{i}{\gamma_i}} + \frac{e^{-i\phi_i}}{\frac{1}{\lambda_i} + \frac{1}{\lambda} + \frac{i}{\gamma_i}} \right] \quad (\text{A.1})$$

to the dielectric function measured by Johnson and Christy [JC72] for gold Table A.1 and silver A.2

variable	fit value	variable	fit value	variable	fit value	variable	fit value
ω_{pl}	10.3392	Γ_{pl}	0.24668508	A_1	2.66641	A_2	243.705
ω_1	2.38613	ω_2	0.278584	Φ_1	-1.33841	Φ_2	-3.09254
γ_1	0.906995	γ_2	0.30894	ε_{∞}	0.920894		

Table A.1 | Fit parameter for gold.

variable	fit value	variable	fit value	variable	fit value	variable	fit value
ω_{pl}	9.12988	Γ_{pl}	0.0218872	A_1	4.64428	A_2	0.401092
ω_1	2.16392	ω_2	4.01371	Φ_1	-1.97191	Φ_2	-1.65356
γ_1	2.98446	γ_2	0.504812	ε_{∞}	0.0080116		

Table A.2 | Fit parameter for silver.

Appendix B

Equations of motion for the hybrid system

B.1 One quantum dot coupled to a metal sphere

For sake of completeness, we give the equation of motion for the plasmon assisted conduction band density for a hybrid system consisting of one quantum dot coupled to a metal sphere. The equation reads:

$$\begin{aligned}
\partial_t \langle n_c | n \rangle \langle p | \rangle &= \left(\dot{\mathbf{i}}(n-p)\omega_{sp} - \frac{\gamma_{sp}}{2}(p+n) - \gamma_g \right) \langle n_c | n \rangle \langle p | \rangle \\
&+ \gamma_{sp} \sqrt{p+1} \sqrt{n+1} \langle n_c | n+1 \rangle \langle p+1 | \rangle \\
&- \frac{\dot{\mathbf{i}}}{\hbar} \mu (E(t)^* \langle \rho_{vc} | n \rangle \langle p | \rangle - E(t) \langle \rho_{vc} | p \rangle \langle n | \rangle) \\
&+ \frac{\dot{\mathbf{i}}}{\hbar} \chi E(t) \sqrt{p} \langle n_c | n \rangle \langle p-1 | \rangle - \frac{\dot{\mathbf{i}}}{\hbar} \chi^* E(t)^* \sqrt{n} \langle n_c | n-1 \rangle \langle p | \rangle \\
&+ \frac{\dot{\mathbf{i}}}{\hbar} \chi^* E(t)^* \sqrt{p+1} \langle n_c | n \rangle \langle p+1 | \rangle - \frac{\dot{\mathbf{i}}}{\hbar} \chi E(t) \sqrt{n+1} \langle n_c | n+1 \rangle \langle p | \rangle \\
&- \dot{\mathbf{i}} g_1 \sqrt{n+1} \langle \rho_{vc} | n+1 \rangle \langle p | \rangle + \dot{\mathbf{i}} g_1^* \sqrt{p+1} \langle \rho_{vc} | p+1 \rangle \langle n | \rangle .
\end{aligned} \tag{B.1}$$

Plasmonic oscillations ω_{sp} and damping γ_{sp} occur in the first and second line since the conduction band density is plasmon assisted by the plasmonic eigenstates $|n\rangle\langle p|$. The third line couples the conduction band density via the external optical field $E(t)$ to the excitonic polarization. The fourth and fifth line account for the interaction between the plasmons and the external optical field. In the last line the interaction between the excitons and the plasmons is included.

B.2 Two quantum dot coupled to a metal sphere

For the sake of completeness we give the equation of motion for the ρ_{ijkl} terms. Here for the case of two quantum dots coupled to a metal sphere in the biexcitonic basis including F\~{A}Prster interaction between the quantum dots.

$$\begin{aligned}
 \partial_t \rho_{vvvv}^{n,m} = & \left(\dot{\mathbf{i}}(n-m)\omega_{sp} - \frac{\gamma_{sp}}{2}(n+m) \right) \rho_{vvvv}^{n,m} + \gamma_{sp}\sqrt{n+1}\sqrt{m+1}\rho_{vvvv}^{n+1,m+1} \\
 & + \gamma_g(\rho_{cvvc}^{n,m} + \rho_{vccv}^{n,m}) + \dot{\mathbf{i}}\frac{\mu_1}{\hbar}(E_t^* \rho_{vvvc}^{n,m} - E_t \rho_{vvvc}^{m,n*}) + \dot{\mathbf{i}}\frac{\mu_2}{\hbar}(E_t^* \rho_{vvcv}^{n,m} - E_t \rho_{vvcv}^{m,n*}) \\
 & + \frac{\dot{\mathbf{i}}}{\hbar}E_t^* \chi^* (\sqrt{m+1}\rho_{vvvv}^{n,m+1} - \sqrt{n}\rho_{vvvv}^{n-1,m}) + \frac{\dot{\mathbf{i}}}{\hbar}E_t \chi (\sqrt{m}\rho_{vvvv}^{n,m-1} - \sqrt{n+1}\rho_{vvvv}^{n+1,m}) \\
 & + \dot{\mathbf{i}}\sqrt{m}\frac{g_1}{\hbar}\rho_{vvvc}^{n,m-1} - \dot{\mathbf{i}}\sqrt{n}\frac{g_1^*}{\hbar}\rho_{vvvc}^{m,n-1*} + \dot{\mathbf{i}}\sqrt{m}\frac{g_2}{\hbar}\rho_{vvcv}^{n,m-1} - \dot{\mathbf{i}}\sqrt{n}\frac{g_2^*}{\hbar}\rho_{vvcv}^{m,n-1*}
 \end{aligned} \tag{B.2}$$

The density like term $\rho_{vvvv}^{n,m}$ representing the electron ground state correlation has no decay term but is driven by in scattering terms from upper excitonic levels through $\rho_{cvvc}^{n,m}$ and $\rho_{vccv}^{n,m}$ which ensure energy relaxations in the system. The interaction between plasmons and external optical field couples $\rho_{vvvv}^{n,m}$ to other plasmon number states. The plasmon excitation and absorption terms appear at all quantities $\rho_{opqr}^{n,m}$ with $o, p, q, r \in c, v$ (c: conduction, v: valence band).

$$\begin{aligned}
 \partial_t \rho_{cvcv}^{n,m} = & (\dot{\mathbf{i}}(n-m)\omega_{sp} + \dot{\mathbf{i}}(\omega_{\frac{g_1}{\hbar}} - \omega_{\frac{g_2}{\hbar}}) - \frac{\gamma_{sp}}{2}(n+m) - \gamma_g)\rho_{cvcv}^{n,m} + \gamma_{sp}\sqrt{n+1}\sqrt{m+1}\rho_{cvcv}^{n+1,m+1} \\
 & - \dot{\mathbf{i}}\frac{\mu_1}{\hbar}E_t^*(\rho_{vvvc}^{n,m} - \rho_{cvcv}^{m,n*}) - \dot{\mathbf{i}}\frac{\mu_2}{\hbar}E_t(\rho_{cvcv}^{n,m} - \rho_{vvvc}^{m,n*}) + \dot{\mathbf{i}}\frac{V_{12}}{\hbar}(\rho_{vccv}^{n,m} - \rho_{cvcv}^{n,m}) \\
 & + \frac{\dot{\mathbf{i}}}{\hbar}E_t^* \chi^* (\sqrt{m+1}\rho_{cvcv}^{n,m+1} - \sqrt{n}\rho_{cvcv}^{n-1,m}) + \frac{\dot{\mathbf{i}}}{\hbar}E_t \chi (\sqrt{m}\rho_{cvcv}^{n,m-1} - \sqrt{n+1}\rho_{cvcv}^{n+1,m}) \\
 & + \dot{\mathbf{i}}\frac{g_1}{\hbar}\sqrt{m}\rho_{cvcv}^{m-1,n*} - \dot{\mathbf{i}}\frac{g_1}{\hbar}\sqrt{n+1}\rho_{cvcv}^{n+1,m} + \dot{\mathbf{i}}\frac{g_2^*}{\hbar}\sqrt{m+1}\rho_{vvvc}^{m+1,n*} - \dot{\mathbf{i}}\frac{g_2^*}{\hbar}\sqrt{n}\rho_{cvcv}^{n-1,m}
 \end{aligned} \tag{B.3}$$

$\rho_{cvcv}^{n,m}$ is a pure polarization operator for quantum dot 1 and quantum dot 2. Therefore, it is damped by γ_g ($\gamma_g/2$ for each transition). On the one hand, the Förster interaction couples $\rho_{cvcv}^{n,m}$ to pure density like expectation values $\rho_{vccv}^{n,m}$ and $\rho_{cvvc}^{n,m}$. On the other hand, the interaction with the external optical field and the interaction between the excitons and plasmons $g_{1/2}$ couple $\rho_{cvcv}^{n,m}$ to excitonic polarization and density like expectation values.

$$\begin{aligned}
 \partial_t \rho_{cccv}^{n,m} = & (\dot{\mathbf{i}}(n-m)\omega_{sp} + \dot{\mathbf{i}}\omega_{\frac{g_1}{\hbar}} - \frac{\gamma_{sp}}{2}(n+m) - 3/2\gamma_g)\rho_{cccv}^{n,m} + \gamma_{sp}\sqrt{n+1}\sqrt{m+1}\rho_{cccv}^{n+1,m+1} \\
 & - \dot{\mathbf{i}}\frac{\mu_1}{\hbar}E_t^*(\rho_{vccv}^{n,m} - \rho_{cccv}^{n,m}) - \dot{\mathbf{i}}\frac{\mu_2}{\hbar}(-E_t \rho_{cccv}^{n,m} + E_t^* \rho_{cvcv}^{n,m}) - \dot{\mathbf{i}}\frac{V_{12}}{\hbar}\rho_{cccv}^{n,m} \\
 & + \frac{\dot{\mathbf{i}}}{\hbar}E_t^* \chi^* (\sqrt{m+1}\rho_{cccv}^{n,m+1} - \sqrt{n}\rho_{cccv}^{n-1,m}) + \frac{\dot{\mathbf{i}}}{\hbar}E_t \chi (\sqrt{m}\rho_{cccv}^{n,m-1} - \sqrt{n+1}\rho_{cccv}^{n+1,m}) \\
 & - \dot{\mathbf{i}}\frac{g_1}{\hbar}\sqrt{n+1}\rho_{vccv}^{n+1,m} + \dot{\mathbf{i}}\frac{g_1}{\hbar}\sqrt{m}\rho_{cccv}^{n,m-1} - \dot{\mathbf{i}}\frac{g_2}{\hbar}\sqrt{n+1}\rho_{cvcv}^{n+1,m} + \dot{\mathbf{i}}\frac{g_2^*}{\hbar}\sqrt{m+1}\rho_{cccv}^{n,m+1}
 \end{aligned} \tag{B.4}$$

$\rho_{cccv}^{n,m}$ is a mixed operator, density like for quantum dot 2 and polarization like for quantum dot 1, thus damped by $3/2\gamma_g$ ($\gamma_g/2$ for the transition and γ_g for the density). Via the conduction band density like contribution in $\rho_{cccv}^{n,m}$ it drives the valence band density term in $\rho_{vvvc}^{n,m}$ (cf. Eq. (B.6)). The Förster interaction couples the density like part of $\rho_{cccv}^{n,m}$ to a polarization like part and vice versa the polarization like part to a density like part, this contributes to the formation of plasmon polariton excitations.

$$\begin{aligned}
 \partial_t \rho_{ccvc}^{n,m} = & (\dot{\mathbf{i}}(n-m)\omega_{sp} + \dot{\mathbf{i}}\omega \frac{g_2}{\hbar} - \frac{\gamma_{sp}}{2}(n+m) - 3/2\gamma_g)\rho_{ccvc}^{n,m} + \gamma_{sp}\sqrt{n+1}\sqrt{m+1}\rho_{ccvc}^{n+1,m+1} \\
 & - \dot{\mathbf{i}}\frac{\mu_1}{\hbar}(E_t^* \rho_{ccvc}^{m,n*} - E_t \rho_{ccvc}^{n,m}) - \dot{\mathbf{i}}\frac{\mu_2}{\hbar}E_t^*(\rho_{ccvc}^{n,m} - \rho_{cccc}^{n,m}) - \dot{\mathbf{i}}\frac{V_{12}}{\hbar}\rho_{ccvc}^{n,m} \\
 & + \frac{\dot{\mathbf{i}}}{\hbar}E_t^* \chi^* (\sqrt{m+1}\rho_{ccvc}^{n,m+1} - \sqrt{n}\rho_{ccvc}^{n-1,m}) + \frac{\dot{\mathbf{i}}}{\hbar}E_t \chi (\sqrt{m}\rho_{ccvc}^{n,m-1} - \sqrt{n+1}\rho_{ccvc}^{n+1,m}) \\
 & - \dot{\mathbf{i}}\sqrt{n+1} \left(\frac{g_1}{\hbar}\rho_{ccvc}^{m,n+1*} + \frac{g_2}{\hbar}\rho_{ccvc}^{n+1,m} \right) + \dot{\mathbf{i}}\frac{g_1^*}{\hbar}\sqrt{m+1}\rho_{ccvc}^{n,m+1} + \dot{\mathbf{i}}\frac{g_2}{\hbar}\sqrt{m}\rho_{cccc}^{n,m-1}
 \end{aligned} \tag{B.5}$$

$\rho_{ccvc}^{n,m}$ is similar to the last term. But in contrast to $\rho_{cccc}^{n,m}$ the contributions of quantum dot 1 and quantum dot 2 are swapped.

$$\begin{aligned}
 \partial_t \rho_{vvvc}^{n,m} = & (\dot{\mathbf{i}}(n-m)\omega_{sp} - \dot{\mathbf{i}}\omega \frac{g_1}{\hbar} - \frac{\gamma_{sp}}{2}(n+m) - 1/2\gamma_g)\rho_{vvvc}^{n,m} + \gamma_{sp}\sqrt{n+1}\sqrt{m+1}\rho_{vvvc}^{n+1,m+1} \\
 & + \gamma_g \rho_{cccc}^{m,n*} - \dot{\mathbf{i}}\frac{\mu_1}{\hbar}E_t(\rho_{ccvc}^{n,m} - \rho_{vvvc}^{n,m}) + \dot{\mathbf{i}}\frac{\mu_2}{\hbar}(E_t^* \rho_{ccvc}^{m,n*} - E_t \rho_{ccvc}^{m,n*}) - \dot{\mathbf{i}}\frac{V_{12}}{\hbar}\rho_{vvvc}^{n,m} \\
 & + \frac{\dot{\mathbf{i}}}{\hbar}E_t^* \chi^* (\sqrt{m+1}\rho_{vvvc}^{n,m+1} - \sqrt{n}\rho_{vvvc}^{n-1,m}) + \frac{\dot{\mathbf{i}}}{\hbar}E_t \chi (\sqrt{m}\rho_{vvvc}^{n,m-1} - \sqrt{n+1}\rho_{vvvc}^{n+1,m}) \\
 & + \dot{\mathbf{i}}\frac{g_2}{\hbar}\sqrt{m}\rho_{ccvc}^{m-1,n*} - \dot{\mathbf{i}}\frac{g_2^*}{\hbar}\sqrt{n}\rho_{ccvc}^{m,n-1*} + \dot{\mathbf{i}}\frac{g_1^*}{\hbar}\sqrt{m+1}\rho_{vvvc}^{n,m+1} - \dot{\mathbf{i}}\frac{g_1}{\hbar}\sqrt{n}\rho_{ccvc}^{n-1,m}
 \end{aligned} \tag{B.6}$$

Similar to the last to terms $\rho_{vvvc}^{n,m}$ is a mixed operator, but now the density like part belongs to the valence band. This affects the damping and give rise of the driving term $+\gamma_{sp}\rho_{cccc}^{n,m}$ in the second line. Again the Förster interaction couples the density like part to a polarization like part and the polarization part to a density part.

$$\begin{aligned}
 \partial_t \rho_{vvcv}^{n,m} = & (\dot{\mathbf{i}}(n-m)\omega_{sp} - \dot{\mathbf{i}}\omega \frac{g_2}{\hbar} - \frac{\gamma_{sp}}{2}(n+m) - 1/2\gamma_g)\rho_{vvcv}^{n,m} + \gamma_{sp}\sqrt{n+1}\sqrt{m+1}\rho_{vvcv}^{n+1,m+1} \\
 & + \dot{\mathbf{i}}\frac{\mu_1}{\hbar}(E_t^* \rho_{ccvc}^{m,n*} - E_t \rho_{ccvc}^{n,m}) + \dot{\mathbf{i}}\frac{\mu_2}{\hbar}E_t(\rho_{vvvc}^{n,m} - \rho_{vccv}^{n,m}) - \dot{\mathbf{i}}\frac{V_{12}}{\hbar}\rho_{vvcv}^{n,m} + \gamma_g \rho_{ccvc}^{m,n*} \\
 & + \frac{\dot{\mathbf{i}}}{\hbar}E_t^* \chi^* (\sqrt{m+1}\rho_{vvcv}^{n,m+1} - \sqrt{n}\rho_{vvcv}^{n-1,m}) + \frac{\dot{\mathbf{i}}}{\hbar}E_t \chi (\sqrt{m}\rho_{vvcv}^{n,m-1} - \sqrt{n+1}\rho_{vvcv}^{n+1,m}) \\
 & + \dot{\mathbf{i}}\frac{g_1}{\hbar}\sqrt{m}\rho_{ccvc}^{m-1,n*} - \dot{\mathbf{i}}\frac{g_1^*}{\hbar}\sqrt{n}\rho_{ccvc}^{n-1,m} + \dot{\mathbf{i}}\frac{g_2^*}{\hbar}\sqrt{m+1}\rho_{vvvc}^{n,m+1} - \dot{\mathbf{i}}\frac{g_2}{\hbar}\sqrt{n}\rho_{vccv}^{n-1,m}
 \end{aligned} \tag{B.7}$$

$\rho_{vvcv}^{n,m}$ behaves like the last term $\rho_{vvvc}^{n,m}$ with swapped semiconductor quantum dots ($1 \leftrightarrow 2$). Therefore again the Förster interaction couples both terms leading to the new plasmon polariton excitations.

$$\begin{aligned}
 \partial_t \rho_{ccvv}^{n,m} = & (\dot{\mathbf{i}}(n-m)\omega_{sp} + \dot{\mathbf{i}}(\omega \frac{g_1}{\hbar} + \omega \frac{g_2}{\hbar}) - \frac{\gamma_{sp}}{2}(n+m) - \gamma_g)\rho_{ccvv}^{n,m} + \gamma_{sp}\sqrt{n+1}\sqrt{m+1}\rho_{ccvv}^{n+1,m+1} \\
 & - \dot{\mathbf{i}}\frac{\mu_1}{\hbar}E_t^*(\rho_{vvcv}^{m,n*} - \rho_{ccvc}^{n,m}) - \dot{\mathbf{i}}\frac{\mu_2}{\hbar}E_t^*(\rho_{vvvc}^{m,n*} - \rho_{cccv}^{n,m}) \\
 & + \frac{\dot{\mathbf{i}}}{\hbar}E_t^* \chi^* (\sqrt{m+1}\rho_{ccvv}^{n,m+1} - \sqrt{n}\rho_{ccvv}^{n-1,m}) + \frac{\dot{\mathbf{i}}}{\hbar}E_t \chi (\sqrt{m}\rho_{ccvv}^{n,m-1} - \sqrt{n+1}\rho_{ccvv}^{n+1,m}) \\
 & + \dot{\mathbf{i}}\frac{g_2}{\hbar}\sqrt{m}\rho_{cccv}^{n,m-1} - \dot{\mathbf{i}}\frac{g_2}{\hbar}\sqrt{n+1}\rho_{vvvc}^{m,n+1*} + \dot{\mathbf{i}}\frac{g_1}{\hbar}\sqrt{m}\rho_{cccv}^{n,m-1} - \dot{\mathbf{i}}\frac{g_1}{\hbar}\sqrt{n+1}\rho_{vvcv}^{m,n+1*}
 \end{aligned} \tag{B.8}$$

The pure polarization like term $\rho_{ccvv}^{n,m}$ is damped by γ_g since it involves the polarization of both quantum dots and does not couple via the Förster interaction, since all quantum dots are simultaneously either excited or unexcited.

$$\begin{aligned}
 \partial_t \rho_{vccv}^{n,m} = & (\dot{\mathfrak{i}}(n-m)\omega_{sp} - \frac{\gamma_{sp}}{2}(n+m) - \gamma_g)\rho_{vccv}^{n,m} + \gamma_{sp}\sqrt{n+1}\sqrt{m+1}\rho_{vccv}^{n+1,m+1} \\
 & + \dot{\mathfrak{i}}\frac{V_{12}}{\hbar}(\rho_{cvcv}^{n,m} - \rho_{cvcv}^{m,n*}) + \gamma_g\rho_{cccc}^{n,m} \\
 & + \dot{\mathfrak{i}}\frac{\mu_1}{\hbar}(E_t^*\rho_{cccv}^{m,n*} - E_t\rho_{cccv}^{n,m}) + \dot{\mathfrak{i}}\frac{\mu_2}{\hbar}(E_t\rho_{vvcv}^{m,n*} - E_t^*\rho_{vvcv}^{n,m}) \\
 & + \frac{\dot{\mathfrak{i}}}{\hbar}E_t^*\chi^*(\sqrt{m+1}\rho_{vccv}^{n,m+1} - \sqrt{n}\rho_{vccv}^{n-1,m}) + \frac{\dot{\mathfrak{i}}}{\hbar}E_t\chi(\sqrt{m}\rho_{vccv}^{n,m-1} - \sqrt{n+1}\rho_{vccv}^{n+1,m}) \\
 & + \dot{\mathfrak{i}}\frac{g_1}{\hbar}\sqrt{m}\rho_{cccv}^{m-1,n*} - \dot{\mathfrak{i}}\frac{g_1^*}{\hbar}\sqrt{n}\rho_{cccv}^{n-1,m} + \dot{\mathfrak{i}}\frac{g_2^*}{\hbar}\sqrt{m+1}\rho_{vvcv}^{m+1,n*} - \dot{\mathfrak{i}}\frac{g_2}{\hbar}\sqrt{n+1}\rho_{vvcv}^{n+1,m}
 \end{aligned} \tag{B.9}$$

In the pure density like term $\rho_{vccv}^{n,m}$ we can again see the driving of the valance band like part through the corresponding conduction band part of $\rho_{cccc}^{n,m}$. Via the Förster interaction $\rho_{vccv}^{n,m}$ is coupled to the pure polarization like term $\rho_{cvcv}^{n,m}$.

$$\begin{aligned}
 \partial_t \rho_{cvvc}^{n,m} = & (\dot{\mathfrak{i}}(n-m)\omega_{sp} - \frac{\gamma_{sp}}{2}(n+m) - \gamma_g)\rho_{cvvc}^{n,m} + \gamma_{sp}\sqrt{n+1}\sqrt{m+1}\rho_{cvvc}^{n+1,m+1} \\
 & + \dot{\mathfrak{i}}\frac{V_{12}}{\hbar}(\rho_{cvcv}^{m,n*} - \rho_{cvcv}^{n,m}) + \gamma_g\rho_{cccc}^{n,m} \\
 & + \dot{\mathfrak{i}}\frac{\mu_1}{\hbar}E_t\rho_{vvvc}^{m,n*} - \dot{\mathfrak{i}}\frac{\mu_1}{\hbar}E_t^*\rho_{vvvc}^{n,m} + \dot{\mathfrak{i}}\frac{\mu_2}{\hbar}E_t^*\rho_{ccvc}^{m,n*} - \dot{\mathfrak{i}}\frac{\mu_2}{\hbar}E_t\rho_{ccvc}^{n,m} \\
 & + \frac{\dot{\mathfrak{i}}}{\hbar}E_t^*\chi^*(\sqrt{m+1}\rho_{cvvc}^{n,m+1} - \sqrt{n}\rho_{cvvc}^{n-1,m}) + \frac{\dot{\mathfrak{i}}}{\hbar}E_t\chi(\sqrt{m}\rho_{cvvc}^{n,m-1} - \sqrt{n+1}\rho_{cvvc}^{n+1,m}) \\
 & + \dot{\mathfrak{i}}\frac{g_1^*}{\hbar}\sqrt{m+1}\rho_{vvvc}^{m+1,n*} - \dot{\mathfrak{i}}\frac{g_1}{\hbar}\sqrt{n+1}\rho_{vvvc}^{n+1,m} + \dot{\mathfrak{i}}\frac{g_2}{\hbar}\sqrt{m}\rho_{ccvc}^{m-1,n*} - \dot{\mathfrak{i}}\frac{g_2^*}{\hbar}\sqrt{n}\rho_{ccvc}^{n-1,m}
 \end{aligned} \tag{B.10}$$

The term $\rho_{cvvc}^{n,m}$ behaves in the same way as the last one ($\rho_{vccv}^{n,m}$) with swapped quantum dot 1 and quantum dot 2.

Restricting ourself to two quantum dots and assuming only one electron per quantum dot in Equation (B.2)-(B.10), the hierarchy of the electron operators is closed at the level of expectation values with four operators. With this assumption higher orders of electron operators do not exist.

Appendix C

Parameters used to model the optical experiments

In the following we summarize the parameter used to model the optical experiments carried out in the group of Holger Lange and Tony Heinz. In table C.1 we give all parameters used and how they were determined. The parameters for the quantum dot are mostly determined by independent experiments and fits to the resulting data, like for the radiative dephasing, resonance energies and the distance between the quantum dots and the gold sphere. The dipole moment and the rate for the pure dephasing are taken from the named references.

The diameter of the gold spheres are determined by transmission electron microscopy. The resonances and the damping of the plasmons are calculated according to Section 2.1.2 by solving a continuity relation (Equation (2.16)) set up by using the Helmholtz equation.

Parameter	Symbol	Value
dipole moment QD	d	1.84enm [EB97]
radiative dephasing	γ_x	$2 \cdot 10^{-8} \text{fs}^{-1}$ (green), $6 \cdot 10^{-8} \text{fs}^{-1}$ (red) (Fit)
pure dephasing	γ_{pure}	0.053fs^{-1} [Tak93]
resonance QD	$\hbar\omega_x$	2.37eV (green), 2.08eV (red) (Spectrum)
distance QD-AuNP	R	12, 5nm up to 36, 5nm depending on spacer (TEM)
diameter AuNP	d_m	12nm, 20nm, 40nm (TEM)
resonance AuNP	$\hbar\omega_{pl}$	2.45eV (12nm), 2.45eV (20nm), 2.42eV (40nm) [KD13]
damping AuNP	γ_{pl}	0.093fs^{-1} (12nm) 0.079fs^{-1} (20nm), 0.082fs^{-1} (40nm) [KD13]
dipole moment AuNP	χ	8.17enm (12nm), 17.58enm (20nm), 49.72enm (40nm)
pulse duration	τ	300fs (laser manual)
time offset	t_{off}	90ps (IRF)
excitation frequency	$\hbar\omega$	2.37eV (green), 2.08eV (red)
	n	1
quadratic chirp	k	$5 \cdot 10^{-4} \text{fs}^{-1}$ (spectra)

Table C.1 | Parameters used to model the optical measurements in Chapter 5 and how they are determined.

We determine the laser parameter from measurements of the instrumental response function (IRF) like for the time offset. The pulse duration is taken from the laser manual since it is to

short to be totally resolved by the experimental setup. Excitation frequency and the quadratic chirp are determined via measurements of the spectra.

Appendix D

Different contributions to the far field signal for the red quantum dots coupled to a gold sphere

For sake of completeness we plot the contributions to the far field signal for the remaining spacer thicknesses of 5nm in Figure [D.1](#) and 10nm in Figure [D.1](#).

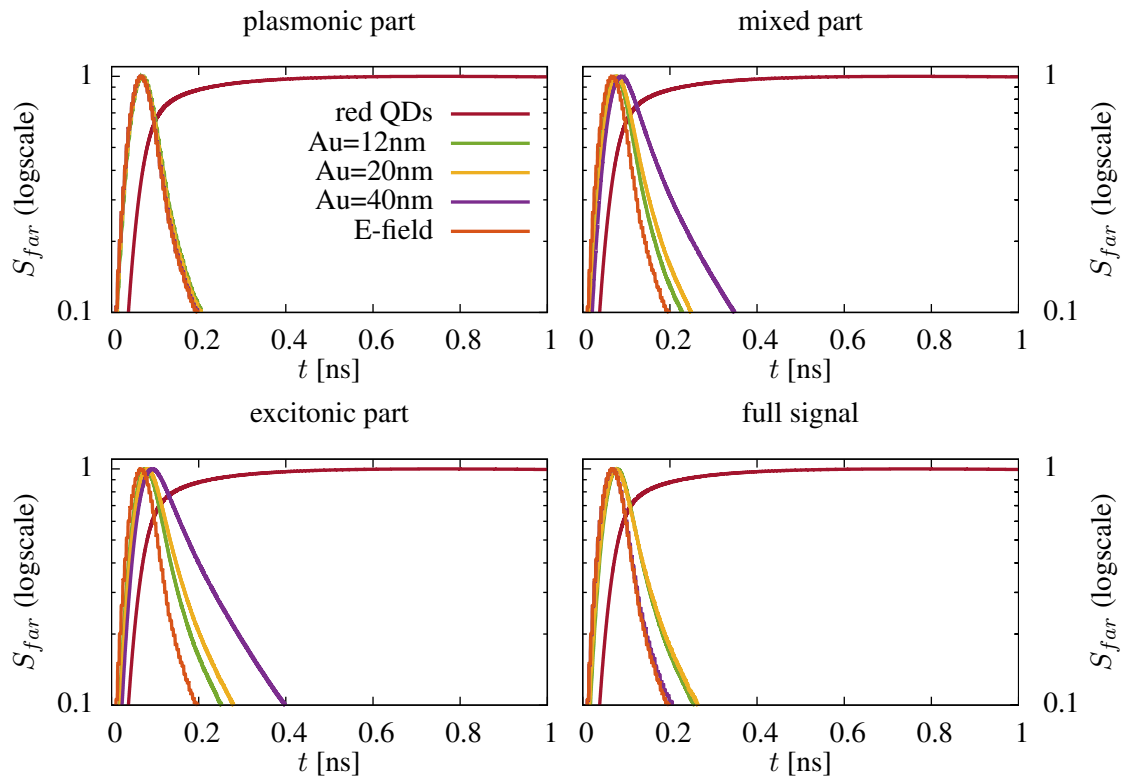


Figure D.1 | Theoretical curves averaged over an ensemble of 50 single hybrid systems and convolved with the instrumental response function. Shown in a-c are the different parts of the far field signal (5.6) for a spacer thickness of 5nm and for several diameters of the gold spheres. In c) the complete signal of the hybrid system is shown.

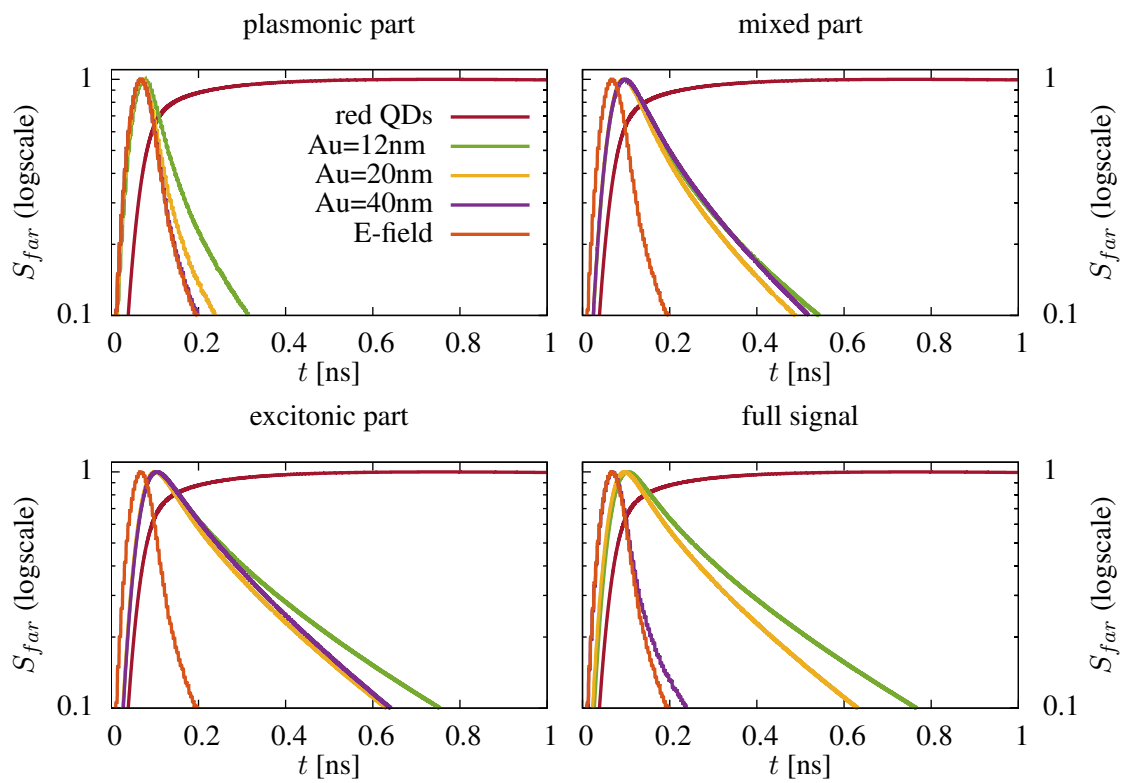


Figure D.2 | Theoretical curves averaged over an ensemble of 50 single hybrid systems and convolved with the instrumental response function. Shown in a-c are the different parts of the far field signal (5.6) for a spacer thickness of 10nm and for several diameters of the gold spheres. In c) the complete signal of the hybrid system is shown.

Bibliography

- [AAGG07] V. Ya. Aleshkin, A. V. Antonov, L. V. Gavrilenko, and V. I. Gavrilenko. Fano resonance study in impurity photocurrent spectra of bulk gaas and gaas quantum wells doped with shallow donors. *Phys. Rev. B*, 75:125201, Mar 2007.
- [ABN06] Pascal Anger, Palash Bharadwaj, and Lukas Novotny. Enhancement and quenching of single-molecule fluorescence. *Phys. Rev. Lett.*, 96:113002, Mar 2006.
- [ALA⁺10] Alexandre Aubry, Dang Yuan Lei, Antonio I. Fernandez-Dom Anguez, Yannick Sonnefraud, Stefan A. Maier, and J. B. Pendry. Plasmonic light-harvesting devices over the whole visible spectrum. *Nano Letters*, 10(7):2574–2579, 2010. PMID: 20518545.
- [AMO⁺97] Takao Aoki, Georg Mohs, Takeshi Ogasawara, Ryo Shimano, Makoto Kuwata-Gonokami, and A. Yamaguchi. Polarization dependent quantum beats of homogeneously broadened excitons. *Opt. Express*, 1(12):364–369, Dec 1997.
- [BAKM⁺97] S. Bar-Ad, P. Kner, M. V. Marquezini, S. Mukamel, and D. S. Chemla. Quantum confined fano interference. *Phys. Rev. Lett.*, 78:1363–1366, Feb 1997.
- [BCC⁺97] V I Belitsky, A Cantarero, M Cardona, C Trallero-Giner, and S T Pavlov. Feynman diagrams and fano interference in light scattering from doped semiconductors. *Journal of Physics: Condensed Matter*, 9(27):5965, 1997.
- [BEP⁺11] Sergey I Bozhevolnyi, Andrey B Evlyukhin, Anders Pors, Michael G Nielsen, Morten Willatzen, and Ole Albrektsen. Optical transparency by detuned electrical dipoles. *New Journal of Physics*, 13(2):023034, 2011.
- [Beu35] H. Beutler. über absorptionsserien von argon, krypton und xenon zu termen zwischen den beiden ionisierungsgrenzen $^2p_3^2/0$ und $^2p_1^2/0$. *Zeitschrift für Physik*, 93(3-4):177–196, 1935.
- [BFB⁺89] P. C. Becker, H. L. Fragnito, J. Y. Bigot, C. H. Brito Cruz, R. L. Fork, and C. V. Shank. Femtosecond photon echoes from molecules in solution. *Phys. Rev. Lett.*, 63:505–507, Jul 1989.
- [BLRBA99] D. Basko, G.C. La Rocca, F. Bassani, and V.M. Agranovich. Förster energy transfer from a semiconductor quantum well to an organic material overlayer. *Eur. Phys. J. B*, 8(3):353–362, 1999.

- [BLRBA02] D.M. Basko, G.C. La Rocca, F. Bassani, and V.M. Agranovich. Electronic energy transfer in a planar microcavity. *physica status solidi (a)*, 190(2):379–382, 2002.
- [Boa82] A. D. Boardman. *Electromagnetic surface modes*. John Wiley and Sons, Chichester, 1982.
- [BP51] David Bohm and David Pines. A collective description of electron interactions. i. magnetic interactions. *Phys.Rev.*, 82:625, 1951.
- [BP53] David Bohm and David Pines. A collective description of electron interactions: Iii. coulomb interactions in a degenerate electron gas. *Phys. Rev.*, 92:609–625, Nov 1953.
- [BP02] H.-P. Breuer and F. Petruccione. *The Theory of Open Quantum Systems*. Oxford University Press, Oxford, 2002.
- [BRAB⁺08] G. Bachelier, I. Russier-Antoine, E. Benichou, C. Jonin, N. Del Fatti, F. Vallee, and P.-F. Brevet. Fano profiles induced by near-field coupling in heterogeneous dimers of gold and silver nanoparticles. *Phys. Rev. Lett.*, 101:197401, Nov 2008.
- [BS03] D. J. Bergman and M. I. Stockman. Surface plasmon amplification by stimulated emission of radiation: Quantum generation of coherent surface plasmons in nanosystems. *Phys. Rev. Lett.*, 90:027402, 2003.
- [BS04] B. Babic and C. Schönenberger. Observation of fano resonances in single-wall carbon nanotubes. *Phys. Rev. B*, 70:195408, Nov 2004.
- [BSSB06] Somnath Bhowmick, Sangeeta Saini, Vijay B. Shenoy, and Biman Bagchi. Resonance energy transfer from a fluorescent dye to a metal nanoparticle. *The Journal of Chemical Physics*, 125(18):–, 2006.
- [BSX⁺06] S. Blumstengel, S. Sadofev, C. Xu, J. Puls, and F. Henneberger. Converting wigner into frenkel excitons in an inorganic/organic hybrid semiconductor nanostructure. *Phys. Rev. Lett.*, 97:237401, Dec 2006.
- [BW80] Max Born and Emil Wolf. *Principles of optics*. Pergamon Press, Oxford, 6 edition, 1980.
- [Car93] Howard Carmichael. *An Open Systems Approach to Quantum Optics*, volume 18 of *Lecture Notes in Physics Monographs*. Springer Berlin Heidelberg, 1993.
- [CHTK02] S. A. Crooker, J. A. Hollingsworth, S. Tretiak, and V. I. Klimov. Spectrally resolved dynamics of energy transfer in quantum-dot assemblies: Towards engineered energy flows in artificial materials. *Phys. Rev. Lett.*, 89:186802, Oct 2002.
- [CMW09] Carlos Campana, Bastien Mussard, and Tom K. Woo. Electrostatic potential derived atomic charges for periodic systems using a modified error functional. *Journal of Chemical Theory and Computation*, 5(10):2866–2878, 2009.

- [CR68] Julian Crowell and R. H. Ritchie. Radiative decay of coulomb-stimulated plasmons in spheres. *Phys. Rev.*, 172:436–440, Aug 1968.
- [CRBSP15] Cindy T. Cooper, Miguel Rodriguez, Steve Blair, and Jennifer S. Shumaker-Parry. Mid-infrared localized plasmons through structural control of gold and silver nanocrescents. *The Journal of Physical Chemistry C*, 119(21):11826–11832, 2015.
- [CSG14] Jie Cao, Tong Sun, and Kenneth T.V. Grattan. Gold nanorod-based localized surface plasmon resonance biosensors: A review. *Sensors and Actuators B: Chemical*, 195:332 – 351, 2014.
- [CSHL06] D. E. Chang, A. S. Sørensen, P. R. Hemmer, and M. D. Lukin. Quantum optics with surface plasmons. *Phys. Rev. Lett.*, 97:053002, Aug 2006.
- [CSSJ10] De-Li Chen, Abraham C. Stern, Brian Space, and J. Karl Johnson. Atomic charges derived from electrostatic potentials for molecular and periodic systems. *The Journal of Physical Chemistry A*, 114(37):10225–10233, 2010. PMID: 20795694.
- [CSW89] K.-P. Charle, W. Schulze, and B. Winter. The size dependent shift of the surface plasmon absorption band of small spherical metal particles. *Zeitschrift für Physik D, Atoms, Molecules and Clusters*, 12(1-4):471–475, 1989.
- [CWB01] A. A. Clerk, X. Waintal, and P. W. Brouwer. Fano resonances as a probe of phase coherence in quantum dots. *Phys. Rev. Lett.*, 86:4636–4639, May 2001.
- [CY03] A. R. Cowan and Jeff F. Young. Optical bistability involving photonic crystal microcavities and fano line shapes. *Phys. Rev. E*, 68:046606, Oct 2003.
- [Czy04] G. Czycholl. *Theoretische Festkörperphysik*. Springer, Berlin, 2004.
- [DAFK06] J. Danckwerts, K. J. Ahn, J. Förstner, and A. Knorr. Theory of ultrafast nonlinear optics of coulomb-coupled semiconductor quantum dots: Rabi oscillations and pump-probe spectra. *Phys. Rev. B*, 73(16):165318, Apr 2006.
- [DKW64] J N Dodd, R D Kaul, and D M Warrington. The modulation of resonance fluorescence excited by pulsed light. *Proceedings of the Physical Society*, 84(1):176, 1964.
- [DQK⁺13] Xiangnan Dang, Jifa Qi, Matthew T. Klug, Po-Yen Chen, Dong Soo Yun, Nicholas X. Fang, Paula T. Hammond, and Angela M. Belcher. Tunable localized surface plasmon-enabled broadband light-harvesting enhancement for high-efficiency panchromatic dye-sensitized solar cells. *Nano Letters*, 13(2):637–642, 2013. PMID: 23339821.
- [EB97] S. A. Emedocles and M. G. Bawendi. Quantum-confined stark effect in single cdse nanocrystallite quantum dots. *Science*, 278(5346):2114–2117, 1997.
- [ELRM06] P. G. Etchegoin, E. C. Le Ru, and M. Meyer. An analytic model for the optical properties of gold. *The Journal of Chemical Physics*, 125(16):–, 2006.

- [Fan35] Ugo Fano. Sullo spettro di assorbimento dei gas nobili presso il limite dello spettro d'arco. *Il Nuovo Cimento*, 12(3):154–161, 1935.
- [Fan61] U. Fano. Effects of configuration interaction on intensities and phase shifts. *Phys. Rev.*, 124:1866–1878, Dec 1961.
- [FKS⁺15] Sebastian Friede, Sergei Kuehn, Sergey Sadofev, Sylke Blumstengel, Fritz Henneberger, and Thomas Elsaesser. Nanoscale transport of surface excitons at the interface between zno and a molecular monolayer. *Phys. Rev. B*, 91:121415, Mar 2015.
- [FLKA14] Fakonas James S., Lee Hyunseok, Kelaita Yousif A., and Atwater Harry A. Two-plasmon quantum interference. *Nat Photon*, 8(4):317–320, apr 2014.
- [Fox06] M. Fox. *Quantum Optics : An Introduction: An Introduction*. Oxford Master Series in Physics. OUP Oxford, 2006.
- [FZS14] Fan Xiaofeng, Zheng Weitao, and Singh David J. Light scattering and surface plasmons on small spherical particles. *Light Sci Appl*, 3:e179, jun 2014.
- [För48] Th. Förster. Zwischenmolekulare energiewanderung und fluoereszenz. *Annalen der Physik*, 437(1-2):55–75, 1948.
- [GG09] S.V. Gaponenko and D.V. Guzatov. Possible rationale for ultimate enhancement factor in single molecule raman spectroscopy. *Chemical Physics Letters*, 477(4-6):411 – 414, 2009.
- [GGGH⁺00] J. Göres, D. Goldhaber-Gordon, S. Heemeyer, M. A. Kastner, Hadas Shtrikman, D. Mahalu, and U. Meirav. Fano resonances in electronic transport through a single-electron transistor. *Phys. Rev. B*, 62:2188–2194, Jul 2000.
- [GJH⁺15] Yu Gong, Alan G. Joly, Dehong Hu, Patrick Z. El-Khoury, and Wayne P. Hess. Ultrafast imaging of surface plasmons propagating on a gold surface. *Nano Letters*, 15(5):3472–3478, 2015. PMID: 25844522.
- [GLK07] A. O. Govorov, J. Lee, and N. A. Kotov. Theory of plasmon-enhanced förster energy transfer in optically excited semiconductor and metal nanoparticles. *Phys. Rev. B*, 76:125308, 2007.
- [GPB⁺09] M. Galli, S. L. Portalupi, M. Belotti, L. C. Andreani, L. O’Faolain, and T. F. Krauss. Light scattering and fano resonances in high-q photonic crystal nanocavities. *Applied Physics Letters*, 94(7):–, 2009.
- [GVVY⁺13] Rong-Chun Ge, C. Van Vlack, P. Yao, Jeff. F. Young, and S. Hughes. Accessing quantum nanoplasmonics in a hybrid quantum dot - metal nanosystem: Mollow triplet of a quantum dot near a metal nanoparticle. *Phys. Rev. B*, 87:205425, May 2013.
- [GZL⁺08] Weijiang Gong, Yisong Zheng, Yu Liu, Francis N. Kariuki, and Tianquan Lü. Fano effect in a t-shaped double quantum dot structure in the presence of rashba spin-orbit coupling. *Physics Letters A*, 372(16):2934 – 2940, 2008.

- [HK09] H. Haug and S.W. Koch. *Quantum Theory of the Optical and Electronic Properties of Semiconductors*. World Scientific, 2009.
- [HSD⁺08] Feng Hao, Yannick Sonnefraud, Pol Van Dorpe, Stefan A. Maier, Naomi J. Halas, and Peter Nordlander. Symmetry breaking in plasmonic nanocavities: Sub-radiant Ispr sensing and a tunable fano resonance. *Nano Letters*, 8(11):3983–3988, 2008. PMID: 18831572.
- [HYD06] Fenglan Hu, Huatong Yang, Xiaoping Yang, and Jinming Dong. Electronic transport and fano resonance in carbon nanotube ring systems. *Phys. Rev. B*, 73:235437, Jun 2006.
- [Jac99] John David Jackson. *Classical Electrodynamics*. John Wiley & Sons, New York, 3rd edition, 1999.
- [JC72] P. B. Johnson and R. W. Christy. Optical constants of the noble metals. *Phys. Rev. B*, 6(12):4370–4379, Dec 1972.
- [JSK06] Yong S Joe, Arkady M Satanin, and Chang Sub Kim. Classical analogy of fano resonances. *Physica Scripta*, 74(2):259, 2006.
- [KAP15] A. Femius Koenderink, Andrea Alu, and Albert Polman. Nanophotonics: Shrinking light-based technology. *Science*, 348(6234):516–521, 2015.
- [KBR⁺08] Vamsi K. Komarala, A. Louise Bradley, Yury P. Rakovich, Stephen J. Byrne, Yurii K. Gun'ko, and Andrey L. Rogach. Surface plasmon enhanced förster resonance energy transfer between the cdte quantum dots. *Applied Physics Letters*, 93(12):–, 2008.
- [KCZ⁺03] K. Lance Kelly, Eduardo Coronado, Lin Lin Zhao, , and George C. Schatz. The optical properties of metal nanoparticles: The influence of size, shape, and dielectric environment. *The Journal of Physical Chemistry B*, 107(3):668–677, 2003.
- [KD13] K. Kolwas and A. Derkachova. Damping rates of surface plasmons for particles of size from nano- to micrometers; reduction of the nonradiative decay. *Journal of Quantitative Spectroscopy and Radiative Transfer*, 114:45 – 55, 2013.
- [KDD06] K. Kolwas, A. Derkachova, and S. Demianiuk. The smallest free-electron sphere sustaining multipolar surface plasmon oscillation. *Computational Materials Science*, 35(3):337 – 341, 2006. Proceedings of the 4th International Conference on the Theory of Atomic and Molecular Clusters (TAMC-IV) The 4th International Conference on the Theory of Atomic and Molecular Clusters.
- [KF69] U. Kreibig and C. V. Fragstein. The limitation of electron mean free path in small silver particles. *Zeitschrift fur Physik*, 224:307–323, aug 1969.
- [KFvP⁺92] M. Koch, J. Feldmann, G. von Plessen, E. O. Göbel, P. Thomas, and K. Köhler. Quantum beats versus polarization interference: An experimental distinction. *Phys. Rev. Lett.*, 69:3631–3634, Dec 1992.

- [KG85] U. Kreibig and L. Genzel. Optical absorption of small metallic particles. *Surface Science*, 156:678 – 700, 1985.
- [KGR⁺08] Kroner M., Govorov A. O., Remi S., Biedermann B., Seidl S., Badolato A., Petroff P. M., Zhang W., Barbour R., Gerardot B. D., Warburton R. J., and Karrai K. The nonlinear Fano effect. *Nature*, 451(7176):311–314, jan 2008. 10.1038/nature06506.
- [KK06] M. Kira and S.W. Koch. Many-body correlations and excitonic effects in semiconductor spectroscopy. *Prog. Quantum Electron.*, 30(5):155–296, 2006.
- [KK08] M. Kira and S.W. Koch. Cluster-expansion representation in quantum optics. *Phys. Rev. A*, 78:022102, 2008.
- [KS12] Jacob B. Khurgin and Greg Sun. Injection pumped single mode surface plasmon generators: threshold, linewidth, and coherence. *Opt. Express*, 20(14):15309–15325, Jul 2012.
- [KS14] Jacob B. Khurgin and Greg Sun. Comparative analysis of spasers, vertical-cavity surface-emitting lasers and surface-plasmon-emitting diodes. *Nat Photon*, 8(6):468–473, jun 2014.
- [LD13] Dominic Lepage and Jan J. Dubowski. Miniaturized quantum semiconductor surface plasmon resonance platform for detection of biological molecules. *Biosensors*, 3(2):201, 2013.
- [LHZK87] R. Leonhardt, W. Holzappel, W. Zinth, and W. Kaiser. Terahertz quantum beats in molecular liquids. *Chemical Physics Letters*, 133(5):373 – 377, 1987.
- [LIH06] J. D. Lee, J. Inoue, and Muneaki Hase. Ultrafast fano resonance between optical phonons and electron-hole pairs at the onset of quasiparticle generation in a semiconductor. *Phys. Rev. Lett.*, 97:157405, Oct 2006.
- [LJC⁺12] Holger Lange, Beatriz H. Juárez, Adrian Carl, Marten Richter, Neus G. Bastús, Horst Weller, Christian Thomsen, Regine von Klitzing, and Andreas Knorr. Tunable plasmon coupling in distance-controlled gold nanoparticles. *Langmuir*, 28:298–303, 2012.
- [LK70] N. D. Lang and W. Kohn. Theory of metal surfaces: Charge density and surface energy. *Phys. Rev. B*, 1:4555–4568, Jun 1970.
- [LKL⁺15] Minah Lee, Jong Uk Kim, Ki Joong Lee, SooHoon Ahn, Yong-Beom Shin, Jonghwa Shin, and Chan Beum Park. Aluminum nanoarrays for plasmon-enhanced light harvesting. *ACS Nano*, 9(6):6206–6213, 2015. PMID: 26046384.
- [LMH⁺11] Zhongyang Li, Yingfang Ma, Ran Huang, Ranjan Singh, Jianqiang Gu, Zhen Tian, Jiaguang Han, and Weili Zhang. Manipulating the plasmon-induced transparency in terahertz metamaterials. *Opt. Express*, 19(9):8912–8919, Apr 2011.
- [Lou83] R. Loudon. *The Quantum Theory of Light*. Oxford Univ. Press, 1983.

- [LRNB03] B. W. Lovett, J. H. Reina, A. Nazir, and G. A. D. Briggs. Optical schemes for quantum computation in quantum dot molecules. *Phys. Rev. B*, 68:205319, 2003.
- [LWK76] A. Laubereau, G. Wochner, and W. Kaiser. Ultrafast coherent excitation and probing of molecular vibrations with isotopic substructure. *Phys. Rev. A*, 13:2212–2225, Jun 1976.
- [MAR06] M. E. Madjet, A. Abdurahman, and T. Renger. Intermolecular coulomb couplings from ab initio electrostatic potentials: Application to optical transitions of strongly coupled pigments in photosynthetic antennae and reaction centers. *J. Phys. Chem. B*, 110:17268–17281, 2006.
- [MBN09] Nikolay A. Mirin, Kui Bao, and Peter Nordlander. Fano resonances in plasmonic nanoparticle aggregates. *The Journal of Physical Chemistry A*, 113(16):4028–4034, 2009. PMID: 19371111.
- [MFK10] Andrey E. Miroshnichenko, Sergej Flach, and Yuri S. Kivshar. Fano resonances in nanoscale structures. *Rev. Mod. Phys.*, 82:2257–2298, 2010.
- [Mie08] Gustav Mie. Beiträge zur optik trüber medien, speziell kolloidaler metallösungen. *Annalen der Physik*, 330(3):377–445, 1908.
- [Mil94] Peter W. Milonni. *The Quantum Vacuum*. Academic Press, San Diego, 1994.
- [MLH⁺97] Miyawaki Atsushi, Llopis Juan, Heim Roger, McCaffery J. Michael, Adams Joseph A., Ikura Mitsuhiko, and Tsien Roger Y. Fluorescent indicators for Ca²⁺ based on green fluorescent proteins and calmodulin. *Nature*, 388(6645):882–887, aug 1997.
- [MST⁺95] T. Meier, A. Schulze, P. Thomas, H. Vaupel, and K. Maschke. Signatures of fano resonances in four-wave-mixing experiments. *Phys. Rev. B*, 51:13977–13986, May 1995.
- [MTK07] Torsten Meier, Peter Thomas, and Stephan W. Koch. *Coherent Semiconductor Optics*. Springer-Verlag Berlin Heidelberg, 2007.
- [NCCP08] Antonio Alvaro Ranha Neves, Andrea Camposeo, Roberto Cingolani, and Dario Pisignano. Interaction scheme and temperature behavior of energy transfer in a light-emitting inorganic-organic composite system. *Advanced Functional Materials*, 18(5):751–757, 2008.
- [ND05] Nguyen Annalee W and Daugherty Patrick S. Evolutionary optimization of fluorescent proteins for intracellular FRET. *Nat Biotech*, 23(3), mar 2005. 10.1038/nbt1066.
- [NGPJ⁺06] Carolina Novo, Daniel Gomez, Jorge Perez-Juste, Zhenyuan Zhang, Hristina Petrova, Maximilian Reismann, Paul Mulvaney, and Gregory V. Hartland. Contributions from radiation damping and surface scattering to the linewidth of the longitudinal plasmon band of gold nanorods: a single particle study. *Phys. Chem. Chem. Phys.*, 8:3540–3546, 2006.

- [NHL⁺08] Anker Jeffrey N., Hall W. Paige, Lyandres Olga, Shah Nilam C., Zhao Jing, and Van Duyne Richard P. Biosensing with plasmonic nanosensors. *Nat Mater*, 7(6):442–453, jun 2008. 10.1038/nmat2162.
- [NZB⁺09] M. A. Noginov, G. Zhu, A. M. Belgrave, R. Bakker, V. M. Shalaev, E. E. Narimanov, S. Stout, E. Herz, T. Suteewong, and U. Wiesner. Demonstration of a spaser-based nanolaser. *Nature*, 460:1110–1112, Aug 2009. 10.1038/nature08318.
- [PB52] David Pines and David Bohm. A collective description of electron interactions: II. collective vs individual particle aspects of the interactions. *Phys. Rev.*, 85:338–353, Jan 1952.
- [PGC⁺13] Young-Shin Park, Yagnaseni Ghosh, Yongfen Chen, Andrei Piryatinski, Ping Xu, Nathan H. Mack, Hsing-Lin Wang, Victor I. Klimov, Jennifer A. Hollingsworth, and Han Htoon. Super-poissonian statistics of photon emission from single cdse-cds core-shell nanocrystals coupled to metal nanostructures. *Phys. Rev. Lett.*, 110:117401, Mar 2013.
- [Pin53] David Pines. A collective description of electron interactions: IV. electron interaction in metals. *Phys. Rev.*, 92:626–636, Nov 1953.
- [Pro12] Igor E Protsenko. Theory of the dipole nanolaser. *Physics-Uspekhi*, 55(10):1040, 2012.
- [PSF⁺12] Elmar Pösel, Christian Schmidtke, Steffen Fischer, Kersten Peldschus, Johannes Salamon, Hauke Kloust, Huong Tran, Andrea Pietsch, Markus Heine, G. Adam, U. Schumacher, C. Wagener, S. Förster, and H. Weller. Tailor-made quantum dot and iron oxide based contrast agents for in vitro and in vivo tumor imaging. *ACS Nano*, 6(4):3346–3355, 2012. PMID: 22463104.
- [PV14] Vladimir M. Parfenyev and Sergey S. Vergeles. Quantum theory of a spaser-based nanolaser. *Opt. Express*, 22(11):13671–13679, Jun 2014.
- [PZMM15] Thomas Plehn, Dirk Ziemann, Jörg Megow, and Volkhard May. Frenkel to wannier-mott exciton transition: Calculation of fret rates for a tubular dye aggregate coupled to a cdse nanocrystal. *The Journal of Physical Chemistry B*, 119(24):7467–7472, 2015. PMID: 25531181.
- [RAK⁺06] Marten Richter, Kwang Jun Ahn, Andreas Knorr, Andrei Schliwa, Dieter Bimberg, Mohamed El-Amine Madjet, and Thomas Renger. Theory of excitation transfer in coupled nanostructures - from quantum dots to light harvesting complexes. *Phys. Status Solidi B*, 243(10):2302–2310, 2006.
- [RCSK09] Marten Richter, Alexander Carmele, Anna Sitek, and Andreas Knorr. Few-photon model of the optical emission of semiconductor quantum dots. *Phys. Rev. Lett.*, 103(8):087407, 2009.
- [RDSF⁺10] A. Ridolfo, O. Di Stefano, N. Fina, R. Saija, and S. Savasta. Quantum plasmonics with quantum dot-metal nanoparticle molecules: Influence of the fano effect on photon statistics. *Phys. Rev. Lett.*, 105:263601, Dec 2010.

- [RGTK15] Marten Richter, Michael Gegg, T. Sverre Theuerholz, and Andreas Knorr. Numerically exact solution of the many emitter - cavity laser problem: Application to the fully quantized spaser emission. *Phys. Rev. B*, 91:035306, Jan 2015.
- [RSK⁺13] Søren Raza, Nicolas Stenger, Shima Kadkhodazadeh, Søren V. Fischer, Natalie Kostesha, Antti-Pekka Jauho, Andrew Burrows, Martijn Wubs, and Asger Mortensen. Blueshift of the surface plasmon resonance in silver nanoparticles studied with eels. *Produktinformation Nanophotonics*, 2(2), April 2013.
- [Rup82] R. Ruppin. Decay of an excited molecule near a small metal sphere. *jcp*, 76:1681–1684, feb 1982.
- [RW69] R. H. Ritchie and R. E. Wilems. Photon-plasmon interaction in a nonuniform electron gas. i. *Phys. Rev.*, 178:372–381, Feb 1969.
- [RYS⁺13] Søren Raza, Wei Yan, Nicolas Stenger, Martijn Wubs, and N. Asger Mortensen. Blueshift of the surface plasmon resonance in silver nanoparticles: substrate effects. *Opt. Express*, 21(22):27344–27355, Nov 2013.
- [SBB⁺15] R. Schlesinger, Bianchi F., Blumstengel S., Christodoulou C., Ovsyannikov R., Kobin B., Moudgil K., Barlow S., Hecht S., Marder S.R., Henneberger F., and Koch N. Efficient light emission from inorganic and organic semiconductor hybrid structures by energy-level tuning. *Nat Commun*, 6, apr 2015.
- [Sch03] Gregory D Scholes. Long-range resonance energy transfer in molecular systems. *Annu. Rev. Phys. Chem.*, 54:57–87, 2003.
- [SK11] G. Sun and J. B. Khurgin. Theory of optical emission enhancement by coupled metal nanoparticles: An analytical approach. *Applied Physics Letters*, 98(11):–, 2011.
- [SKD12] Scholl Jonathan A., Koh Ai Leen, and Dionne Jennifer A. Quantum plasmon resonances of individual metallic nanoparticles. *Nature*, 483(7390):421–427, mar 2012. 10.1038/nature10904.
- [SKR15] Judith F. Specht, Andreas Knorr, and Marten Richter. Two-dimensional spectroscopy: An approach to distinguish förster and dexter transfer processes in coupled nanostructures. *Phys. Rev. B*, 91:155313, Apr 2015.
- [SKY09] G. Sun, J. B. Khurgin, and C. C. Yang. Impact of high-order surface plasmon modes of metal nanoparticles on enhancement of optical emission. *Applied Physics Letters*, 95(17):–, 2009.
- [Sla98] Jiri Ctyroky Slavik, Jiri Homola. Miniaturization of fiber optic surface plasmon resonance sensor. *Sensors and Actuators B: Chemical*, 51(1-3):311 – 315, 1998.
- [SP03] Sekar Rajesh Babu and Periasamy Ammasi. Fluorescence resonance energy transfer (FRET) microscopy imaging of live cell protein localizations. *The Journal of Cell Biology*, 160(5):629–633, jan 2003.

- [Sto11] Mark I. Stockman. Nanophotonics: Shrinking light-based technology. *Physics Today*, February 2011.
- [SZ97] M. O. Scully and M. S. Zubairy. *Quantum Optics*. Cambridge University Press, Cambridge, 1997.
- [SZZ⁺10] Xiong-Rui Su, Wei Zhang, Li Zhou, Xiao-Niu Peng, and Qu-Quan Wang. Plasmon-enhanced förster energy transfer between semiconductor quantum dots: multipole effects. *Opt. Express*, 18(7):6516–6521, Mar 2010.
- [Tak93] T. Takagahara. Electron-phonon interactions and excitonic dephasing in semiconductor nanocrystals. *Phys. Rev. Lett.*, 71(21):3577–3580, Nov 1993.
- [TCRK13] T. Sverre Theuerholz, Alexander Carmele, Marten Richter, and Andreas Knorr. Influence of förster interaction on light emission statistics in hybrid systems. *Phys. Rev. B*, 87:245313, Jun 2013.
- [TMO⁺13] Tame M. S., McEnery K. R., Ozdemir S. K., Lee J., Maier S. A., and Kim M. S. Quantum plasmonics. *Nat Phys*, 9(6):329–340, Jun 2013.
- [VAP⁺12] Aleksei P Vinogradov, Evgenii S Andrianov, Aleksandr A Pukhov, Aleksandr V Dorofeenko, and A A Lisyansky. Quantum plasmonics of metamaterials: loss compensation using spasers. *Physics-Uspekhi*, 55(10):1046, 2012.
- [VKR⁺14] Eike Verdenhalven, Andreas Knorr, Marten Richter, Bjoern Bieniek, and Patrick Rinke. Theory of optical excitations in dipole-coupled hybrid molecule-semiconductor layers: Coupling of a molecular resonance to semiconductor continuum states. *Phys. Rev. B*, 89:235314, Jun 2014.
- [VSS⁺09] Niels Verellen, Yannick Sonnefraud, Heidar Sobhani, Feng Hao, Victor V. Moshchalkov, Pol Van Dorpe, Peter Nordlander, and Stefan A. Maier. Fano resonances in individual coherent plasmonic nanocavities. *Nano Letters*, 9(4):1663–1667, 2009. PMID: 19281254.
- [VVKH12] C. Van Vlack, Philip Trost Kristensen, and S. Hughes. Spontaneous emission spectra and quantum light-matter interactions from a strongly coupled quantum dot metal-nanoparticle system. *Phys. Rev. B*, 85:075303, Feb 2012.
- [WM08] D.F. Walls and G.J. Milburn. *Quantum Optics*. SpringerLink: Springer e-Books. Springer Berlin Heidelberg, 2008.
- [WS10] Edo Waks and Deepak Sridharan. Cavity qed treatment of interactions between a metal nanoparticle and a dipole emitter. *Phys. Rev. A*, 82:043845, Oct 2010.
- [YZD⁺08] Jie-Yun Yan, Wei Zhang, Suqing Duan, Xian-Geng Zhao, and Alexander O. Govorov. Optical properties of coupled metal-semiconductor and metal-molecule nanocrystal complexes: Role of multipole effects. *Phys. Rev. B*, 77:165301, Apr 2008.
- [ZG11] Wei Zhang and Alexander O. Govorov. Quantum theory of the nonlinear fano effect in hybrid metal-semiconductor nanostructures: The case of strong nonlinearity. *Phys. Rev. B*, 84:081405, Aug 2011.

- [ZGB06] Wei Zhang, Alexander O. Govorov, and Garnett W. Bryant. Semiconductor-metal nanoparticle molecules: Hybrid excitons and the nonlinear fano effect. *Phys. Rev. Lett.*, 97:146804, Oct 2006.
- [ZGW⁺08] Shuang Zhang, Dentcho A. Genov, Yuan Wang, Ming Liu, and Xiang Zhang. Plasmon-induced transparency in metamaterials. *Phys. Rev. Lett.*, 101:047401, Jul 2008.
- [ZL13] Xiao-Lan Zhong and Zhi-Yuan Li. All-analytical semiclassical theory of spaser performance in a plasmonic nanocavity. *Phys. Rev. B*, 88:085101, Aug 2013.
- [ZLL⁺13] Yundong Zhang, Jin Li, Hanyang Li, Chengbao Yao, and Ping Yuan. Plasmon-induced-transparency in subwavelengthstructures. *Optics & Laser Technology*, 49(0):202 – 208, 2013.
- [ZLPW⁺15] Na Zhou, Vanesa Lopez-Puente, Qing Wang, Lakshminarayana Polavarapu, Isabel Pastoriza-Santos, and Qing-Hua Xu. Plasmon-enhanced light harvesting: applications in enhanced photocatalysis, photodynamic therapy and photovoltaics. *RSC Adv.*, 5:29076–29097, 2015.

